

# X-ray-Based Techniques to Study the Nano–Bio Interface

Carlos Sanchez-Cano, Ramon A. Alvarez-Puebla, John M. Abendroth, Tobias Beck, Robert Blick, Yuan Cao, Frank Caruso, Indranath Chakraborty, Henry N. Chapman, Chunying Chen, Bruce E. Cohen, Andre L. C. Conceição, David P. Cormode, Daxiang Cui, Kenneth A. Dawson, Gerald Falkenberg, Chunhai Fan, Neus Feliu, Mingyuan Gao, Elisabetta Gargioni, Claus-C. Glüer, Florian Grüner, Moustapha Hassan, Yong Hu, Yalan Huang, Samuel Huber, Nils Huse, Yanan Kang, Ali Khademhosseini, Thomas F. Keller, Christian Körnig, Nicholas A. Kotov, Dorota Koziej, Xing-Jie Liang, Beibei Liu, Sijin Liu, Yang Liu, Ziyao Liu, Luis M. Liz-Marzán, Xiaowei Ma, Andres Machicote, Wolfgang Maisson, Adrian P. Mancuso, Saad Megahed, Bert Nickel, Ferdinand Otto, Cristina Palencia, Sakura Pascarelli, Arwen Pearson, Oula Peñate-Medina, Bing Qi, Joachim Rädler, Joseph J. Richardson, Axel Rosenhahn, Kai Rothkamm, Michael Rübhausen, Milan K. Sanyal, Raymond E. Schaak, Heinz-Peter Schlemmer, Marius Schmidt, Oliver Schmutzler, Theo Schotten, Florian Schulz, A. K. Sood, Kathryn M. Spiers, Theresa Staufer, Dominik M. Stemer, Andreas Stierle, Xing Sun, Gohar Tsakanova, Paul S. Weiss, Horst Weller, Fabian Westermeier, Ming Xu, Huijie Yan, Yuan Zeng, Ying Zhao, Yuliang Zhao, Dingcheng Zhu, Ying Zhu, and Wolfgang J. Parak\*

 Cite This: <https://dx.doi.org/10.1021/acsnano.0c09563>

 Read Online

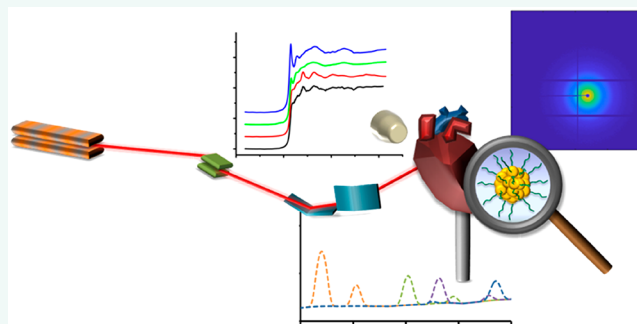
ACCESS |

 Metrics & More

 Article Recommendations

**ABSTRACT:** X-ray-based analytics are routinely applied in many fields, including physics, chemistry, materials science, and engineering. The full potential of such techniques in the life sciences and medicine, however, has not yet been fully exploited. We highlight current and upcoming advances in this direction. We describe different X-ray-based methodologies (including those performed at synchrotron light sources and X-ray free-electron lasers) and their potentials for application to investigate the nano–bio interface. The discussion is predominantly guided by asking how such methods could better help to understand and to improve nanoparticle-based drug delivery, though the concepts also apply to nano–bio interactions in general. We discuss current limitations and how they might be overcome, particularly for future use *in vivo*.

**KEYWORDS:** nano–bio interface, X-ray techniques, synchrotron radiation, imaging, nanoparticles, delivery, degradation, spectroscopy



Several drugs on the market consist of more than just a homogeneous pill for oral delivery or the injection of a solution for intravenous administration, but are intrinsically heterogeneous, comprising multiple compounds. In the case of nanoparticle (NP)-based drugs, they usually involve a particulate delivery vehicle and a pharmaceutically active compound, which is to be delivered to and released at the target site. This concept reaches back decades,<sup>1</sup> well before the actual term “nanomedicine”, under which such NP-based drugs nowadays are referred, was coined. Examples include Abraxane, where the pharmaceutical therapeutic

paclitaxel is delivered *via* protein carriers,<sup>2</sup> or Doxil, where doxorubicin (DOX) is delivered *via* liposomes.<sup>3</sup> However, before reaching acceptance for clinical use, such NP-based

Received: November 13, 2020

Accepted: January 25, 2021

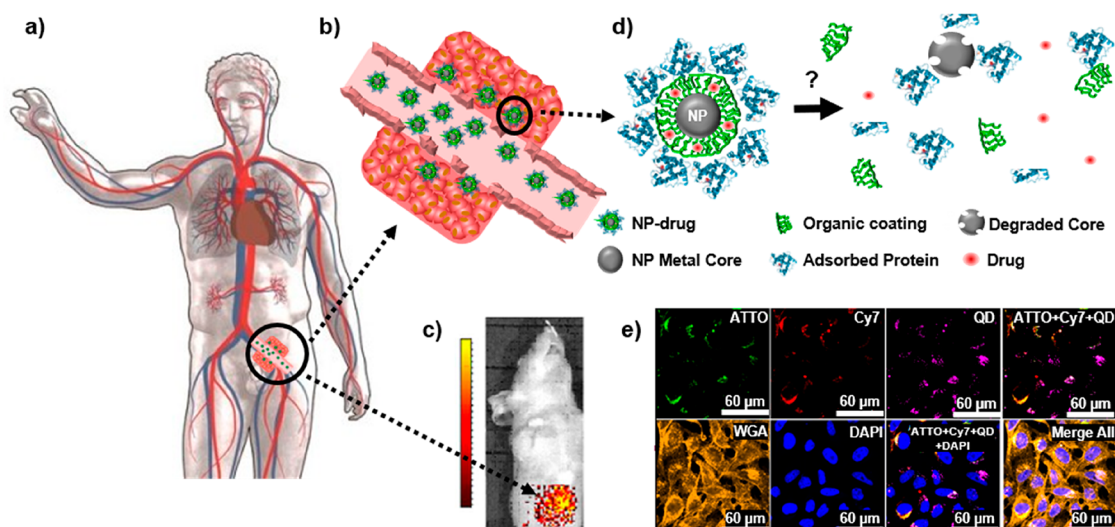


**Figure 1.** (a) Sketch of a hypothetical scenario in which nanoparticle (NP)-based drugs are administered intravenously for the purpose of cancer treatment. (b) In leaky tumor tissue, some NP-based drugs may be retained by passive targeting.<sup>10,11</sup> But do these drugs penetrate effectively into the tumor tissue or remain at the tumor surface? (c) Fluorescently labeled NP-based drugs can be imaged *in vivo* in animal models, but spatial resolution is typically too low and does not allow conclusions about the distribution of the NPs in the tumor tissue. Reprinted with permission from ref 13 under a CC BY-NC-ND 4.0 International License. Copyright 2016 Nature Research. (d) Inside the human body, the NP-based drugs, comprising a NP carrier/vehicle (gray), an organic surface coating including ligands for targeting (green), the drug to be delivered (red), and a corona of adsorbed proteins (blue) may degrade, which can completely change the NP properties. (e) Example of *in vitro* degradation of a model for a NP-based drug after endocytosis by cells. Here, the NP-based model drug used can be identified in different compartments by their fluorescence (shown in false colors in the overlay of different fluorescence channels): CdSe/ZnS quantum dots (QDs) (purple) as NP carriers, ATTO-labeled polymer shell around the QDs (green), representing the ligands on the NP surface, and preadsorbed Cy7-labeled proteins (red) symbolizing a drug to be delivered. As shown in the image, after exposure, the location of the different compounds of the NP-based model drug can be mapped by fluorescence imaging. Data from Carrillo-Carrion *et al.* demonstrate that the three components of the NP (QD core, polymer shell, protein corona) disintegrate over time, as colocalization is partly lost.<sup>17</sup> However, fluorescence imaging is not ideal to follow all the different parts of the NP-based drugs. For example, Cd ions released from the CdSe/ZnS core cannot be directly imaged based on fluorescence. Reprinted with permission from ref 17. Copyright 2019 American Chemical Society.

systems (as with any drug) have to undergo rigorous clinical trials. Apart from probing the biological effects of the drug (*i.e.*, pharmacodynamics), testing also involves characterization of the drug itself and the NP vehicle, specifically, its pharmacokinetics.

Independent of the route of administration (*e.g.*, oral, intravenous, *etc.*), drugs are formulated with numerous pharmaceutical excipients to ensure the desired pharmacological function. Conventionally, absorption enhancers, emulsifiers, diluents, preservatives, solvents, sustained release matrices, *etc.*, are used to shape the pharmacokinetic profile of a drug.<sup>4</sup> At the dawn of nanotechnology, novel and fascinating opportunities for drug formulations emerge. For instance, it has been demonstrated that the therapeutic window of approved drugs will dramatically expand, if dissipated into a nanocrystalline formulation.<sup>5</sup> Far beyond established methodologies, nanotechnology enhances the targeted delivery and controlled release onto the cellular and even subcellular levels, hence emulating fundamental biological mechanisms, such as cell–cell or cell–messenger interactions. Albeit much more sophisticated, nanoformulations have to meet the same regulatory requirements of pharmacovigilance as conventional drugs with respect to effectiveness, efficacy, safety, and benefit.<sup>6</sup> However, due to the cardinal differences compared to conventional drugs, improved methods are urgently needed to monitor the adsorption, distribution, metabolism, excretion–toxicity (ADME–T) profile of a NP-based drug.

Figure 1 depicts a scenario in which a hypothetical patient is being treated with an intravenously injected NP-based drug. We describe the NP-based drug with a model system composed of the NP carrier matrix/vehicle, which is modified on its surface with a coating that provides colloidal stability, could help to minimize immune response, and might also carry targeting ligands, and an encapsulated or appended pharmaceutical compound.<sup>7,8</sup> However, such a NP-based drug is not a static assembly and, after its administration to the human body, may undergo changes in composition.<sup>9</sup> The fate of the NP-based drug over time thus becomes an important consideration. As expected, initially, a part of the NP-based drugs will be cleared from circulation by the immune system and end up in the liver and spleen, while some fraction will arrive at the actual target site, such as a tumor.<sup>10,11</sup> On the route to reach the target site, however, there are several scenarios that can render delivery less efficient. For example, the surfaces of NP-based drugs may be overcoated due to the formation of a protein corona<sup>12</sup> or may suffer enzymatic degradation of their targeting moieties.<sup>9</sup> Ultimately, these surface changes may worsen the capability of the NP-based drug to achieve active targeting, which depends on ligand density.<sup>13</sup> If all targeting ligands are cleaved, there will no longer be active targeting. Even partial cleavage may have dramatic effects on targeting, if multivalent interactions play roles in target recognition.<sup>14</sup> Furthermore, degradation of the surface coating<sup>15</sup> may also lead to the agglomeration of the carrier NPs and thus potentially induce clogging of the blood vessels.<sup>16</sup> Besides agglomeration,

degradation can lead to significantly altered chemical surface structures with respect to polarity or charge. These changes, in turn, will impact in the biodistribution of a NP-based drug by altering its solubility, ability for serum protein binding, and membrane permeability. Finally, degradation of the carrier NP vehicle in the blood may also lead to the loss of the pharmaceutical compound before it actually reaches the target site. In this case, there would be no biological effects as a result of treatment with the NP-based drug, as only the empty NP carrier, but not the embedded pharmaceutical compound, would reach the target site. Thus, as different parts of NP-based drugs degrade over time, following *in vivo* the fate of their individual components is important to understand what is exactly delivered to the target site. Equally important is understanding the efficacy of the targeting strategy chosen to enrich the NP-based drug in its target and the delivery efficiency of the drug from the NP carrier once it has reached it. Again, if the intact NP carrier is not capable of accumulating in the areas that need to be treated (*e.g.*, organs or tumors), or the embedded therapeutic drug cannot be released when required, the overall therapeutic activity will be compromised.

Moreover, once at the target site, NP-based drugs need to penetrate into the tissue and typically get internalized by cells (usually through endosomal pathways), where the pharmaceutical component is supposed to be released into the cytosol. Therefore, targeted drug delivery and controlled drug release represent important parts of drug delivery. Keeping in mind that only a small fraction of the drug or the NP carrier will reach the target and that the drug may cause side effects in other organs, ensuring stable encapsulation that only releases the toxic drug/pharmaceutical agent at the target site would be advantageous. Following this approach, the drug would be released from the NP carrier once the carrier reaches the target tissue, and thus the therapeutic effect would be limited to the immediate vicinity of the target cells, with maximum efficacy. Several strategies have been developed for controlled release, including site-activated release, for example, based on environment sensing mechanisms or by triggering heat dissipation from magnetic NPs embedded in liposomes. For environment-sensing drug release, several approaches based on pH-dependent release have been reported, premised on the observation that pH levels can be different in pathological (*e.g.*, inflamed or infected) tissues or cells. Lipid structures can be made responsive to pH changes, so they are ideal for environment-sensing delivery systems, both for extracellular as well as intracellular release. To understand the release of the pharmacological agent from the NP carrier vehicle, the localization of each of the components needs to be mapped with subcellular resolution. The localization and transformations of the different units of the NP-based drug are important for its biological activity. For example, pharmaceutical compounds can lead to completely different cellular effects depending on their intracellular location (*e.g.*, therapeutic agents acting at the mRNA level would be ineffective if they are confined to endosomes/lysosomes and not released to the cytosol, where the mRNA is located).<sup>18</sup> Also, metal cores (*e.g.*, for NP carrier vehicles) may undergo a variety of transformations once internalized by cells/tissue, which might be vital to understanding the activity or potential risks of NP-based drugs due to NP-induced toxicity (*e.g.*, release of Ag<sup>+</sup> when using Ag-based carriers).<sup>19–24</sup> Thus,

in order to understand the effects of NP-based drugs, biological responses need to be correlated to the intracellular locations,<sup>25</sup> speciation, and behavior of the different compounds of the NP-based drug.

However, it is difficult to obtain information about the structural rearrangements in the delivery system while in a liquid environment. Small-angle X-ray scattering (SAXS) has been used to study these processes and is now an essential tool to gather information and to fine-tune lipid drug release systems.<sup>26–29</sup> Alternatively, drugs can be released from liposomes that incorporate sphingomyelin in their membranes. If such sphingomyelin-liposomes are in contact with the enzyme sphingomyelinase (expressed by stressed cells in tumors or inflammatory tissue), the lipid molecule is broken down into its constituents, ceramide and phosphorylcholine. These molecules no longer have an optimal fit, so the liposome membrane becomes more permeable, and the contents of the liposomes are released. X-ray-based techniques can be used to study these microdomain changes for optimized drug release. External activation methods using magnetic fields have also been developed as an additional means of controlled drug release.<sup>30</sup> Here, ferric NP-containing liposomes are used. Once enough drug carriers have accumulated at the target site, an external alternating magnetic field is directed at the desired location and membrane disruption induced from local heating or by mechanical actuation results in a leaky liposome membrane and subsequent drug release. The synergistic effect of the enzyme and the applied magnetic field induces a more potent and selective release than a single approach alone.<sup>31,32</sup> Again, for the selection of optimized ferric NPs and monitoring conformational changes leading to the release of the drug, X-ray-based analyses are most valuable. In order to study the process, different markers can be attached to the carrier (to monitor delivery) and the drug (to monitor release).

The examples presented here illustrate the potential of NP carriers with mechanisms for controlled release. Related alternative approaches have been reviewed recently.<sup>33</sup> The development of improved luminescent NPs is of interest for targeted drug delivery as well. Photoactive NPs that respond to near-infrared (NIR) excitation could be used for spatially targeted delivery, as NIR light penetrates tissue to greater depths than shorter wavelengths with considerably less phototoxicity.<sup>34,35</sup> Upconverting NPs (UCNPs) make use of energy-transfer upconversion between neighboring lanthanide ions to convert tissue-penetrating NIR light efficiently to visible or UV light. Targeted UCNPs can be used to release therapeutics through UV-based uncaging strategies, creating highly localized light sources of wavelengths that might otherwise be cytotoxic.<sup>36–38</sup> The stable optical response of these NPs also enables extended tracking<sup>39,40</sup> as well as sensitive detection of cellular fluctuations in response to temperature and pressure.<sup>41–43</sup> Moreover, UCNPs have been shown to excite retinal opsins to endow mice with NIR vision<sup>44</sup> as well as to power optogenetic switches in awake mouse brains,<sup>45</sup> suggesting that even more complex therapeutic strategies are possible with these NIR-responsive NPs. For each of these NP-based approaches, understanding the fate of NP-based drugs in biological organisms is of vital importance to improve their potential medical applications.

All of these aspects require efficient imaging or spectroscopic tools to study the behavior of NP-based drugs *in situ* in biological environments or whole biological

**Table 1. List of Current Techniques Commonly Used to Study the Biodistribution or Fate of Nanoparticle (NP)-Drugs in Biological Samples**

<i>Current techniques to study nanoparticles in biological environments</i>				
Type of Tech.	Variants	Uses	Limitations	Advantages
MS	ICP-MS LA-ICP-MS PIRL-MS	<ul style="list-style-type: none"> <li>Detection of NP-based drugs on body fluids</li> <li>Biodistribution of NPs-based drugs <i>ex vivo</i></li> </ul>	<ul style="list-style-type: none"> <li>Does not provide spatial resolution unless coupled to a Laser ablation system</li> <li>Cannot image unstained specific molecules</li> <li>Difficult to use <i>in vivo- in situ</i></li> </ul>	<ul style="list-style-type: none"> <li>Good detection limit</li> <li>ICP-MS allows element-specific detection</li> <li>Coupling with PIRL allows application <i>in vivo</i> on superficial areas</li> </ul>
EM	TEM SEM	<ul style="list-style-type: none"> <li>Imaging of NP-based drugs in cells or surfaces of biological samples</li> </ul>	<ul style="list-style-type: none"> <li>Very low penetration, impossible to use <i>in situ</i></li> <li>Hard to use on life samples</li> <li>Small field of view, hard to image large samples</li> </ul>	<ul style="list-style-type: none"> <li>Very good resolution</li> <li>Detect easily organelles and NPs with great detail</li> <li>Element specific when combined with EDX or EELS</li> <li>Can provide 3D images</li> </ul>
PET/SPECT		<ul style="list-style-type: none"> <li>Biodistribution of NP-based drugs <i>in vivo</i></li> </ul>	<ul style="list-style-type: none"> <li>Require radiolabeling with radioactive traces</li> <li>No simultaneous multiplex imaging</li> <li>Limited spatial resolution</li> <li>Cannot differentiate between chemical elements</li> <li>Cannot differentiate chemical state</li> </ul>	<ul style="list-style-type: none"> <li>Non-destructive</li> <li>Can be used <i>in vivo</i> on full organisms</li> <li>Low background noise</li> <li>Imaging deep inside tissue <i>in vivo</i> is possible</li> </ul>
MRI		<ul style="list-style-type: none"> <li>Imaging of soft tissues</li> <li>Biodistribution of NP-based drugs <i>in vivo</i></li> </ul>	<ul style="list-style-type: none"> <li>Difficult to image hard tissues</li> <li>Cannot reach cellular or sub-cellular resolution</li> </ul>	<ul style="list-style-type: none"> <li>Non-destructive</li> <li>Can be used <i>in vivo</i> on full organisms</li> <li>Imaging deep inside tissue <i>in vivo</i> is possible</li> <li>Multiplex imaging is possible</li> <li>Can provide chemical information</li> </ul>
Optical Microscopy	2-photon NIR SERS PAI OCT	<ul style="list-style-type: none"> <li>Biodistribution of NP-based drugs <i>in vivo</i></li> </ul>	<ul style="list-style-type: none"> <li>Very limited tissue penetration due to scattering problems</li> </ul>	<ul style="list-style-type: none"> <li>Non-destructive</li> <li>Sub-cellular resolution</li> <li>Multiplex imaging is simple</li> <li>Can be used <i>in vivo</i></li> <li>Can be combined with other imaging techniques</li> </ul>

samples such as small animals, allowing direct detection of the different components of the NP-based drugs (to overcome the loss of information as a result of their degradation) and, more importantly, providing high spatial resolution. In mapping the fate of NPs, it is desirable to access different size scales, ranging from subcellular resolution to full organisms (*i.e.*, humans or small animals). Therefore, if a single analytical technique is to be used, it should be capable of changing magnification, to provide optimal spatial resolution according to the requirements of the sample to be analyzed.

The functionalization of NP surfaces is critical for targeting therapeutics to organs and cells of interest and for minimizing toxicity and off-target effects. Intrinsically hydrophobic NPs must be transformed into being hydrophilic by surface

functionalization, and this combination of aqueous surface passivation and biomolecule targeting determines the interactions of the NPs with living systems. While many NP–biomolecule complexes have been assembled by non-specific or reversible linkages, the challenge of maintaining the stability of these complexes within tissue has spawned a number of bioconjugation strategies to attach proteins and organic ligands covalently to NP surfaces, with controlled stoichiometry.<sup>46–50</sup> Identifying a suitable labeling approach for deciphering the degradation processes occurring in the NP-coatings while keeping the efficiency of targeting or delivery of the drug is not straightforward. The label needs to be stable (to limit degradation throughout the course of the study) and detectable with analytical techniques of high sensitivity and resolution. But most of all, it needs to be

modular, in the sense that it should allow chemoselective conjugation to the region of interest, for example, by immobilization on metallic NPs or covalently linked to organic coatings on the surface of the NPs (which helps to understand degradation and targeting) or to the drug embedded (which provides vital information about delivery to the target).<sup>51</sup> In this context, bifunctional metal chelators such as 1,4,7,10-tetraazacyclododecane-1,4,7,10-tetraacetic acid and its derivatives enable the introduction of various labels as tracers into the coating of NPs and may thus be used for detailed analysis of degradation processes.<sup>52</sup> This includes radiolabels compatible with positron emission tomography (PET) or single photon emission computed tomography (SPECT) imaging,<sup>53</sup> nonradioactive heavy metals compatible with magnetic resonance imaging (MRI) and NIR fluorescence, or elemental labels with high contrast in inductively coupled plasma mass spectrometry (ICP-MS) and X-ray detection (such as X-ray fluorescence imaging, XFI).<sup>54–57</sup> Nevertheless, any modification of the structure of a drug might alter its therapeutic activity and biological behavior, an important consideration that must be understood and considered before deciding upon one or more labels.

In addition to using NPs alone as drug delivery vehicles, it is also possible to integrate NPs within different types of materials or as components of gels. Integration of NPs within hydrogels allows improving the mechanical, biological, and chemical properties of the material. One example of this strategy is the integration of nanosilicates, such as Laponite, within polymers that form shear-thinning hydrogels. Such nanosilicates have charge distributions that allow them to interact with gelatin polymers by electrostatic interactions forming bonds that can be broken upon application of force. The incorporation of Laponite within gelatin has been shown to form hydrogels that can be used for various regenerative applications as well as medical devices for embolization.<sup>58</sup> These hydrogels have shown great potential; one advantage is their ability to be delivered through catheters and utilized in minimally invasive manners. Unfortunately, some of these materials are not radio-opaque by themselves. In such cases, the addition of contrast agents such as tantalum can make these hydrogels visible to X-rays and thus suitable for computed tomography (CT) scans and other X-ray techniques. Integration of nanomaterials with non-invasive imaging approaches provides opportunities to address a number of issues such as internal bleeding, aneurysms, and other medical problems. Ultimately *in situ* and *in vivo* analyses will be most valuable.

While with current technologies, *in situ* analyses in humans are not yet feasible, we discuss in this Review current developments toward this goal and obstacles still to be solved. We start first with a description of the state-of-the-art techniques, followed by a forward-looking analysis of the possible improvements in the near term.

## SELECTED CURRENT TECHNIQUES TO STUDY NANOPARTICLE-BASED DRUGS IN BIOLOGICAL ENVIRONMENTS

Over the past century, analytical chemistry has developed a large set of methodologies for the detection of molecular species in biological settings (Table 1). From samples of body fluids, in particular blood and urine, degradation and clearance of the different components of a drug can be

tracked, using, for example, mass spectrometry (MS).<sup>59–62</sup> Though not *in situ*, body fluids can be extracted at different time points from the organism, providing important details on the pharmacokinetics of drugs. However, as detection is performed in blood, urine, *etc.*, spatial resolution is lost. This strategy results in it not being possible to know the concentrations of drugs and their metabolites in the specific organs where a drug is being degraded. Often, to acquire spatial information, animals must be sacrificed, and analytics performed *ex vivo* on the dissected pieces, which is essentially the opposite of *in situ* detection. Still, MS is a convenient technique to record the biodistribution of drugs *ex vivo*. Different components of NPs and loaded pharmaceutical agents can be labeled to enable element-specific detection with ICP-MS,<sup>52,63</sup> and different organic ligands and pharmaceutical compounds can also be directly detected by MS.<sup>64</sup> This strategy has been applied in models of NP-based drugs, in which biodistributions of metal-containing NPs have been recorded *ex vivo*.<sup>15,65,66</sup> Recent progress now also allows applying MS *in vivo*, by using picosecond-infrared-lasers (PIRL) for scar-free minimally invasive surgery and MS analyses of the ablated tissue.<sup>67,68</sup> This advance has led to the development of MS microscopes.<sup>69,70</sup> While MS microscopes enable detailed analyses of molecular species, and thus imaging of the different parts of NP-based drugs, *in situ-in vivo* analyses of NP-based drugs deep inside tissue remain complicated. For example, it is straightforward to probe the NPs with the surface region of tissue fragments using PIRL-coupled MS methods, but reaching tumors deep inside a tissue with the laser, followed by *in situ* extraction of tissue fragments for mass spectrometry analyses (of the presence of NPs), has not thus far been demonstrated.

Alternatively, electron microscopy (EM) techniques such as transmission electron microscopy (TEM) and scanning electron microscopy (SEM) allow imaging cells with extremely high resolution. Moreover, experimental approaches such as cryo-electron tomography coupled with focused ion-beam milling provide three-dimensional (3D) images of organelles and large protein structures inside cells.<sup>71–73</sup> While the development of liquid-phase supports for EM allows studying samples over time in biologically relevant environments,<sup>74</sup> it is not yet clear whether imaging live cells will be possible.<sup>75–77</sup> Finally, EM techniques also permit direct detection of metals with adequate sensitivity through spectroscopic methods such as energy dispersive X-ray analysis (EDX) and electron energy loss spectroscopy (EELS).<sup>63</sup> However, EM is not capable of imaging deep inside tissues and cells. Although it can be possible to image thin parts of intact whole cells (*i.e.*, 500 nm) using cryoEM (at a voltage of 300 kV), EM traditionally requires extensive sample preparation (mostly using thin sections of fixed cells), making *in situ* usage impossible.

Visualization of NP-based drugs can be accomplished *in situ via* different standard medical imaging techniques. A comprehensive overview of techniques suitable for imaging of NP carriers is beyond the scope of this Review, but a number of relevant recent reviews can be recommended.<sup>78,79</sup> In particular, MRI and PET/SPECT enable performing analyses on small animals and humans. Both PET and SPECT require radio-labeling of the different NP components with different radioactive traces (*e.g.*, one for the pharmaceutical agent and one for the matrix of the carrier vehicle) in order to follow the fates of the different entities by performing different

(multiplexed) imaging experiments. Imaging deep inside tissue *in vivo* is possible, but spatial resolution is limited. Nevertheless, only information about the location of the radio-labeled compounds can be obtained, but not about their molecular state (e.g.,  $^{64}\text{Cu}$  or  $^{64}\text{Cu}^{2+}$  cannot be distinguished, excluding for example the identification of changes in the surface chemistry of Cu NPs). Imaging deep inside tissue with up to near-cellular-level resolution (below  $10\ \mu\text{m}$ ) can be achieved with MRI.<sup>80–82</sup> Element-based MRI diagnostics (e.g.,  $\text{Gd}^{3+}$ ,  $\text{Mn}^{2+}$ )<sup>83,84</sup> and NP-based MRI diagnostics (e.g.,  $\text{MnO}$ ,  $\text{Fe}_3\text{O}_4$ )<sup>85,86</sup> can avoid the use of radioactive elements and have been used to monitor signal changes of NPs within tumor mass. By using functional MRI, local chemical information can be provided in some cases.<sup>87</sup> Multiplexed imaging is possible by using different elements ( $^1\text{H}$ ,  $^{13}\text{C}$ ,  $^{19}\text{F}$ , etc.). However, the diagnostic outcome of MRI is also closely dependent on the resolution of MRI equipment. In addition, there can be nonlinear signal responses to concentration of agent and endogenous changes in contrast that can create uncertainty in the measurements, and signal intensity and imaging resolution are not yet sufficient to reach subcellular levels.<sup>88</sup>

While scarcely used in clinics, optical imaging (fluorescence and bioluminescence) is one of the most commonly used imaging techniques in preclinical settings, in particular for *in vitro* imaging of cell/tissues (both fixed or live) and for *in vivo* imaging of small animals, due to its low cost, rapid throughput, and multiplexing ability. However, we note that it is not highly accurate for determining biodistribution. Other than the localization of fluorescently labeled molecules/structures, it can also provide information about the local microenvironment by using analyte-sensitive fluorophores.<sup>89</sup> Multifunctional NPs have been developed as biocompatible probes of external stimuli, such as force sensors. For example, ceramic NPs doped with lanthanide ions have been widely used as temperature, electric field, and pressure sensors for MRI (with gadolinium) and for biomarker detection using their upconversion.<sup>90,91</sup> In principle, fluorescence imaging is also possible in humans, though there are many limitations, primarily that it is limited to imaging structures  $<1\ \text{cm}$  from an endothelial surface.<sup>92</sup> Fluorescence allows tracking of pharmaceutical agents and NP carriers by measuring organ distribution and subcellular localization. Commonly used NIR fluorophores (e.g., IR780, chlorin e6) enable monitoring the changes of NP-based drugs in tumors over time and can also be combined with photothermal or photodynamic therapy to integrate cancer diagnosis and treatment.<sup>93–95</sup> The above-mentioned lanthanide dopants, besides facilitating upconversion (*i.e.*, when irradiated with NIR light, emitting in the visible), can also be used as markers for X-ray fluorescence or nanoscintillator-driven photodynamic therapies.<sup>96–98</sup>

Fluorescence can be detected with spatial resolution (*i.e.*, recording images) down to the level of single molecules and also with temporal resolution (*i.e.*, enabling fluctuation-based correlation analyses such as fluorescence correlation spectroscopy, or in combination with spatial resolution, enabling the recording of movies). Although the standard diffraction-based resolution limit of light is a few hundreds of nanometers, super-resolution and near-field approaches have pushed recordings to spot sizes of only a few nanometers.<sup>99–102</sup> Exceptional spectral resolution permits a multiplexed recording of the fluorescence originating from

different fluorophores,<sup>17</sup> see Figure 2. Finally, changes in the local environment of the imaged drug can also be

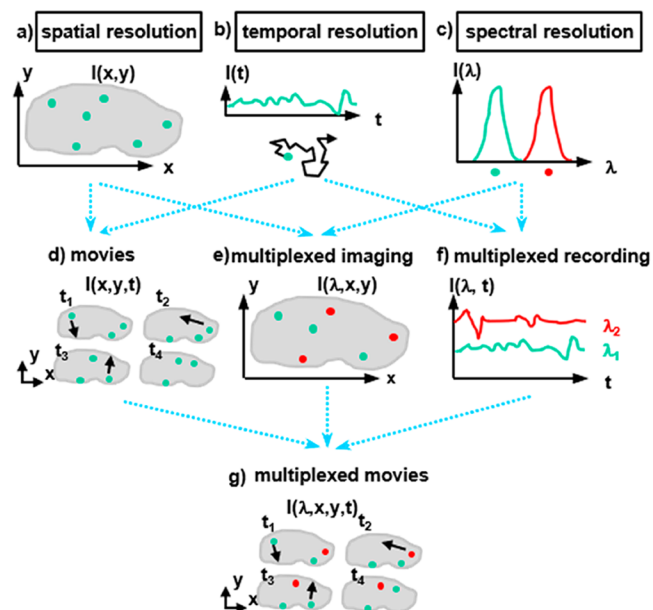


Figure 2. (a) Spatial resolution allows recording monochromatic images, such as the distribution  $I(x,y)$  of one type of fluorophore within one cell. (b) Temporal resolution allows recording intensity fluctuations  $I(t)$  at one point, which with correlation analysis enables diffusion measurements of fluorophores. (c) Spectral resolution permits discrimination of the fluorescence  $I(\lambda)$  of fluorophores emitting at different wavelengths,  $\lambda$ . (d) Spatial and temporal resolution taken together allow recording of monochromatic movies, such as the movement of one type of fluorophores within one cell. (e) Spatial and spectral resolution taken together allow recording multicolor images, such as the distribution of different fluorophores in one cell. (f) Temporal and spectral resolution together enable multiplexed recording of intensity variations of multiple fluorophores. (g) Taking spatial, temporal, and spectral resolution together makes it possible to record multicolor movies, such as recording the movement of multiple different fluorophores in one cell.

detected, both qualitatively and quantitatively, by using analyte-sensitive reporter fluorophores. The use of fluorescence-based analytics is therefore a powerful methodology, but not without its practical limitations. Maybe the greatest obstacle for its use in many “real” samples is light scattering, see Figure 3.

For fluorescence measurements, a fluorophore needs to be optically excited, and the resulting fluorescent emission needs

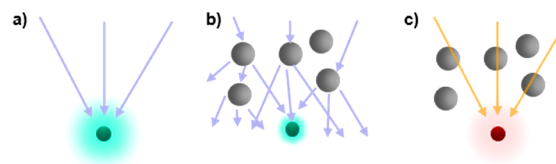


Figure 3. (a) Visible light can be focused to a fluorophore. (b) In the case of scatterers in the path, the focus is diffused, limiting spatial resolution as well as the intensity that arrives at the fluorophore. (c) In case wavelengths are used at which no scattering occurs with the intermediate material, the illumination path would remain unaffected.

to be recorded with a detector. To achieve spatial resolution and to maximize the excitation probability, the stimulating radiation should be focused as tightly as possible to the position of the fluorophore (see Figure 3a). However, in many “real” samples, the incoming beam encounters obstacles in the form of light scattering. This scattering limits focus, leading to reductions in the spatial resolution and effective excitation probability at the target (see Figure 3b). Consider the fluorescence of a fluorophore in water *versus* milk. It is relatively simple to record the emission of a standard fluorophore in water; however, milk is an emulsion and scatters light, thereby appearing opaque to visible light. This scattering affects both the excitation and emission, hampering fluorescence measurements. The interiors of cells growing as two-dimensional (2D) monolayer cultures can be probed using fluorescence imaging. These measurements can be used, for example, to detect specific molecules using immunostaining<sup>103</sup> or to track individual molecules.<sup>104</sup> However, the same measurements would no longer be possible if the cell to be probed lay 1 mm deep inside three-dimensional (3D) tissue. As such, light scattering is a fundamental problem to acquire fluorescence measurements in tissue and full organisms efficiently. Visible light is strongly scattered by both biological tissues and inhomogeneous fluids, such as blood. The overall absorption of the light used for irradiation as well as the emission from the fluorophores by the different components of the sample hampers the useful penetration depth of optical microscopy. Penetration limits of optical imaging can be avoided by combining it with intraoperative or endoscopic procedures, yielding imaging methods that have already been translated for use in humans, but are highly invasive, as most require surgical intervention. Alternatively, tissue penetration issues caused by absorption and scattering can be partially solved by working in the so-called spectral “biological window”,<sup>105</sup> which designates the reduced scattering of light by tissue in the NIR region. Therefore, scattering and absorption effects can be reduced by shifting the wavelength of the beam used for the irradiation of a sample from visible to NIR light.<sup>106</sup> Alternatively, two-photon microscopy uses longer wavelength photons to excite fluorophores, achieving deeper penetration. As such, two-photon intravital microscopy enables important *in vivo* and *in situ* insight into fundamental biological processes (e.g., immunological responses) occurring 100–200  $\mu\text{m}$  deep within animals.<sup>107–109</sup> While two-photon imaging techniques also suffer from optical scattering, advances in modern image analysis, applying effective and adaptive Fourier filtering algorithms (FFA), promise to improve image quality and analyses.<sup>110,111</sup> Despite these advances, acquisition of high-resolution optical recordings deep within tissue is not possible using existing methodologies. One could dissect the specimen, but that would exclude *in situ* and longitudinal detection. While such *ex vivo* analyses can be done in animal experiments, it is ruled out for most clinical applications in humans. Thus, tissue effectively remains nontransparent to analytics based on visual light optics.

Raman microscopy presents an alternative and a complement to the methods discussed above. Although Raman microspectroscopy has been used frequently for the characterization of tissues and cells,<sup>112</sup> the intrinsic low Raman cross sections of NPs, especially with infrared light, limit its applicability in bioimaging. The intensity of conventional Raman scattering, however, can be enhanced by many orders

of magnitude when the target molecules are located close to plasmonic surfaces, giving rise to the so-called surface-enhanced Raman scattering (SERS).<sup>113</sup> Whereas most applications of SERS have been directed to the analytical detection of molecules at low concentrations, direct SERS spectroscopy has also been used in the classification and characterization of tissues<sup>114</sup> and cells.<sup>115,116</sup> The intrinsic complexity of these biological samples makes the spectral output of the direct use of SERS difficult to interpret. Thus, as an alternative to direct SERS, labeled particles known as SERS tags or SERS-encoded NPs have been developed specifically for imaging. Such particles typically comprise a metal (Au or Ag) NP core, on which molecules with high SERS cross-section are adsorbed. Then, the particle is protected with an oxide or a polymer material that, in turn, can be functionalized with targeting biomolecules.<sup>117</sup> The SERS tags can be used for bioimaging, with the advantage that the signal can be readily excited with NIR lasers, circumventing the photodegradation common to visible lasers.<sup>118</sup> Applications *in vivo* have been reported using fiber optics-based illumination and signal collection, which enables acquiring images as deep as a few millimeters (or even centimeters) within the subject, but only with moderate spatial resolution.<sup>119,120</sup> Although high-resolution imaging is more challenging, recent reports demonstrate the possibility of using confocal SERS to classify cell types, both in 2D<sup>121</sup> and in 3D<sup>122</sup> cell co-cultures. Additionally, as SERS is a surface active methodology, changes in the local environment of the metal NP can be detected, such as conformation of adsorbed proteins.<sup>123–125</sup> Thus, SERS potentially enables one to follow the fate and degradation of NP-based drugs, also *in vivo*.<sup>126</sup> Nonetheless, resolution and penetration depth are hindered by the same issues discussed for fluorescence imaging above, while acquisition times for SERS images are still typically much slower than those for fluorescence.

Photoacoustic imaging (PAI) is another optical imaging modality to monitor NP-based drugs, labeled macromolecules and/or cells, combining the sensitivity of fluorescence imaging with the high spatial resolution of ultrasound imaging. This method measures the echo waves initiated from the heat generated by a laser beam and subsequently thermo-elastic expansion of the tissue and is capable of greater spatial resolution when imaging NPs deep within tissues compared to fluorescence imaging.<sup>127</sup> For instance, PAI has been widely utilized to investigate the distribution of different Au NPs.<sup>128</sup> The strong localized surface plasmon resonance (LSPR) effect in Au NPs enables tunable photoacoustic absorption *in vivo*. Alternatively, a series of protein nanostructures filled with gas generated by some microorganisms can be used as PAI contrast agents and enable to probe macrophage phagocytosis and lysosomal degradation in the liver of living animals.<sup>129–131</sup> Single-walled carbon nanotubes (SWNTs) can also be monitored *in vivo* with a wide PA absorption spectrum without specific peaks. Other suitable candidates for PAI include NPs loaded or labeled with organic photoacoustic contrast agents, such as cyanine-based dyes, melanin, and porphyrin.<sup>132</sup> Similar to fluorescence imaging, the NIR window (780–900 nm) and the second NIR window (900–1700 nm) are optimal for *in vivo* applications in order to avoid laser absorption from endogenous agents such as hemoglobin.<sup>133</sup> Multiplexed PAI enables the quantification of signals from NPs, oxygenated hemoglobin, and deoxygenated hemoglobin separately, but

**Table 2. List of X-ray Imaging, Spectroscopy, and Scattering Techniques Commonly Used to Study the Biodistribution or Fate of Nanoparticle (NP) Drugs in Biological Samples**

<i>Imaging</i>				
	Signal detected	Uses	Limitations	Advantages
<b>TXM/STXM</b>	X-ray transmitted through a sample	<ul style="list-style-type: none"> <li>• Imaging of hard and soft tissues</li> <li>• Suitable to image subcellular morphology</li> <li>• Biodistribution of NPs</li> </ul>	<ul style="list-style-type: none"> <li>• Resolution depends on size of the beam</li> <li>• High resolution or large field of view</li> <li>• Cannot image unstained specific molecules</li> </ul>	<ul style="list-style-type: none"> <li>• Good detection of metal NPs</li> <li>• Allows elemental mapping using advances approaches.</li> </ul>
<b>XRF/XFI</b>	Element specific X-ray emission	<ul style="list-style-type: none"> <li>• Biodistribution of NPs</li> <li>• Degradation of NPs</li> </ul>	<ul style="list-style-type: none"> <li>• Large biological samples absorb and scatter the signal, making detection of NPs difficult</li> <li>• Slow acquisition</li> <li>• Resolution depends on size of the beam</li> <li>• High resolution or large field of view</li> <li>• Hard to detect cell organelles</li> </ul>	<ul style="list-style-type: none"> <li>• Good detection of metal NPs</li> <li>• Element specific</li> <li>• Can be combined with other imaging and spectroscopic techniques</li> </ul>
<b>CDI-Phase contrast imaging</b>	Changes in the phase of X-rays	<ul style="list-style-type: none"> <li>• Imaging of hard and soft tissues</li> <li>• Imaging the same sample from macroscopic to cellular scale</li> <li>• Biodistribution of NPs</li> </ul>	<ul style="list-style-type: none"> <li>• Cannot differentiate between chemical elements</li> <li>• High resolution or large field of view</li> <li>• Cannot be combined with perform spectroscopic techniques</li> </ul>	<ul style="list-style-type: none"> <li>• Non-destructive</li> <li>• efficient imaging of unstained soft tissues</li> <li>• promising for <i>in vivo</i> applications</li> <li>• Good detection of metal NPs</li> <li>• Allows sequential imaging of a sample with increasing resolution</li> <li>• Can be combined with other imaging techniques</li> </ul>
<b>SAXS imaging</b>	X-ray scattered by the sample	<ul style="list-style-type: none"> <li>• Imaging of hard and soft tissues</li> <li>• Imaging complex organization of biological samples</li> </ul>	<ul style="list-style-type: none"> <li>• Hard to detect cell organelles</li> <li>• Cannot differentiate between chemical elements</li> </ul>	<ul style="list-style-type: none"> <li>• Can map nanoscale morphology of NPs in complex biological environments</li> <li>• Can determine complex organization of cells and molecules within biological samples</li> </ul>
<b>Ptychography</b>	Combination of CDI with scanning approaches	<ul style="list-style-type: none"> <li>• Imaging of hard and soft tissues</li> <li>• Biodistribution of NPs</li> </ul>	<ul style="list-style-type: none"> <li>• Cannot differentiate between chemical elements</li> </ul>	<ul style="list-style-type: none"> <li>• Wavelength limited resolution</li> <li>• Compatible with thick specimens</li> <li>• Can be combined with other imaging techniques</li> </ul>

Table 2. continued

<i>Spectroscopy and Scattering</i>				
	Property probed	Uses	Limitations	Advantages
<b>XAS (XANES, EXAFS)</b>	Local electronic environment of inner shells of metal atoms	<ul style="list-style-type: none"> <li>• Degradation of NPs</li> <li>• Transformation of chemical properties and structure of NPs</li> <li>• Changes in size or shape of NPs</li> <li>• Interaction of NPs with biomolecules</li> <li>• Reactivity of NPs in biological environments</li> </ul>	<ul style="list-style-type: none"> <li>• Requires high concentrations of NPs</li> </ul>	<ul style="list-style-type: none"> <li>• Element specific</li> <li>• Provides information on chemical and physical properties of NPs</li> <li>• Can be applied easily to tissue and cell samples</li> <li>• Can be combined with other imaging techniques</li> </ul>
<b>XES-RIXS</b>	Local electronic environment of inner shells of metal atoms	<ul style="list-style-type: none"> <li>• Degradation of NPs</li> <li>• Transformation of chemical properties of NPs</li> <li>• Reactivity of NPs in biological environments</li> </ul>	<ul style="list-style-type: none"> <li>• Requires high concentrations of NPs</li> </ul>	<ul style="list-style-type: none"> <li>• Element specific</li> <li>• Provides information on chemical properties of NPs</li> <li>• Complementary to XAS</li> <li>• Better energy resolution than XAS</li> <li>• Does not require monochromatic X-rays</li> </ul>
<b>XPCS</b>	Scattering properties of NPs	<ul style="list-style-type: none"> <li>• Degradation of NPs</li> <li>• Aggregation of NPs</li> <li>• Determine hydrodynamic properties of NPs in biological fluids</li> </ul>	<ul style="list-style-type: none"> <li>• Not element specific</li> <li>• Requires high concentrations of NPs</li> <li>• Limited by beam damage</li> <li>• Requires high X-ray coherence.</li> <li>• Difficult to interpret as Biological samples exhibits complex dynamics over many time and length scales</li> </ul>	<ul style="list-style-type: none"> <li>• Provides information on NPs and biological systems of different length scales</li> <li>• Provides dynamic information on colloidal and hydrodynamic properties of NPs</li> </ul>
<b>XPS</b>	Local electronic environment of external orbitals of metal atoms	<ul style="list-style-type: none"> <li>• Degradation of NPs</li> <li>• Chemical changes in the surface of NPs</li> </ul>	<ul style="list-style-type: none"> <li>• Lower sensitivity than XAS</li> <li>• Only can be used to probe the surface of NPs</li> </ul>	<ul style="list-style-type: none"> <li>• Element specific,</li> <li>• Provides information on chemical properties of the surface of NPs</li> <li>• Can be applied easily to tissue and cell samples</li> </ul>
<b>SAXS USAX WAXS</b>	Scattering properties of NPs	<ul style="list-style-type: none"> <li>• Degradation of NPs</li> <li>• Changes in size, shape or aggregation state of NPs</li> </ul>	<ul style="list-style-type: none"> <li>• Not element specific</li> <li>• Difficult to interpret as Biological samples are complex systems over many length scales</li> </ul>	<ul style="list-style-type: none"> <li>• Quick acquisition</li> <li>• Can be applied <i>in situ</i></li> <li>• Provides information on NPs and biological systems of different length scales</li> <li>• Can be applied easily to tissue and cell samples</li> </ul>
<b>Total X-ray Scattering</b>	Scattering properties of NPs on a surface	<ul style="list-style-type: none"> <li>• Interaction of NPs with biological membranes</li> </ul>	<ul style="list-style-type: none"> <li>• Only can probe surfaces</li> </ul>	<ul style="list-style-type: none"> <li>• Provides information on the binding mode of NPs to membranes and other surfaces.</li> </ul>

remains a limitation for PAI. Thus, PAI has great potential for use in investigating pharmacokinetics, biodistribution, stem cell homing, metastasis dynamics, *etc.* Presently, PAI is used mostly in research laboratories to follow blood flow, plaque formation in blood vessels, and blood vessel elasticity. Instruments approved for clinical application are not yet available, limiting the widespread use of this method.

Optical coherence tomography (OCT) is a non-invasive optical imaging technique that may be used in combination

with PAI to measure the time delay from photons backscattered by samples irradiated with low-coherence NIR or visible light.<sup>134</sup> This method is widely used *in vivo*, especially in the eye, and measures the morphology of tissues with millimeter penetration depth and micrometer resolution.<sup>135–137</sup> NPs can be used as contrast agents for OCT.<sup>138–141</sup> Therefore, OCT might also help to detect NP-based drugs in biological environments and can be used

to probe the biodistribution and/or behavior of such nanomaterials *in vivo*.<sup>142</sup>

Due to the noted limitations of the above-discussed imaging techniques, especially with respect to penetration depth, there are clear needs for the development of further methodologies for the *in situ* and *in vivo* analyses of NP-based drugs. In the following section, the use of X-ray-based analytics to characterize and to image NP-based drugs will be discussed as methodologies with significant potential in this context. Capabilities for such measurements *in situ* in complex biological environments such as blood, *in vitro* in cells and tissue, and ultimately *in vivo* in animals and humans will be outlined. While this Review focuses on NP-based drugs, the concepts discussed herein apply to the characterization of nano–bio interactions in general.

### X-RAY-BASED TECHNIQUES AS AN ALTERNATIVE TO STUDY NANOPARTICLE-BASED DRUGS IN BIOLOGICAL ENVIRONMENTS

Visible light is an electromagnetic wave within a specific range of wavelengths  $\lambda$ . Scattering imposes limits to visible light-based imaging, but scattering is highly wavelength dependent ( $\lambda^{-4}$ ) and therefore can be reduced by shifting the optical excitation from the visible to the NIR.<sup>143–145</sup> Alternatively, it is possible to reduce the scattering of the incident light further and to achieve deeper tissue penetration by shifting fluorescence-based methodologies to a different spectral range, such as X-rays. Standard X-ray projection imaging in a physician's office allows visualizing bones deep inside the body in contrast to surrounding soft tissues and is also used clinically in hospitals in the form of computed tomography (CT).<sup>146</sup> X-ray-based medical imaging remains by far the most commonly used method, exceeding the use of all other imaging techniques combined. This technique is based on the differential X-rays attenuation in different organs, which depends on the elemental composition (mostly O, C, H, and N for biological tissue, but bone contains high quantities of heavier Ca) and tissue density.<sup>147</sup>

Such dramatic changes in wavelength alter the fundamental interactions of light with matter, as many phenomena, such as absorption, fluorescence emission, and scattering, are wavelength dependent. For example, X-rays can carry enough energy to excite electrons located in orbitals at the inner shells of heavy elements, whereas optical techniques normally study electronic transitions only between valence orbitals. Therefore, X-ray-based techniques such as X-ray fluorescence (XRF),<sup>148,149</sup> or for *in situ/in vivo*, also called X-ray fluorescence imaging (XFI), or X-ray absorption spectroscopy (XAS)<sup>148,150,151</sup> enable direct detection of the different components in NP-based drugs (Table 2). Due to the characteristic discrete electronic levels of different elements, XRF is element specific, and thus multiplexed detection is possible.<sup>148,149,152</sup> Furthermore, as the chemical environment also changes the electronic levels, information about the electronic and chemical states of the elements under study can be obtained by using XAS.<sup>150,151,153</sup> As X-ray scattering occurs on the basis of the electron shells of atoms, the sizes of labels reduce to the sizes of individual atoms. However, working with biological samples requires consideration of radiation-induced toxicity, which is a particular concern with X-ray radiation.

X-ray-based techniques may fully or partially solve some of the problems of fluorescence-based analytics and constitute a

valuable alternative to optical imaging for the study of NP-based drugs *in situ* (Table 2). This set includes a number of spectroscopic techniques such as XRF, XAS, and X-ray emission spectroscopy (XES), among others. There are also scattering techniques, such as powder X-ray diffraction (PXRD), total X-ray scattering, or SAXS imaging,<sup>154</sup> X-ray phase contrast imaging techniques,<sup>155–157</sup> and X-ray photon correlation spectroscopy (XPCS).<sup>158–162</sup> These techniques could be used to probe nanomaterials directly, including NP-based drugs, and to provide important information about their location, quantification, state, and supramolecular arrangements.

In fact, X-ray-based techniques are frequently used to characterize NP syntheses and properties. We first start with a short summary on how such techniques are used to characterize NPs under laboratory conditions (*e.g.*, dissolved in water), for example, to monitor their synthesis and assessing their materials' properties. Based on this information, prospects for extending such approaches to "biological" environments will be discussed.

Detailed analyses of PXRD data for NPs can provide useful insights into size, shape, crystal structure, crystallinity, and sample purity.<sup>163</sup> Amorphous or poorly crystallized components of a sample are not detectable by PXRD, so NPs that do not have a crystalline core will not be observed with diffraction. The most interesting properties of NPs are caused by quantum confinement as a result of their small sizes. But it is precisely these small sizes that make it challenging to obtain a solid and reliable characterization of the synthesis of NPs *in situ*. The peaks in PXRD patterns of NPs get considerably broader as NP size decreases, leading to lower signal-to-noise ratios and making it challenging to identify phases and to evaluate purity. TEM and SEM, optical measurements, nuclear magnetic resonance, or MS techniques are generally used to obtain information about size, composition, and chemical environment of NPs, and these techniques can be used in conjunction with PXRD to provide additional insights into the characteristics of samples. However, despite their suitability to study NP samples, there remain considerable limitations with regard to their applicability to *in situ* studies (*i.e.*, including extensive sample preparation requirements, of specific solvent requirements or vacuum conditions, low sensitivity, or incapacity of separating between the different populations found within the growing particles). A wide variety of X-ray-based techniques have been used to characterize the structure, composition, size, or aggregation state of NPs (*e.g.*, SAXS, wide-angle X-ray scattering (WAXS), XRF, XAS, PXRD, pair distribution function (PDF), and X-ray photoelectron spectroscopy (XPS)).<sup>164</sup> In most cases, the small X-ray scattering cross sections of NPs impose the need for synchrotron-radiation-based techniques. Despite the possibility of characterizing NPs of different types, the dynamic character of synthetic processes leads to the need for *in situ* studies. Control of the syntheses of NPs, from their nucleation and growth to the attachment to other NPs or conjugation with biological ligands/pharmaceutical agents, would benefit heavily from monitoring the reactions involved *in situ*. These measurements would enable not only observing the evolution of the NPs in real time but also obtaining data without any disruption of the initial structure. The breakthroughs in this field will come from the possibility to combine different characterization techniques to study the synthesis and

properties of NPs in their different stages. Indeed, the use of microfluidic devices to perform both synthesis and *in situ* characterization offers enormous potential. At this point, it is critical to consider the interface of the reaction container. Inexpensive, X-ray-transparent polyimide windows are suitable for *in situ* X-ray characterization, for example, by means of SAXS, WAXS, XAS, or PDF. However, other promising techniques, such as XPS or MS, require vacuum conditions. Therefore, while the use of flow reactors is a reality, combining multiple interfaces that allow the successful application of several X-ray-based techniques at different time windows of the reaction represent real challenges in this context.

These techniques could also be applied to a wide variety of NP-based drugs. Conversely, the identification of ideal drug delivery systems to study under X-ray techniques can facilitate the use of existing infrastructure to observe nano-bio interactions that previously could only be inferred. For example, crystalline materials such as liposomes, metal NPs, and metal-organic frameworks (MOFs)-based NPs have distinct X-rays scattering profiles. In particular, MOFs can also be loaded with therapeutics and engineered to disassemble in acidic microenvironments, meaning that dissolution of the MOF carrier system could be monitored by SAXS. This process would not require any labels and would also give information on whether the NPs fracture to release cargo, to disassemble into crystallites, or to dissolve completely during internalization. The reverse time course (formation instead of dissolution) has been performed by looking at the formation of MOFs on the cell walls/membranes of microorganisms.<sup>165</sup> Further, SAXS has recently been used to monitor the cellular uptake and interactions of cubic liposomes (cubosomes) in a microfluidic setup. Roughly 16 min after interacting with the cells, the cubosomes demonstrated a phase transition and evolved into hexasomes, a phenomenon that would not have been observable without X-ray techniques.<sup>166</sup> Theoretically, X-ray absorption near-edge structure (XANES) spectroscopy and XRF can similarly be used to monitor whether the metal state changes and how the loaded drug is released, due to its proximity to the metal center. In particular, the protein corona will also dictate whether changes in the microenvironment can be observed after internalization, as demonstrated by *in situ* extended X-ray absorption fine structure (EXAFS) measurements of TiO<sub>2</sub> NPs, which revealed no fine structure change upon internalization into cells from cell media.<sup>167</sup> Other EXAFS work has also confirmed that small molecules may stay bound to NPs (maghemite) during internalization.<sup>168</sup>

The question is now how such *in situ* methods could be extended to *in situ-in vivo* measurements, that is, requiring the observation of NP samples not under test condition, but ultimately deep inside tissue. Modern development of synchrotron radiation sources allows for advanced beam properties, such as foci down to the range of a few nm,<sup>169-177</sup> excellent coherence, and brilliance exceeding 10<sup>21</sup> photons/(s·mm<sup>2</sup>·mrad<sup>2</sup>) at 0.1% bandwidth.<sup>178</sup> As such, measurements deep inside tissue with subcellular resolution are potentially possible. Therefore, these X-ray techniques constitute an exciting alternative to study the behavior and fate of NP-based drugs in biological systems at different length scales. Particularly, X-ray techniques can replicate, or might be able eventually to replicate, the

following types of measurements which are standard for fluorescence-based analytics:

Imaging (*i.e.*, spatial resolution) (see Figure 2a) based on X-ray transmission, fluorescence, (coherent) scattering, diffraction, or phase contrast techniques has been demonstrated using synchrotron radiation.<sup>57,149,154,179-182</sup> Furthermore, recently developed nanoprobe beamlines<sup>169-176,183</sup> possess advanced X-ray optics which are capable of focusing synchrotron radiation below 50 nm, allowing the use of X-ray imaging techniques to study biological samples with subcellular resolution.

Temporal resolution is possible (see Figure 2b), in particular when using a fast 2D pixel detector running at kHz or even MHz frame rates, ideally synchronized with the bunch pattern of the synchrotron radiation source.<sup>184,185</sup> For example, intensity fluctuation-based studies of the dynamics of objects scattering X-rays have been performed with XPCS using synchrotron radiation with highly coherent X-ray beams.<sup>186,187</sup> The scattering pattern is modulated by an interference pattern. Changes in this pattern are correlated to the motion of the scattering and thus to its diffusion coefficient (which provides information on the size and shape of the object).<sup>158-160</sup> The application of time-resolved techniques also allows studying the dynamics of metal centers upon photoexcitation and photoactivation.<sup>188</sup>

Spectral resolution (see Figure 2c) with X-rays is possible due to the characteristic discrete electronic levels of different elements. As such, X-ray absorption, fluorescence, and some X-ray inelastic scattering techniques (*i.e.*, resonant inelastic X-ray scattering, RIXS) are element specific. Multiplexed measurements of different elements such as Au, Cu, Fe, Ag, Pt, Os, *etc.* are thus possible.<sup>148,149,152,189-191</sup> Spectral resolution is even more important when studying the mechanisms of action of NP-based drugs, as it permits following various species of the same element that can be generated once the NP has been administered.<sup>192</sup> From the detector side, arrays of microcalorimeters hold potential for microspectroscopy applications using X-rays.<sup>193-196</sup>

Movies (see Figure 2d) are conceived as the combination of spatial and temporal resolution. Such experiments can be recorded using synchrotron radiation to probe biological samples.<sup>197,198</sup> However, in general, high spatial resolution or large image areas and high temporal resolution are still mutually exclusive. This limit is mainly due to two primary factors. First, biological samples normally contain low concentrations of the NPs of interest, making it necessary to use relatively long acquisition times on instruments providing high photon fluxes to obtain high-quality images. Furthermore, many X-ray imaging techniques use scanning-based approaches needing mechanical translation of the sample during acquisition, which takes longer for higher resolution images. This limitation holds true even for full-field imaging techniques, as the size of the field of view normally affects the final resolution of the image (*i.e.*, imaging larger fields of view leads to lower resolutions). Therefore, scanning approaches are still needed to image large areas of the sample with high resolution.

Multiplexed imaging (see Figure 2e) is possible, as different elements can be spectrally resolved using different techniques, which also allow achieving spatial resolution.<sup>199</sup> For example, the simultaneous acquisition of maps of different elements within a single XRF scan with synchrotron radiation is a clear example of well-established multiplexed imaging.<sup>149</sup> Further-

more, in multimodal imaging, XRF can be coupled also with other techniques such as XAS and XRD (at fluorescence microprobes), ptychography, transmission, and XRD simultaneously. Moreover, collecting images at different energies around an X-ray absorption edge permits imaging chemical states and electronic states which are compound specific. Similar to spectral resolution, detectors based on microcalorimeters may hold potential for multiplexed imaging as well.

Multiplexed recording might be possible with XRF (see Figure 2f). Parallel fluctuation analysis as recorded by XRF from different elements could be achieved using an energy-discriminating detector with high temporal resolution (kHz or more). Alternatively, XES should allow probing two orbitals within the same element with subnanosecond temporal resolution, by combining a van Hamos spectrometer<sup>200</sup> with fast detectors.

Multiplexed movies would involve the combination of spatial, temporal, and spectral resolution (see Figure 2g). This kind of measurement using X-ray-based techniques is currently at the technically possible limit, due to multiple technical restrictions (as described above) and by the maximum biologically tolerable dose. Nevertheless, there is no fundamental physical principle that would rule out multiplexed movies, although there are tremendous practical hurdles, and at the state of the art, multiplexed movies are not yet possible.

While the aforementioned examples are structured on a conceptual basis, in the following sections we will discuss the current aspects of employing X-ray-based techniques for their potential use in analyzing NP-based drugs *in situ* in more practical terms.

### X-RAY IMAGING OF NANOPARTICLE-BASED DRUGS (AND RELATED SYSTEMS) FROM THE SUBCELLULAR TO THE ANIMAL LEVEL

X-ray imaging has the potential to overcome the penetration depth limitation of EM and to image cellular components in fully intact cells with high spatial resolution and minimal sample preparation, *i.e.*, imaging biological material in a native or near-native state. Different from fluorescence imaging with visible/NIR light, synchrotron radiation-based imaging methods are capable of providing element-specific and precise distribution information on NPs at subtissue, cellular, and even organelle levels as well as the morphology information on biological specimens. The key factor here is the short wavelength of the X-rays. Whereas visible/NIR light suffers from low spatial resolution of a few 100 nm due to Abbe's diffraction limit and even super-resolution techniques thus far typically achieve only a few tens of nm spatial resolution in cells<sup>99,201,202</sup> (or 5 nm spatial resolution in nonbiological synthetic samples),<sup>203</sup> X-rays enable single nm spatial resolution, which is more than enough for the imaging of NP-based drugs. Also, by choosing the X-ray wavelength selectively, scattering effects by tissue can be minimized. This high resolution, however, comes with the price of potentially higher radiation damage than that caused by optical imaging techniques, which will be discussed in a separate section. Strategies for deep-tissue recordings will be discussed at the end of this section. For the majority of X-ray-based microscopies suitable for biological specimens, soft, tender, and hard X-ray wavelength ranges (which are discussed below) can be used as light sources, and each method has its

own advantages and drawbacks. Thus, the applicable imaging method should be chosen depending on the desired penetration depth, spatial resolution, and contrast mechanism.<sup>204</sup> In the case of inorganic NPs, X-ray-based imaging technologies can visualize the position and distribution of the NPs inside the cell/tissue *in situ*, without any further functionalization or labeling. Also, released heavy-element ions can be directly imaged. Loaded pharmaceutical compounds, however, may require tagging with atoms that provide enough contrast for the respective imaging method (unless they contain certain atoms such as Pt in the case of cisplatin). There are a variety of different methods for X-ray imaging, such as analyzing the phase contrast, absorption, fluorescence emission, or diffraction signals, *etc.*, of different elements/NPs. From these, several X-ray-based microscopies have been developed, which enable imaging in the field of nanobiotechnology,<sup>205–207</sup> both using soft and/or hard X-rays as light sources.<sup>181,182</sup> Examples include transmission X-ray microscopy (TXM), scanning transmission X-ray microscopy (STXM), micro- or submicro-focused XFI, and coherent diffraction imaging microscopy (CDI)/X-ray ptychography.

X-rays are ionizing radiation that can be divided into low penetrating soft X-ray (with energies from 100 eV to 1 keV, penetrating up to a few  $\mu\text{m}$ ), tender X-rays (energies from 1 to 5 keV), and high penetrating hard X-rays (wavelengths below 2 Å and energies above 5 keV). The interactions of photons with soft matter are dominated in the soft energy X-ray range by the photoelectric effect and in the hard X-ray energy range above 50 keV by Compton scattering. X-rays are orders of magnitude more penetrating than charged particles. The attenuation of the beam increases exponentially with the thickness of the sample and decreases with increasing X-ray energy. The intensity of the beam is attenuated by  $1/e$  (attenuation length) after transmission of soft tissue, for example, through 30  $\mu\text{m}$  (cell), 300  $\mu\text{m}$  (cell spheroid), 3 mm (tumor), and 30 mm (organ) at energies of 2.4, 5.4, 11.8, and 33 keV, respectively.<sup>208</sup> For radiography of the human chest in clinics, X-ray beams with maximum energies of 50–150 kV are used (*i.e.*, a beam composed of X-rays with a range of energies from a minimum of about 25 kV, depending on the filtering used, up to the maximum selected). The high penetration depth of X-rays can be employed to obtain real 3D imaging by tomographic methods, usually by computational reconstruction of virtual slices from a series of projections recorded at various angles. Being tiny and sparse, NPs in a tissue can only be investigated in 3D if the local tomographic resolution approaches the size of the NP itself, which requires coherent scattering techniques such as X-ray holotomography or ptychographic tomography and small sample volumes. The sensitivity for NPs can be increased by selecting XRF contrast. When composed of heavy elements inside a light matrix, NPs generate an XRF signal that can be efficiently separated from the background signal by energy dispersive detectors. XRF tomography enables measuring intrinsic trace element distributions with parts-per-million sensitivity in cells without the need to add or to encode genetically-specific fluorescent labels. However, the spatial resolution is limited by the X-ray optics used, to about 60 nm in 3D. Indeed, XRF tomography is a raster scanning technique utilizing a pencil beam, and as a consequence, this technique is comparatively slow. The measurement of a mega voxel 3D image can easily take several hours. On the other hand, XRF tomography

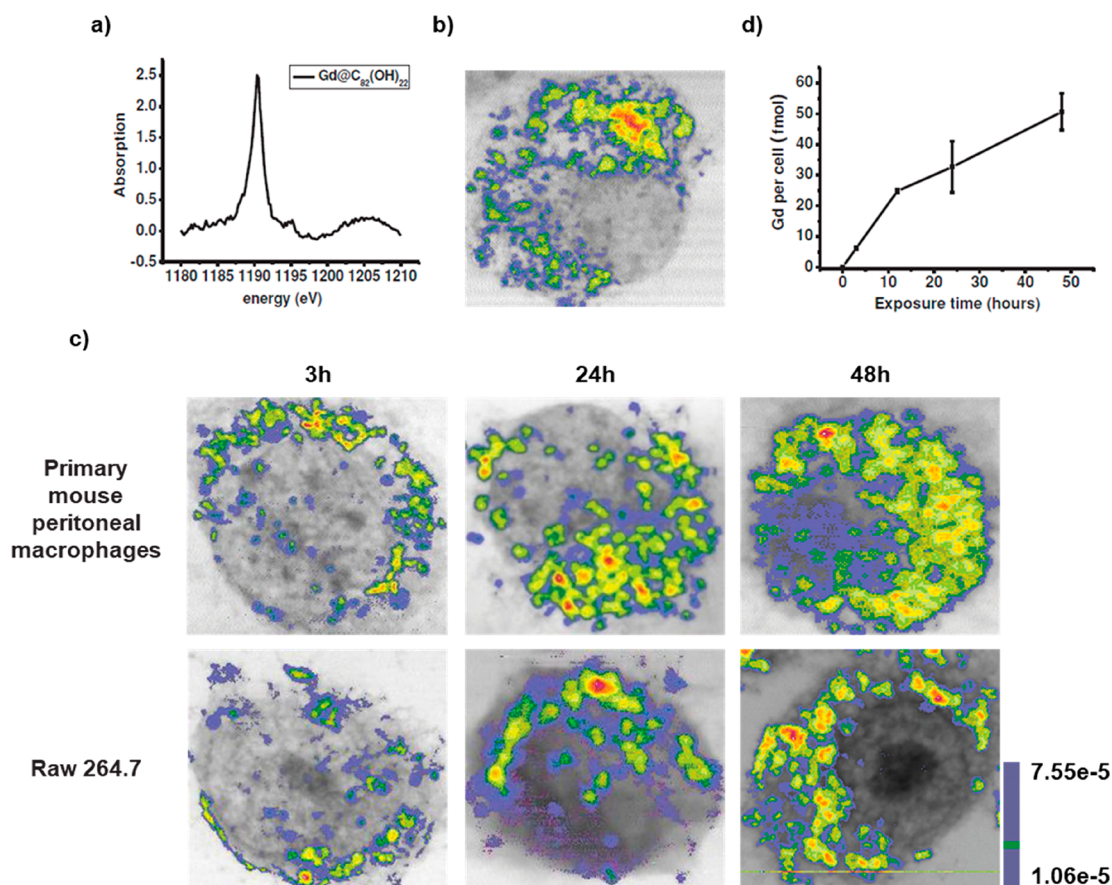


**Figure 4.** Internalization of metallofullerenol by macrophages *in vivo* and *in vitro*. (a) A Gd M5-edge XANES spectrum of Gd@C<sub>82</sub>(OH)<sub>22</sub> NPs. (b) Soft X-ray dual-energy contrast STXM images of Gd@C<sub>82</sub>(OH)<sub>22</sub> in a primary mouse peritoneal macrophage *in vivo*. (c) Soft X-ray dual-energy contrast STXM images of the time-dependent uptake of Gd@C<sub>82</sub>(OH)<sub>22</sub> NPs by primary mouse peritoneal macrophages and RAW 264.7 cells *in vitro*. (d) ICP-MS quantification of the time-dependent uptake of the NPs in macrophages of primary mouse peritoneal macrophages. Reprinted with permission from ref 210. Copyright 2014 John Wiley and Sons, Inc.

offers free spatial scalability. The size of the scanned volume is generally limited by the available measurement time once a suitable beam size is selected. For thick samples, the “over absorption” of the X-ray fluorescence radiation emitted from the NP inside the sample matrix is important. For Au NPs, for example, the L<sub>α</sub> radiation (9.7 keV) would transmit soft matter of 15, 150, and 1500 μm at 99.1%, 91.5%, and 41% intensity, respectively. A sample of 15 mm would be transmitted only at 0.0015% intensity. Using the high-energetic Au–K<sub>α1</sub> line (68.8 keV) would allow 75% and 5.6% transmission through 15 mm and 150 mm soft tissue, respectively.<sup>208</sup> The application of high energies for XRF microscopy requires dedicated sources, X-ray optics and detectors, and is discussed in a separate section below. At high-resolution conditions including coherent illumination, XRF tomography can be combined with ptychography, a scanning coherent X-ray diffraction imaging technique, to image the internal structures simultaneously, including organelles and distributions of trace elements within cells.<sup>209</sup> In ptychography, the effective numerical aperture of the imaging system can be increased, resulting in higher resolution than the size of the beam and imaging the natural contrast arising from internal electron density. Larger XRF tomographies may be combined with X-ray holotomography or phase contrast tomography to locate the NP position precisely relative to the tissue structure.

Soft X-ray-based microscopy is suitable for imaging the subcellular morphology together with the distribution of NPs/pharmaceutical agents in cells. As an example, Chen *et al.* used STXM to observe the continuous uptake and subcellular distribution of metallofullerenols in macrophages with 2D spatial resolution of 30 nm (Figure 4).<sup>210</sup> Taking images below and above the absorption edge provides elemental contrast in STXM imaging (dual-energy STXM). Cells were scanned at two energies, E<sub>1</sub> (1189 eV) and E<sub>2</sub> (1185 eV) just above and below the M5 absorption edge of the Gd atoms from Gd@C<sub>82</sub>(OH)<sub>22</sub>. The result showed that the Gd@C<sub>82</sub>(OH)<sub>22</sub> NPs were taken up by primary mouse peritoneal macrophages and RAW264.7 after 3 h exposure, and the content of Gd@C<sub>82</sub>(OH)<sub>22</sub> kept increasing over 48 h. The internalized Gd@C<sub>82</sub>(OH)<sub>22</sub> NPs were mainly located in the cytoplasm, but almost never entered into the nucleus (Figure 4).<sup>210</sup> Being element specific, this method is suitable for studying the distributions of elemental Gd, even when Gd is integrated with other NPs, such as in the case of Gd-hybridized Au@SiO<sub>2</sub>NPs (Au@SiO<sub>2</sub>(Gd)). With this method, both uptake and intracellular distribution of NP-based drugs were investigated. Hyaluronic acid (HA) and DOX were added to Au@SiO<sub>2</sub> (Gd) carrier NPs as pharmaceutical agents. With dual-energy STXM, the cellular uptake of these NP-based drugs was imaged in MDA-MB-231 cells.<sup>211</sup> Data showed a time-dependent uptake and how the intracellular localization of the Au@SiO<sub>2</sub> (Gd) NPs moved

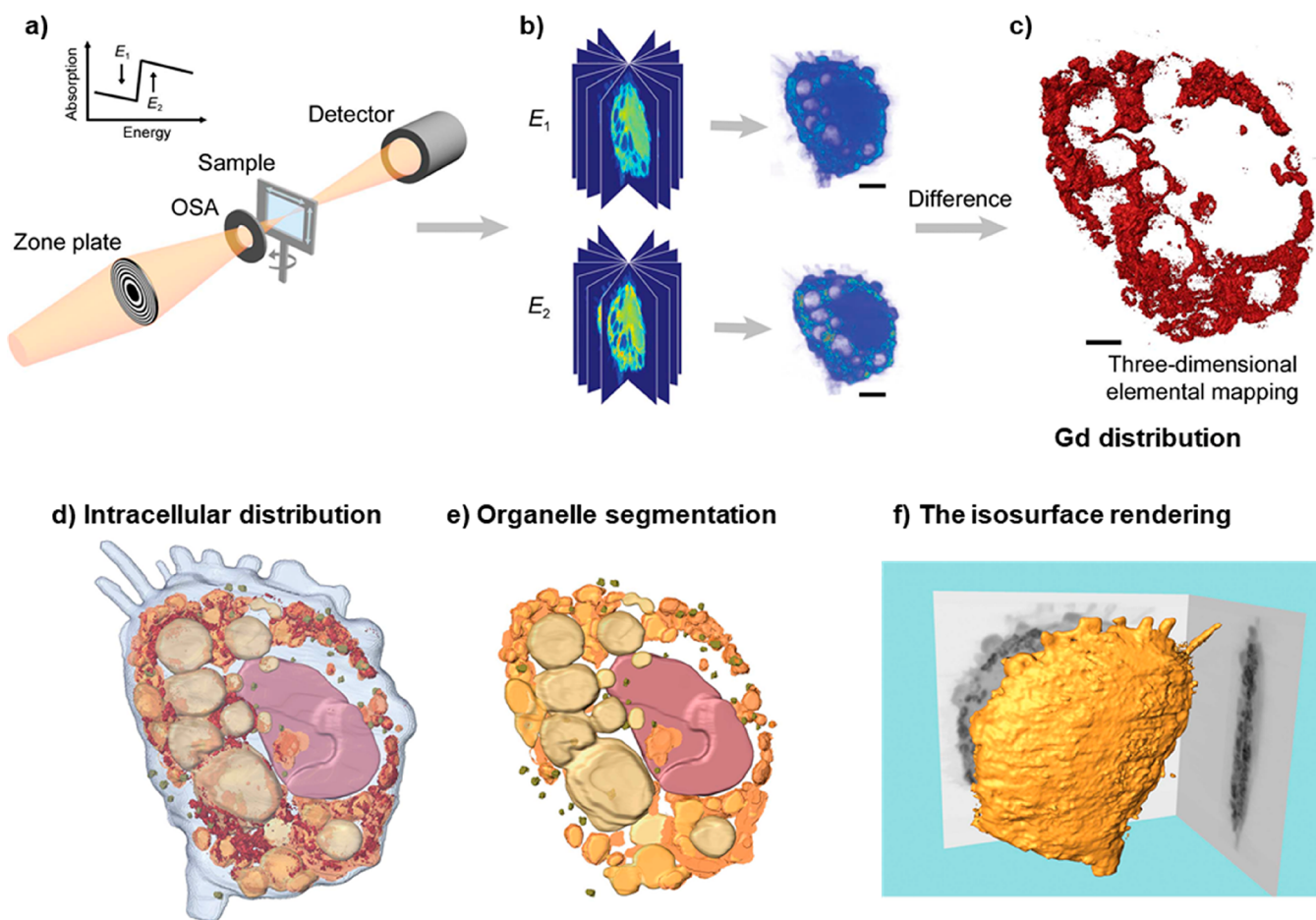


**Figure 5.** (a) Schematic layout of the dual-energy STXM imaging technique. Two sets of projections are acquired from various angles by STXM at energies below and above the absorption edge of the observed element, which in the reported work was Gd. (b) Tomographic data sets for both energies were separately reconstructed using the EST algorithm. (c) From this the quantitative 3D distribution of the specific element, here Gd, was obtained. (d) Intracellular distribution of Gd@C<sub>82</sub>(OH)<sub>22</sub>NPs. (e) Organelle segmentation based on differences in the linear attenuation coefficient and specific morphology of the different organelles. (f) Isosurface rendering of the macrophage at 1189 eV. Reprinted with permission from ref 214 under a CC-BY License. Copyright 2018 International Union of Crystallography.

from the membrane to around the cell nuclei. Reduced cellular uptake was detected when cells were pretreated with HA, verifying that the HA targeting modification efficiently enhances cellular uptake. These results on the internalization of Au@SiO<sub>2</sub> (Gd) NPs were in accord with data obtained with laser confocal scanning microscopy and TEM.<sup>211</sup>

In the aforementioned example, besides the 2D distribution, 3D ultrastructural imaging of the Gd@C<sub>82</sub>(OH)<sub>22</sub>NPs inside the cell was performed by combining dual-energy contrast STXM and equally sloped tomography (EST; Figure 5a,b). This method is a type of tomography where projections are acquired using a constant slope increment (instead of more common angle increments). This technique facilitates the use of iterative image reconstruction algorithms based on pseudopolar fast Fourier transform,<sup>212</sup> producing high-quality images with reduced exposure to radiation.<sup>213</sup> In this experiment, the detailed distribution of Gd@C<sub>82</sub>(OH)<sub>22</sub>NPs in macrophages was obtained (Figure 5c).<sup>214</sup> A large number of NPs were found to be aggregated within cells, and they were mainly located in phagosomes. No NPs were observed in the nuclei, which is in agreement with 2D imaging results. Based on the morphologies and the linear attenuation coefficients,  $\mu$ , of the organelles,<sup>215</sup> the 3D images

were segmented into subvolume regions, and the lysosomes, mitochondria, and nuclei could be segmented (Figure 5d). The quantitative analysis results of the segmentation suggest that the majority of aggregated NPs were only located in phagocytic vesicles, instead of other organelles, including the nuclei (Figure 5e). This method also can show the characteristic morphological features of macrophages, for example, the pseudopods, rough surfaces, and flat shapes (Figure 5f).

Recently, soft X-ray based TXM nano-CT has been applied to visualize *Escherichia coli* (AMR) cells. Data indicated that La@graphene oxide (GO) NPs are able to insert perpendicularly into the cell membrane, causing a number of irregularly shaped perforations, leading to disruption of the bacterial membrane and thus ultimately to killing the bacteria (Figure 6).<sup>216</sup> There are also examples of using soft X-ray CDI to obtain morphological information on some bacteria, green algae, viruses, chromosomes, etc.<sup>217–219</sup> The development of XRF tomography enabled the visualization of internal chemical elemental structure nondestructively, initially demonstrated in investigations of the freshwater diatom *Cyclotella meneghiniana* and later extended to the model organism *Caenorhabditis elegans* and others.<sup>220,221</sup> The chemical

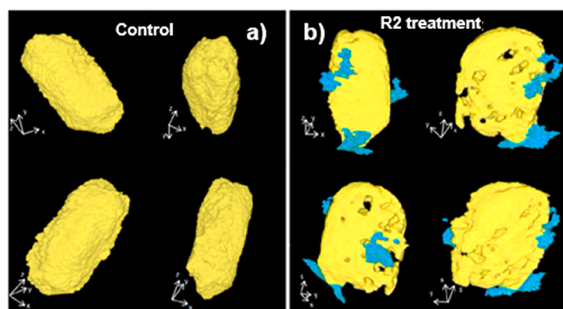


**Figure 6.** Nanocomputed tomography images of *Escherichia coli*: (a) untreated or (b) upon exposure to La@GO nanocomposites to decipher the bactericidal mechanism. Reprinted with permission from ref 216. Copyright 2019 American Chemical Society.

coordination of Cu within an intact organism was revealed using the four-dimensional combination of XRF XANES tomography, by mapping the distribution of cuprous and cupric complexes within *Drosophila melanogaster*.<sup>222</sup> The lack of sensitivity of XRF to lighter elements leads to a symbiotic correlation with ptychography, the latter technique particularly suited to revealing the structures of lighter elements.<sup>223,224</sup> STXM tomography, optical fluorescence, and 2D ptychography have also been correlated.<sup>189</sup>

Soft X-ray microscopy (XRM) is also suitable for recording tomography of heterogeneous atmospheric particulate matter. The morphology and the distribution of elemental Fe can be observed, which can help to understand biological phenomena caused by atmospheric particulate matter after entering the biological environment, which is of relevance for ecotoxicology.<sup>225</sup> Soft X-rays have strong interactions with organic materials, which limits the cell penetration to  $\sim 10\text{--}15\ \mu\text{m}$ , depending on different cell types<sup>226</sup> and the incident photon energies used.

As illustrated with the above examples, in addition to high spatial resolution, an important advantage of using soft X-rays for imaging is that cell membranes and intracellular structures can be imaged without the use of contrasting methods. This is a significant advantage over laboratory-based optical fluorescence microscopy imaging and OCT in the visible/NIR, where fluorescence staining of such structures is required, in order to correlate the location of NPs to intracellular organelles.<sup>103</sup> Standard thin-section TEM yields high-resolution images, but visualization of intracellular organelles requires staining,<sup>227</sup> and 3D tomography typically needs to be done by reconstruction of images obtained from different slices. Cryo-EM can image these organelles in 3D without staining, but only in thin parts of the cells (*i.e.*, 500 nm). Nevertheless, presently, soft X-ray techniques do not allow imaging different types of individual biological molecules in a cell directly, which would be important in investigating intracellular nano–bio interactions. Biomolecules such as proteins are small when compared with organelles or the complex structures found within them (*i.e.*, a few nm *versus* hundreds of nm respectively) and normally provide a low contrast independent of their type (unless they contain large quantities of heavier elements such as Fe). This issue makes it challenging to determine the location of a type of protein or to discriminate between different types of individual proteins using soft X-rays. However, the use of staining strategies might help to solve

this problem. For example, by using immuno-gold, it was possible to stain cellular components such as microtubules<sup>228</sup> or mitochondria.<sup>229</sup> Kong *et al.* reported a genetically encoded method for *in situ* labeling of intracellular proteins.<sup>230</sup> Analogous to green fluorescent protein for fluorescence imaging, the genetically encoded tags provided a means for site-specific labeling of proteins of interest in mammalian cells with high-contrast elements, which enabled imaging of protein locations using STXM with 30 nm resolution (Figure 7). This ability to image multiple proteins holds promise for multimodal imaging to understand the biological effects and mechanisms of how NP-based drugs interact with cells at the molecular level.<sup>231</sup>

Overall, soft X-ray-based imaging methods make it possible to obtain morphological information from intact samples, quantitative mass information (*e.g.*, of the internalized NPs), and localization information about the different NP parts to study nano–bio interactions. Accompanied with advances on X-ray monochromator technology, optics, X-ray detectors, experiment control, and the quality of the X-ray light source, the diversity of imaging modalities based on synchrotron and X-ray free-electron lasers light sources are on the way toward achieving efficient imaging of cells. The combination of different modalities of X-ray microscopy to build multimodal instruments can succeed in achieving correlative imaging on the same cell, providing complementary information from each method.

In contrast to soft X-rays, the greater biological penetration depth of hard X-rays enables imaging of larger cells, tissues, and organisms. Furthermore, the morphology of tissues and cells can be visualized with hard X-rays through use of chemical staining to enhance the signal of organic structures of cells and tissue,<sup>232</sup> but also by using phase contrast data acquisition protocols,<sup>155–157</sup> including holotomography,<sup>233</sup> or coherent diffraction-based ptychography.<sup>234</sup> The morphology and organelle localization can also be assessed on cellular samples by using experimental approaches based on the correlative acquisition of optical and hard X-ray microscopy images.<sup>235</sup> Additionally, hard X-ray tomography can provide the high-resolution 3D distribution of metal NPs in cells,<sup>236,237</sup> as an important alternative to methodologies based on visible fluorescence and OCT.<sup>238</sup> Due to their pH independence, these methods also avoid the photobleaching considerations inherent to working with fluorophores. For example, in Figure 8, the 3D distribution of 20 nm Ag NPs inside a single human monocyte (THP-1) at different time points is shown, using hard X-ray TXM with Zernike phase contrast imaging at high spatial resolution of 60 nm at 8 keV.<sup>22</sup> These images directly demonstrate the cellular accumulation and exclusion processes of Ag NPs in THP-1 cells. The different content, 3D distribution, and aggregation states of the Ag NPs elucidated the time-dependent interactions of cells with the NPs. The Ag NPs were internalized by cells, trafficked from engulfed vesicles to the lysosomes, disrupted the lysosomal membranes, decreased matrix metalloproteinases, generated reactive oxygen species (ROS), and finally caused apoptosis of the cell.<sup>22</sup> While these findings could have been also determined with fluorescence imaging in the visible by using fluorescently labeled NPs, in this work, additional information was extracted that would not have been possible with fluorescence spectroscopy in the visible. The trick was to combine imaging with XANES, which also allows observing the oxidation states of Ag atoms.

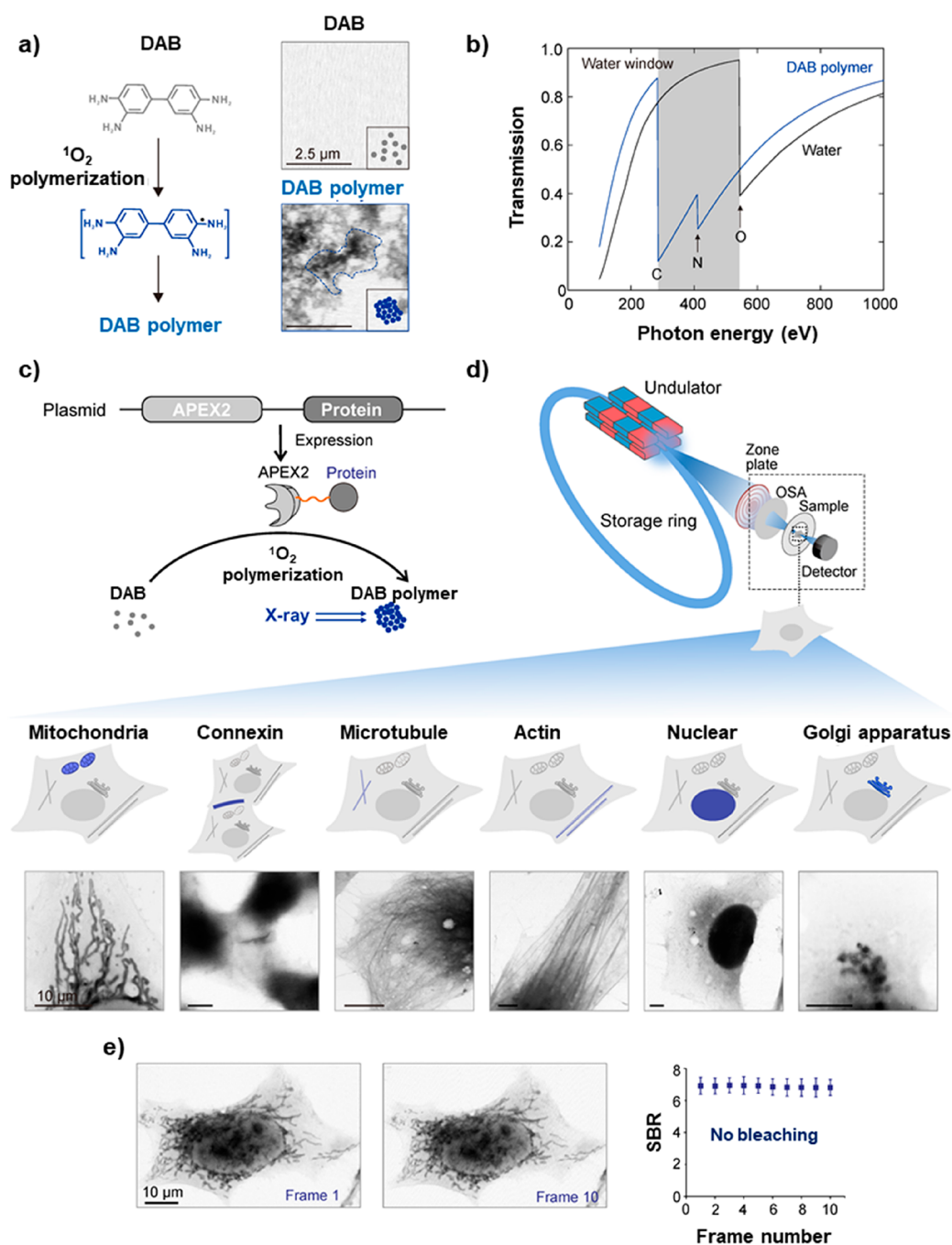


**Figure 7.** Repurpose engineered peroxidase as genetically encoded tags for protein localization with XRM. (a) Schematics showing the catalytic polymerization of 3,3'-diaminobenzidine (DAB) into DAB polymer (left) and X-ray imaging of DAB polymer (right). (b) X-ray absorption spectra of water and DAB polymer. In the "water window", absorption by carbon and nitrogen is much stronger than by oxygen. (c) Schematics showing APEX2 as a genetically encoded tag for protein localization with XRM. By using fusion expression plasmids including APEX2 and biotargets, these tags are highly specific and can polymerize DAB into localized X-ray-visible dense DAB polymers. This strategy enables localizing and imaging various cellular targets with high resolution. (d) STXM images of cellular proteins and specific amino acid sequences: COX4 (mitochondrial), Cx43,  $\alpha$ -tubulin,  $\beta$ -actin, NLS, and GalT. Scale bars: 10  $\mu\text{m}$ . (e) Photostability characterization of the genetically encoded tag for protein localization with XRM. No photobleaching occurred after 10 frames of STXM scans (for each STXM scan, the signal-to-background ratio of 10 loci was calculated and averaged to obtain a single value). Scale bars: 10  $\mu\text{m}$ . Reprinted with permission from ref 230 under a CC-BY License. Copyright 2020 Oxford University Press.

The cytotoxicity of Ag NPs is largely due to the chemical transformation from elemental Ag into particulate Ag, as  $(\text{Ag}^0)_n$  to  $\text{Ag}^+$  ions and  $\text{Ag}-\text{O}-$  and then  $\text{Ag}-\text{S}-$  species (see Figure 8a).<sup>22</sup> The same method has also been applied to visualize the distributions of  $\text{TiO}_2$  NPs and nano- $\text{MoS}_2$  in

cells.<sup>239,240</sup> Further possibilities of spectroscopic analyses are discussed in greater detail in a separate section, below.

Phase contrast approaches are more efficient than absorption-based techniques for imaging low-absorbing samples,<sup>233</sup> such as soft biological tissues without using staining procedures (and, therefore, promising for *in situ*

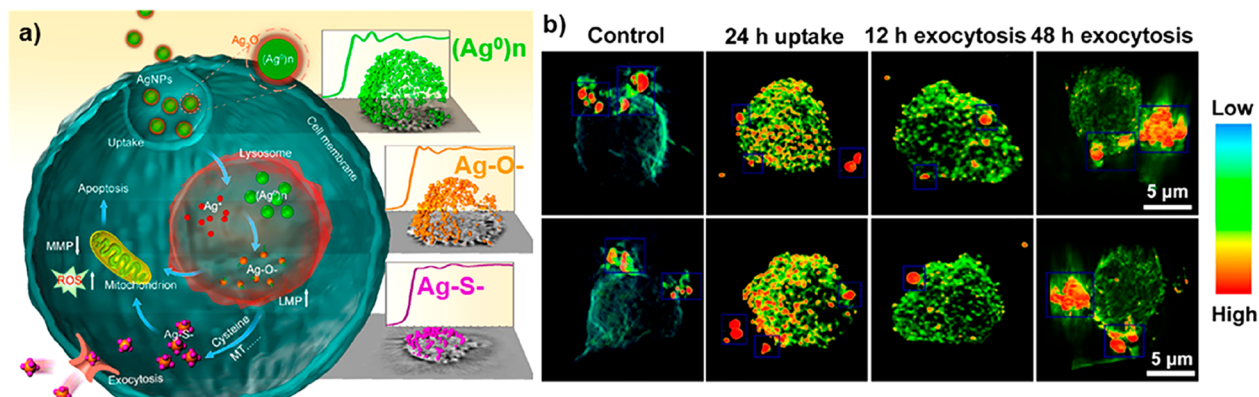


**Figure 8.** (a) Schematic diagram of the chemical mechanism of Ag NP toxicity to human monocytes (THP-1), showing also the XANES spectra of Ag atoms in different oxidation states/chemical environments. (b) Single-cell imaging with 3D hard X-ray tomography (NanoCT) to observe the spatial distribution of Ag NPs in a single THP-1 cell. Reprinted with permission from ref 22. Copyright (2015) American Chemical Society.

analysis). Phase contrast imaging follows alterations on the phase of X-rays as they go through an object. Such changes are related to the electron densities of the components of the sample, meaning the different cells or tissues in biological specimens. Imaging fine tissue structures or individual cells in hydrated samples is challenging, as differences in electron density between such biological structures and water are small (especially at the micro- or nanoscale). However, good contrast images with cellular or subcellular resolution can be obtained by using the correct experimental set-ups and phase retrieval algorithms. For example, full-field propagation-based phase contrast tomography has shown promising results for 3D imaging of weakly absorbing specimens such as biological samples with good resolution.<sup>241–244</sup> Apart from being applied to probe nanomaterials inside single cells, X-rays have already been used for imaging tissues or organisms. Current developments in benchtop X-ray sources make it possible to extend the same experimental approach (with submicrometer resolution) to clinical and biomedical research within a laboratory environment.<sup>243,245,246</sup> As such, the application of full-field propagation-based phase contrast tomography has enabled acquisition of a variety of data, from structural information on full or large sections of organs with  $\mu\text{m}$  resolution<sup>243,245–248</sup> to mapping in 3D the cellular organization of large areas of brains or lungs (from mice or human origin) with outstanding resolution<sup>241–244</sup> and collecting images from isolated cells with subcellular resolution.<sup>237,249,250</sup> Furthermore, as metal-based NP-based drugs would show much higher electron densities than the soft elements normally found in tissues or organs, it will be possible to detect them easily in biological samples using phase contrast techniques. Again, propagation-based phase contrast tomography has enabled scientists to discriminate individual barium-based NPs (used as contrast agents) and to map their locations within isolated macrophages.<sup>237</sup> It has also been used to determine the distributions of barium-labeled macrophages in lungs of healthy and asthmatic mice (showing preferential localization of macrophages within the alveoli and their ability to penetrate epithelial layers within lungs, Figure 9).<sup>241</sup> Interestingly, propagation-based phase contrast is highly dose efficient, and the size of the volume analyzed can be easily controlled by changing the relative distances between source, sample, and detector.<sup>241,243,246,251</sup> Yet, the analysis of larger volumes normally leads to images

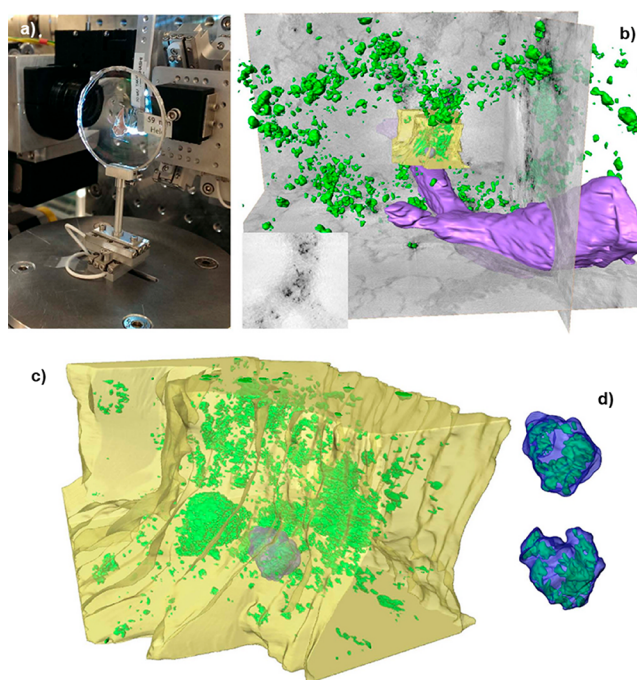


**Figure 9.** Example of propagation-based phase contrast tomography of a lung section from a healthy mouse where macrophages labeled with barium NPs were instilled, showing the barium NPs (green), blood vessel (purple), bronchial area (yellow), and the contours of macrophages (blue). (a) Lung section mounted on the sample holder. (b) 3D rendering of the reconstructed volume of a large field of view of the lung section. (c) 3D rendering of the reconstructed volume obtained from tomographic data zooming on the bronchial area in (b). (d) Detail of barium-labeled macrophage highlighted in (c) from two orientations showing the internal distribution of the NP. Reprinted with permission from ref 241 under a CC BY-NC-ND 4.0 International License. Copyright 2015 Nature Research.

with lower spatial resolution. Nevertheless, as the technique is nondestructive, it is possible to implement sequential analytical strategies. For example, images of full organs can be initially acquired to identify interesting areas, which can then be analyzed at higher resolution.<sup>241,243,246,251</sup> Thus, hard X-ray propagation phase contrast tomography is a promising approach to study NP-based drugs *in situ* at different levels

(i.e., from the cellular level to full organs or small animals) with a single technique. There is however concern that X-ray phase contrast imaging may suffer from increased required radiation doses.<sup>252</sup>

As shown in Figure 9, there is potential for *in situ* studies *in vivo*, at least in animals. Au NPs are attractive as CT contrast agent because of their strong X-ray attenuation, flexibility for surface functionalization, and biocompatibility. Wen *et al.*<sup>253</sup> studied kinetics of Gd-loaded dendrimer-entrapped Au NPs and monitored the accumulation of contrast in several organs over 45 min post-intravenous injection in rats using micro-CT. Zhang *et al.*<sup>254</sup> demonstrated an accumulation of a contrast agent in tumor tissue. They used a multimodal imaging nanoprobe by co-loading an aggregation-induced fluorescent dye (NPAPF) and Au NPs into FDA-approved micelles. The combination of fluorescence and micro-CT results in a probe with high sensitivity (fluorescence) and high spatial resolution (micro-CT). Of course, it does not yet overcome the limitation of restricted penetration depth of fluorescence imaging, but for small animal studies, this is not a crucial problem. Use of such a probe may be useful for testing strategies for enhanced sensitivity using synchrotron radiation. For translation to human imaging, the fluorescent marker could be replaced for example, by a SPECT label, as demonstrated in a study by Xu *et al.*<sup>255</sup> Their Au/<sup>99m</sup>Tc-PEG-RGD dendrimer entrapped NPs can be used as a nanoprobe for targeted SPECT/CT dual mode imaging of cancer cells *in vitro* and subcutaneous tumor models *in vivo*.

A form of CT imaging, known as spectral photon counting CT (SPCCT), has recently emerged as a tool for both preclinical and clinical studies.<sup>256</sup> Conventional CT uses energy-integrating detectors, whereas SPCCT uses photon-counting detectors. This approach allows characterization of the energy profile of the beam that has exited the subject as well as higher spatial resolution and lower radiation dose.<sup>257</sup> Of particular relevance to this Review, SPCCT allows “K-edge imaging” of elements ranging approximately from cerium to bismuth. K-edge imaging provides maps of elemental distributions within the subject and can image more than one element at a time.<sup>258,259</sup> This technique has been used with cerium, tantalum, ytterbium, gold, and bismuth NPs and for applications such as blood vessel imaging, targeted imaging, and cell tracking.<sup>260–263</sup> For example, Si-Mohamed *et al.* reported the use of SPCCT for tracking poly(ethylene glycol) (PEG)-coated Au NPs (Figure 10).<sup>264</sup> While conventional CT images suggested liver and spleen uptake, it was found by Au “K-edge” images that Au NPs were also in the bone marrow. Other applications of Au NPs for drug delivery, targeting, and imaging have been reviewed by Kong *et al.*<sup>265</sup>

*Ex vivo–in situ* studies can provide important information when linked to complementary studies *in vivo*. Study designs featuring multimodal longitudinal imaging *in vivo* with imaging methods permit good soft tissue contrast (e.g., MRI) and high sensitivity for monitoring drug kinetics (e.g., fluorescence or photoacoustics). These methods can be combined with synchrotron radiation-based detailed *ex vivo* assessment on intact animals or excised organs. Labels such as Au NPs are good candidates for this approach (not for MRI, which still provides the high-resolution anatomical background information). For drug-delivery systems, one needs to decide whether to label the carrier, the drug, or

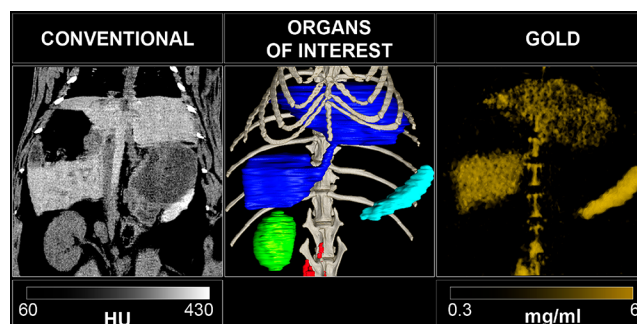


Figure 10. SPCCT images of a rabbit injected with PEG-coated, 15 nm core Au NPs, at 6 months post-injection. From left to right: A conventional CT image, segmentation of organs of interest (dark blue: liver, light blue: spleen, green: right kidney, red: lymph nodes, light gray: bone structure) and a Au “K-edge” image. Reprinted with permission from ref 264. Copyright 2017 Royal Society of Chemistry.

both. While drug labels may alter its efficacy, there are a few drugs that show intrinsic CT contrast, such as cisplatin and other metal-based drugs. Oxaliplatin is a second-generation platinum anticancer drug that has potent therapeutic effects against several gastrointestinal cancers, and platinum (but also other metals) can be imaged, albeit at this time point only *ex vivo*, with synchrotron-based XRF.<sup>266,267</sup> The latter was used to study drug distributions within tumor tissue. This *ex vivo* approach was subsequently also applied to human cancer tissue specimens. Higher platinum concentrations in the tumor stroma were an independent predictive factor of limited histologic response.<sup>268</sup> These results suggest that XRF analysis may contribute to *predicting* the therapeutic effect of I-OHP-based chemotherapy by quantifying the distribution of platinum. This result is an example of X-ray-based 3D histology that can complement standard histological approaches. XRF tomography was also used to determine the 3D accumulation of LaF<sub>3</sub>:Ce nanoscintillators in spheroid tumor models with micron resolution (Figure 11), helping to assess their capacity to act as radiotherapy agents against solid tumors.<sup>269</sup> In addition, XRF maps collected using nanofocused synchrotron radiation have enabled following not only the cellular internalization and degradation of labile Ag particles<sup>23,24</sup> and nanowires<sup>270</sup> but also other nanomaterials such as Au and Ti NPs<sup>236</sup> and Pt-based NP-drugs.<sup>271</sup> In fact, XRF permits multiplexed imaging of the distributions of different elements<sup>269,272</sup> (Figure 11) and provides lower limits of detection down to ultratrace elemental sensitivity for high-Z elements. In principle, the smallest units providing signal are individual atoms (in contrast to fluorescence in the visible/NIR, where the smallest unit providing signal are small molecules, i.e., fluorophores). Elemental mapping by XRF has been also coupled to XAS to determine the speciation of nanomaterials in tissue or cell samples.<sup>273</sup>

In addition, XRF can be used for imaging at scales *above* the cellular level. For example, synchrotron-based XFI has helped to study possible systemic toxicity caused by exposure to NPs found in pollution or consumer products by assessing *ex vivo* their accumulation in animal or plant tissues.<sup>152,274–277</sup> Furthermore, it was shown that XFI computed tomography permits detection of single cells in a Au-loaded tumor implanted in the head of an adult rat, thus demonstrating the suitability of this technique for *ex vivo*

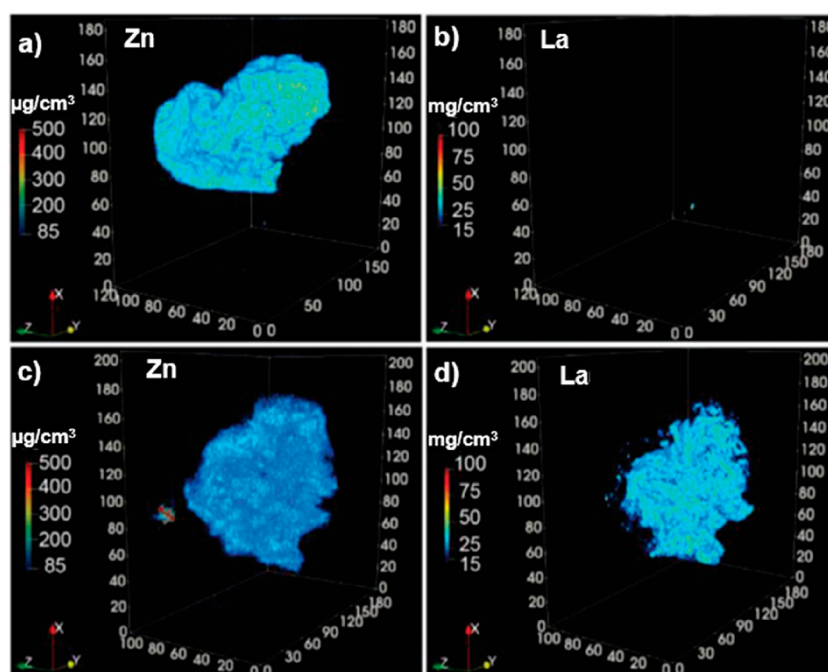


Figure 11. X-ray fluorescence 3D elemental maps showing the distributions of Zn and La in F98 spheroids (a,b) untreated or (c,d) treated with  $\text{LaF}_3\text{:Ce}$  NPs for anticancer radiotherapy. Axes are shown in  $\mu\text{m}$ . Adapted with permission from ref 269 under a CC-BY International License. Copyright 2020 Wiley-VCH GmbH.

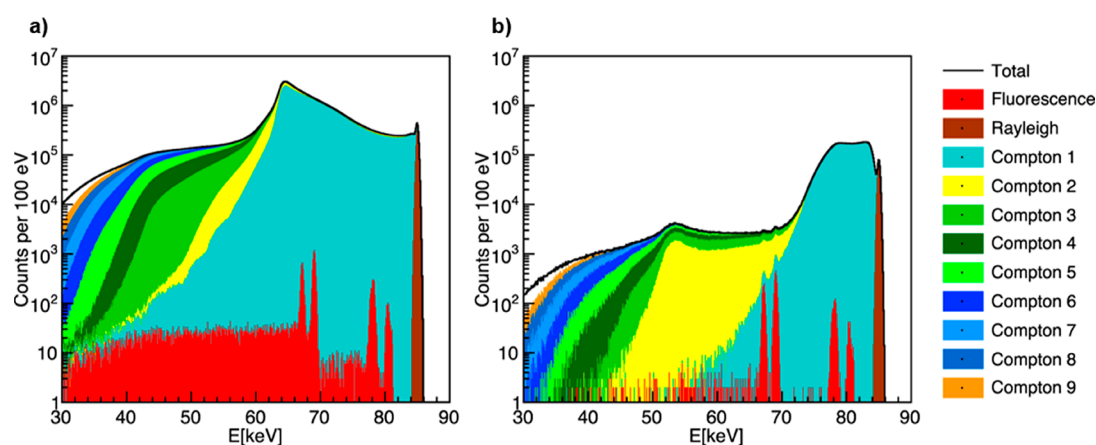


Figure 12. Simulated XFI spectra showing XFI signals obtained from a 30 cm-diameter water-filled sphere. (a) X-ray spectrum from the full solid angle ( $4\pi$ ) with X-ray fluorescence (red) Au NPs (peaks around 67 and 69 keV) are undetectable within a "sea of background photons" from multiple Compton scattering: of 1000 measured photons, only 1 is from fluorescence, the other 999 arise from Compton scattering (the color indicates how often a photon is Compton scattered). (b) Spectrum for the same situation, but after performing optimized "spatial filtering", which enables the detection of X-ray fluorescence signals from the Au NPs. Reprinted with permission from ref 57 under a CC BY-NC-ND 4.0 International License. Copyright 2018 Nature Research.

studies on brain-tumor cell migration.<sup>278</sup> Yet, for quite some time, XFI was seen as essentially unusable for objects of human size. This problem was overcome by a variant called "spatial filtering".<sup>57</sup> The broad background exhibited by XFI in the X-ray spectra of photons emerging from the irradiated object originate predominantly from multiple Compton scattering. For example, from about 1000 measured photons within the detector-resolved X-ray fluorescence lines' energy range, only 1 photon is a fluorescence photon, while the other 999 photons come from Compton scattering. In such a case, no XFI signal can be recorded. However, especially for larger objects, the XFI background can show strong anisotropy if the incident photon energy is close to and

just above the K-edge of the element excited.<sup>57</sup> With the help of a computer algorithm, only such pixels from a large-area pixelated detector are taken into account, yielding the highest information density in terms of XFI signal *versus* background noise. The subsets of selected pixels (hence "spatial filtering") show maximum imaging sensitivity, that is, statistical significance, respectively, whereas if all pixels are taken into account, the 1:999 ratio renders the signal unobservable (Figure 12). Thus, future clinical XFI applications are within reach, and this finding should trigger additional research starting with small-animal XFI. As a first example in this direction, *in situ* imaging of the natural iodine concentration in a mouse is shown in Figure 13. This XFI method,

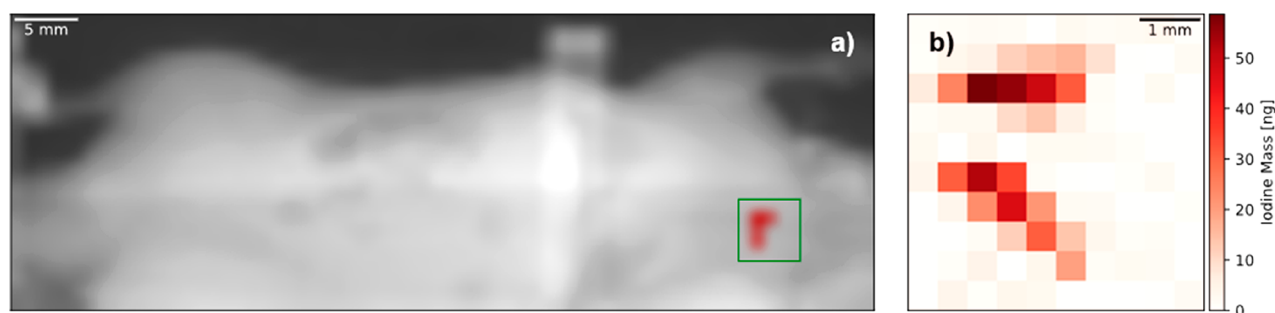


Figure 13. X-ray fluorescence imaging full-body (a) and fine scan of the thyroid region (b) of a mouse. The euthanized mouse was placed sideways with the X-ray beam impinging perpendicular to the figure plane (mouse head on the right side). The left map depicts the number of Compton-scattered photons for each scan position. As seen, the only visible iodine concentration is the natural one found in the thyroid with the local iodine mass in the beam volume as retrieved from data analysis (each pixel of the fine scan covers an area of  $0.25 \text{ mm}^2$  and shows the amount of iodine  $K_{\alpha}$  fluorescence photons). These data were recorded at Deutsches Elektronen-Synchrotron (DESY) by C. Körnig, O. Schmutzler, Y. Liu, T. Stauffer, A. Machicote, Beibei Liu, W. J. Parak, N. Feliu, S. Huber, F. Grüner and have not been published previously. Experiments involving animals were carried out in accordance with the Institutional Review Board “Behörde für Soziales, Familie, Gesundheit und Verbraucherschutz” (Hamburg, Germany).

however, depends on the use of pencil X-ray beams with monochromatic spectra, as provided at synchrotron-based beamlines. Although one can perform basic research at such facilities, translation into clinical application needs ultra-compact X-ray sources, such as laser-driven inverse Compton sources.<sup>279</sup>

Finally, to go from images to movies, time-lapse *in vivo* recordings are at the borderline of what is possible today with existing synchrotron technology. As biodistributions are dynamic and the effects of drugs are described by their pharmacokinetics, such capabilities are tantalizing and widely anticipated. Examples were reported in living cells using low-energy synchrotron-based Fourier-transformed infrared (FTIR) spectroscopy.<sup>280–284</sup> A successful transition to working in the X-ray regime will essentially need the development of methodologies to keep radiation damage at tolerable levels. However, this transition might be possible to achieve, and synchrotron-based hard X-ray phase contrast microtomography has been used to acquire time-lapse images of a living embryo.<sup>197,198</sup> Furthermore, the delivery of respiratory treatments in the lungs of mice has been recently studied *in vivo* by using time-lapse phase contrast imaging with hard X-rays produced by a compact synchrotron light source (CLS).<sup>285–287</sup>

### SCATTERING EXPERIMENTS FOR MONITORING THE TIME-DEPENDENT STRUCTURE/COMPOSITION OF NANOPARTICLES AND THEIR ASSEMBLIES

In this section, X-ray scattering techniques with applications in the characterization of NPs and NP-based drugs are highlighted. While some of these techniques have only been applied thus far to NP suspensions, their possible applications for studying intracellular NPs *etc.* are also discussed. In this direction, SAXS has been widely used and elucidates a wide range of properties. Before describing more complex systems, we give an overview of what SAXS can do in the analysis of NP properties. With regard to NP size distribution, SAXS can be applied to study NP formation and dissolution by making use of micro- and then nanofluidic devices.<sup>288,289</sup> For designing reproducible experiments that yield *in situ* time-resolved structural information at fast time scales, it is necessary to build X-ray compatible microfluidic devices. Polyimide/Kapton-only devices enable the *ex vivo* inves-

tigation of structural dynamics and phase transitions of a wide range of colloidal NPs and soft matter samples down to millisecond time scales. Such devices then can be used to follow structural evolution *in situ* at millisecond time scales using on-chip time-resolved SAXS under continuous-flow conditions. In combination with other techniques such as ultrafast Coulter counters,<sup>290</sup> this approach can have major impact on the design and formulation of amphiphilic polymer NPs for drug-delivery systems in medicine. More sophisticated reciprocal space mapping enables determining NP atomic-scale shape evolution *in situ* and *in operando* as a function of externally changing conditions.<sup>291–293</sup> Concerning shape changes, X-ray diffraction can be used to investigate NP degradation systematically in the form of oxidation or deactivation during catalytic reactions.<sup>294,295</sup> Imaging techniques such as CDI can provide detailed information on the shape and shape changes of single-metal NP in the size range of 100 nm diameter, as demonstrated previously in gas environments.<sup>296</sup> Ptychography can be used to follow changes in the size and shape of NPs in liquid phase, both *ex situ* and under *operando* conditions.<sup>183</sup> Similar responses of the NPs can be expected from other stimuli in the biological, wet chemical environment. Single PtRh alloy NPs and PdRh NP ensembles were found to dealloy by the formation of Rh oxide when switching from reducing to oxidizing conditions.<sup>297,298</sup> Such processes may also occur in cells electrochemically driven at room temperature when changes in pH take place. This change has potential relevance to biological applications, as surface-based catalysis is one origin of NP toxicity.<sup>299,300</sup> These technical possibilities also have potential for the development of applications concerning *in situ* observation of NP-based drugs. Simulations of *in situ* CDI data of the fusion of glioblastoma cells were already reported<sup>301</sup> and also considered radiation damage. Once CDI permits *in situ* imaging of NPs and NP-based drugs in biological environments, these experiments will provide important information about the states of the NP-based drugs such as changes in size and shape and also their effective size increases due to agglomeration. Dissolution of the NP carrier, for example, could be observed by reductions in size and also by changes in its shape. Time-resolved data may offer important information, as discussed below. Loss of the surface coating of the carrier NPs, involving, for example,

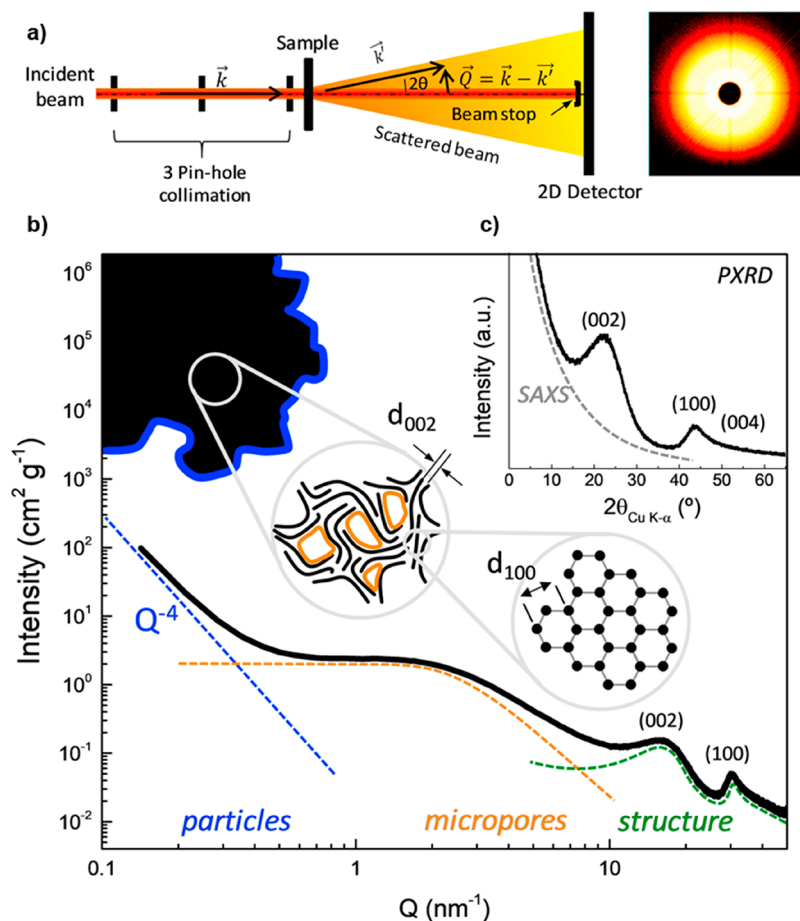


Figure 14. Example SAXS experiment to study the structure of a microporous nongraphitic carbon material. (a) Schematic showing the normal setup of a SAXS instrument. (b) Intensity versus scattering vector curve plot (log–log scale), highlighting morphological (low  $Q$  ranges), microstructural (intermediate  $Q$  ranges), and structural (large  $Q$  ranges) features of the material probed by the technique. (c) Intensity versus scattering angle  $2\theta$  plot (linear scale) of the same spectrum, which is normally used for PXRD. Reprinted with permission from ref 306 under a CC BY-NC-ND 4.0 International License. Copyright 2019 Elsevier.

attached pharmaceutical agents and ligands, might be detected by the onset of agglomeration. While such ideas (*i.e.*, to investigate the state of NPs in biological environments by measuring their effective hydrodynamic diameters) are also explored with other techniques,<sup>302</sup> a fundamental understanding of the interpretation remains lacking.

At the next level, SAXS is helpful in investigating NP assemblies. For “uncontrolled” assemblies, aggregated NPs give rise to diverging SAXS intensity in the direct beam direction, while distributed NPs show a plateau, which allows model-free extraction of the NP diameter. The exact length scale that can be probed by SAXS depends on X-ray collimation and X-ray wavelength. Conservative values for standard university lab sources using Mo X-ray radiation range from *ca.* 1 to *ca.* 50 nm.<sup>303</sup> The exact limits for a given sample depend on signal-to-noise ratio and the brilliance of the X-ray source. Synchrotrons can reach much more extreme values, that is, in ultrasmall-angle X-ray scattering, in which length scales of several microns have been probed in dental composites,<sup>304</sup> bridging the gap all the way to optical microscopy. An interesting recent development from the medical point of view is the use of high-energy X-rays of 50 keV and higher. In this regime, absorption due to the photoelectric effect is small. Since the Compton effect at higher X-ray energies affects mainly back scattering, there

should be little influence of Compton scattering on the SAXS pattern, as previously shown for X-ray reflectometry.<sup>305</sup> Thus, it seems possible to apply highly collimated high-energy X-ray beams for medical SAXS diagnosis of rather large tissue sections of 10 cm thickness (*i.e.*, full organ size). Nevertheless, this measurement would require developing methods capable of dealing with the low coherent scattering signals obtained from soft tissues at such high energies, which would be further attenuated by multiple scattering in thick samples.

Even more information can be obtained from “controlled” NP assemblies. Biomimetic NP assemblies can be conveniently investigated with synchrotron SAXS (Figure 14).<sup>306</sup> For instance, Xia *et al.* self-assembled self-limiting monodisperse supraparticles (SP) from polydisperse NPs.<sup>307</sup> For the majority of the NP assemblies forming spontaneously in bulk solution, self-organization occurs continuously until the components are exhausted and the NPs form a dry crystal, complex solid, or precipitate. A self-limiting self-assembly process would be conceptually different from currently known self-organization reactions. Because self-limiting structures are common in biological systems, the realization that using inorganic NPs might lead to unexpected parallels between the world of inorganic colloids and biomacromolecules. By conducting synchrotron SAXS, a distinct scattering pattern was observed and confirmed monodispersity in the large

ensemble of SPs in solution. The corresponding diameters and dispersibility of the SPs calculated from SAXS data matched the TEM, SEM, and dynamic light scattering (DLS) data. Together, they determine the sizes of SPs both in solution and in dry state and observed dense packing of the NPs. Data fitting using three different form factor models revealed a core–shell sphere as the most likely possibility. Fitting SAXS curves yielded the number of NPs in a single SP and the thickness of the shell, along with a loosely packed core and more densely packed outer shell. All these SAXS results give insight into the potential effects of different forces in self-limiting assembly.<sup>307</sup> Related work by Merkens *et al.* addressed formation of Au NP clusters within a microfluidic chip, driven by hydrophobic interactions.<sup>308</sup>

X-ray techniques are popular in investigating principles in biomimetic nanocomposites. In layer-by-layer (LbL) assembly, Podsiadlo *et al.* investigated the effects of combining polymers and NPs (clay nanosheets), both components with strong tendencies toward self-organization, into a single LbL assembly.<sup>309</sup> They found diffusional self-organization in exponential LbL films on the micro- and nanoscale. SAXS was employed to reveal the morphologies of the LbL films. In films that did not contain clay nanosheets, only diffuse scattering from the polymer was observed. Clay nanosheets spontaneously adsorb almost exclusively in orientations parallel to the substrate.<sup>310</sup> In the film containing clay, a sharp peak corresponding to basal spacing for Na<sup>+</sup>-montmorillonite was shown, and a less prominent peak to a larger basal spacing indicated significant intercalation of polymer between the clay sheets. No distinct peak was observed in another film with clay nanosheets, demonstrating intercalated basal spacing or exfoliation of clay platelets. All these results were helpful in determining the morphologies between the multilayers.<sup>309</sup> Another interesting case study was done by Zhang *et al.* in fabricating fibers with high toughness.<sup>311</sup> The materials architecture with alternating layers of hard inorganic components and soft organic polymers effectively arrests the propagation of cracks. Further improvement of toughness in biomimetic nanocomposites is restricted by the low strains of composite materials. The combination of two structural motifs at different scales (nanoscale and microscale) was designed to increase both the stretchability and toughness simultaneously. They transformed flat nacre films into fibers that combine layered nanoscale and spiral microscale structural motifs. Synchrotron SAXS was used to check the enhanced alignment. Since polymers scatter X-rays weakly, the diffraction peaks originated from the graphene nanosheets. The belt-like fibers without sharp scattering peaks indicated poor alignment of the nanosheets. The nearly perfect nacre-like layering in the transverse direction of the fiber yielded sharp peaks after initial twisting. Further twisted coiled fiber resulted in an absence of sharp peaks. All three fibers showed monotonic intensity drops, indicating the uniform dispersion of graphene in the poly(vinyl alcohol) (PVA) matrix.<sup>311</sup>

Chiral NPs or assemblies with intrinsic geometries that lack inversion symmetry, or with imprinted optical activity attributed to chiral ligands, have recently garnered significant attention for controlling biorecognition and optical sensing.<sup>312–314</sup> Chirality determines many structure–function relationships in nature at many levels of biological organization. Omnipresent chiral properties in biology inspire and necessitate further studies of chirality of nanoscale

materials due to many structural parallels between nano- and biomaterials as well as multiple biomedical applications of NPs. Typically, electronic circular dichroism (CD) in molecules ranging from individual amino acids to hierarchically more complex peptides, proteins, and oligonucleotides is analyzed using UV light, which is incompatible with living cells. However, chiral NP systems have been shown to exhibit significantly enhanced CD at optical and near-IR wavelengths, offering more sensitive and selective routes toward driving enantioselective intermolecular reactions,<sup>315</sup> facilitating higher NP–biomolecule affinities and tuning polarization-dependent light–matter interactions.<sup>316</sup> Indeed, the emergence of chirality in NPs increases their tendency to interact with specific biomolecules featuring similar chirality, a critical condition in drug discovery and delivery, and can also promote further remodeling of NPs by these species. While chiral discrimination can be applied with *in vitro* systems,<sup>317–319</sup> *in vivo* will be substantially more challenging, but engineered orders-of-magnitude enhancements in achievable optical electromagnetic density of chirality in plasmonic- and dielectric-based NP systems may enable discernible chiral hotspots to be detectable in imaging and spectroscopy.<sup>320,321</sup>

Experiments including synchrotron SAXS and XRD can be employed in many chiral nanostructure studies. For direct resolution using X-ray techniques, inversion asymmetric crystallinity of NPs or surface reconstruction with chiral ligands may show polarization-selective scattering, enabling tracking of enantioselective chiral drug delivery, NP toxicity, and protein corona formation.<sup>322,323</sup> In another study, Yan *et al.* self-assembled chiral NP pyramids with strong *R/S* optical activity.<sup>324</sup> They applied synchrotron SAXS combined with DLS data to give evidence for the actual space occupied by the NPs and their assemblies in “wet” states. This insight can help elucidate the degree of expansion upon hydration as well as the ensemble composition of the dispersions. By looking at SAXS features located at different scattering vectors, one can obtain information about different nanoscale superstructures in terms of size, shape, and conformation.<sup>324</sup> Jana *et al.* twisted stacking nanoplatelets to self-assemble into chiral ribbons.<sup>325</sup> All SAXS patterns of the dispersion at all three different steps of self-assembly displayed two scattering peaks whose position does not change over the whole process, confirming that the nanoplatelets remain stacked and the stacking period keeps constant.<sup>325</sup> Jiang *et al.* self-assembled hierarchically organized particles with greater complexity; SAXS served as a significant tool to substantiate the atomic structure of Au-Cys nanoribbons along with density functional theory calculations and XRD data.<sup>326</sup> Ahn *et al.* investigated the effects of chemical modification on the chirality of organic inorganic hybrid perovskites.<sup>327</sup> They used XRD to show the shift of a peak at the smallest  $2\theta$  angle (interlayer spacing of lead halide layers), ascribed to the phase transition of the crystalline structure due to the modulation of halide anion mixing ratio.<sup>327</sup>

As discussed above, such local scattering can be involved in X-ray imaging. Originally, X-ray-based scattering techniques were developed for bulk samples. However, by using low-emittance synchrotron sources with diffraction-limited storage rings, both from the current third-generation (*i.e.*, DESY or NSLS)<sup>328,329</sup> and increasingly from the fourth-generation instruments,<sup>330–333</sup> nanofocused beams providing increased photon flux and coherence are possible, and thus scattering

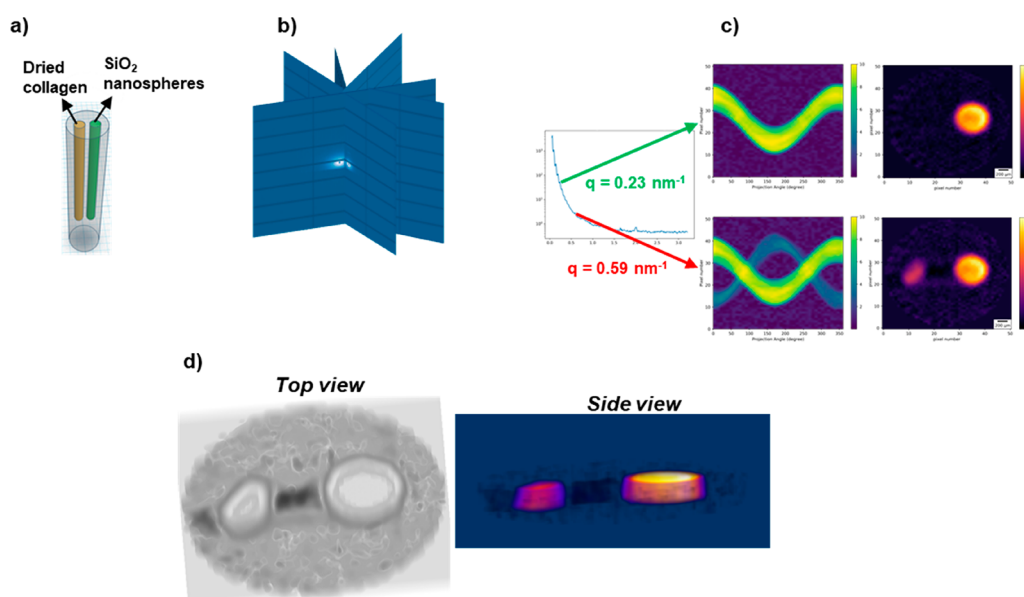


**Figure 15.** (a) Phantom for SAXS tomography: Dried collagen (anisotropic scattering) and 120 nm SiO<sub>2</sub> nanospheres (isotropic scattering) inserted in a homogeneous matrix of RW3 solid water (PTW Freiburg, Freiburg, Germany), which simulates water. (b) Tomographic data set for pencil-beam geometry. (c) Depending on the  $q$ -value choice, some structure is highlighted. In this case, reconstructing at  $q = 0.23 \text{ nm}^{-1}$  emphasizes the SiO<sub>2</sub> nanospheres, while if the signal from collagen is desired, the reconstruction is carried out at the  $q = 0.59 \text{ nm}^{-1}$ . (d) 3D view of the SAXS-CT phantom from the top and the side. These data were recorded at the beamline BL40B2 at the Spring-8 synchrotron source for this work by Andre L. C. Conceição and have not been published previously.

can be carried out locally with high spatial resolution, enabling improved imaging modalities.

SAXS is particularly useful for studying nanoscale morphology in complex environments.<sup>334</sup> Examples range from plant and bone structures up to brain and breast tumors and cardiac tissue.<sup>335–338</sup> By combining scanning approaches along the  $x$ - $y$  plane, rotation around the tomographic axis ( $y$ ), and tilting around the  $x$  axis, SAXS serves as a tomography technique.<sup>339–342</sup> SAXS-computed tomography (SAXS-CT) bridges the gap between information retrieved from high-resolution local techniques and information from low-resolution, large field-of-view imaging techniques when some hierarchical structure is present. Figure 15 shows the schematic procedure for SAXS-CT from the data acquisition to the volume-resolved architectural nanostructure, passing by the choice of the  $q$ -value for reconstruction. Detection of NPs in soft tissues by SAXS is efficient if the electron density of embedded NPs is higher than the hydrocarbon matrix, that is, oxide, semiconductor, or metal NPs are easy to detect in soft tissue matrices. Information that can be readily extracted from such measurements includes the NP size distributions, NP shapes, pair distances between interacting NPs due to molecular interactions,<sup>343,344</sup> and aggregation states.<sup>345</sup> These structural parameters can also be spatially resolved by applying the reverse analysis approach to the SAXS tomograms.<sup>342</sup>

A number of X-ray diffraction or scattering techniques can also generate cell images capable of showing the structure of different organelles with high resolution. Such imaging techniques have been extensively discussed in a recent review.<sup>154</sup> Combinations between those and other X-ray imaging techniques can help probing NPs in cells. In particular, correlative imaging of chemically fixed HeLa cancer cells by fluorescence (optical) microscopy, diffraction-based ptychography, and STXM using X-rays tuned to

the Fe L-edge were effective in determining the specific cellular localization of individual Fe NPs, showing that particles were internalized by cells in <30 min.<sup>189</sup>

It should also be possible to observe the interactions of NPs with cellular membranes directly. X-ray reflectivity (XRR) can be utilized to analyze the adsorption behavior and conformational arrangements of proteins on biomaterials surfaces.<sup>346</sup> XRR furthermore permits the characterization of the lipid-induced fibrillation at the molecular level.<sup>347</sup> The assembly of ligands on NP surfaces can be tested in comparatively simple experiments on planar surfaces using XRR. The XRR technique enables us to probe the attachment and penetration of NP-based drugs through model cell membranes containing lipids and proteins and, in turn, may aid our understanding regarding various physiological functions such as cellular transport, signaling, membrane trafficking, and molecular recognition. For these studies, a Langmuir monolayer of lipids is formed on the water surface, and high-energy synchrotron X-rays are used for XRR and related measurements to cover a larger momentum-transfer ( $q$ ) space (Figure 16).<sup>348</sup> Apart from measurements on the liquid surface, one can also collect XRR data from solid surfaces immersed in liquid using high-energy X-rays. This method becomes particularly helpful as X-rays, which can penetrate through the thick water bath over the membrane.<sup>349</sup> The electron density profile (EDP) obtained from XRR measurements and pressure molecular area data of Langmuir monolayers over water surfaces have demonstrated membrane localization of heme.<sup>348</sup> Heme and its analog hemin, are among the most biologically relevant planar organic molecules. Therefore, it is important to understand the molecular mechanism of intercalation and adsorption of this cytotoxic molecule after its dissociation from proteins such as hemoglobin. Continuous hemin uptake from the subphase and intercalation into and/or adsorption on to the

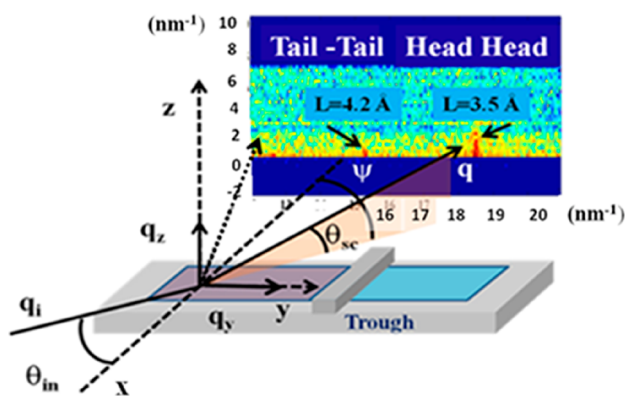


Figure 16. Typical arrangement for X-ray reflectivity and related measurements in a synchrotron experiment. Reprinted with permission from ref 351. Copyright 2019 American Chemical Society.

membrane surface have been witnessed in a strong membrane surface packing-specific manner. Competitive interactions between hemin–membrane and hemin–hemin are proposed to be responsible for the critical hemin concentration. Systematic studies of the EDP showed that up to the limit, continuous hemin uptake is possible and beyond that the hemin–hemin interactions dominate, effectively reducing the hemin intercalation into the membrane. The technique developed could be easily adopted for NP-based drugs by putting them in the subphase to study uptake and orientation-specific attachment in the Langmuir monolayer of bioengineered membranes. Two lipids, namely 1,2-dimyristoyl-*sn*-glycero-3-phosphocholine and 1,2-dimyristoyl-*sn*-glycero-3-phosphoethanolamine, with differences only in their head groups, were studied to understand the specificity of a model protein spectrin for zwitterionic lipids,<sup>349</sup> which constitute the major part of the physiological membrane. Spectrin is a high-molecular-weight, *ca.* 100 nm-long, flexible rod-like protein composed of two subunits. Similar measurements could be carried out to model NP-based drug attachment and penetration of appropriately engineered biomembranes. X-ray reflectivity is a powerful non-invasive technique to determine the buried structure of thin films along the depth,<sup>350</sup> and the extracted EDP from the reflectivity analysis showed that spectrin chains form a uniform layer on top of the phosphocholine-containing bilayer, whereas spectrin gets adsorbed into the phosphoethanolamine-containing membrane, possibly through one or two permanent binding sites with the rest of the chains projected out of the membrane.

### SPECTROSCOPIES TO INVESTIGATE BIOTRANSFORMATION OF NANOPARTICLES IN BIOLOGICAL ENVIRONMENT

Spectroscopies also provide information regarding the chemical states of NPs. Exposure of nanomaterials to biological fluids can affect the surface properties of NPs. Such effects often occur at the outer surface (*e.g.*, loss or rearrangement of capping ligands) and may affect solubility, aggregation, and interactions with their environment. These effects can also happen at the cores of the NPs (*e.g.*, dissolution, remodeling). These changes are especially significant for small NPs having size- and shape-dependent properties, since dissolution of even a few outer layers of the

NP core and modifications to the faceting or shapes of plasmonic NPs can dramatically alter their behavior. *Ex situ* XRD and TEM can provide information about changes to the NP cores that are permanent and therefore do not revert back to their original state. Since NPs are rarely employed in their pristine forms, dynamic exchange of corona proteins,<sup>352</sup> or the ligands that serve in a protection role with the surrounding medium, is expected for almost all types of NPs. Continuous interplay with biomolecules in biological environments gives NPs different bioidentities.<sup>352</sup> Some biomolecules also induce variations in surface properties (charge, hydrophobicity, *etc.*), roughness, and local chemical environment of NPs, cause dissolution/degradation, and ion leaching of NPs, subsequently generating ROS and oxidative stress, which eventually can cause toxicity to cells.<sup>353,354</sup> To reveal such processes, imaging surface plasmon resonance (ISPR) is frequently leveraged,<sup>355,356</sup> in which the loss of previous ligands indirectly causes shifts in the optical resonance peaks of the NPs through remodeling the local refractive index. Kinetics of ligand exchange or loss can further be derived from time-dependent ISPR profiles to give insight into the interplay of coated NPs with the surrounding biological fluids.<sup>357</sup> Under dark-field illumination, ISPR has a resolution down to the level of an individual NP.<sup>358</sup> Major limitations of ISPR characterization include the inability to reflect the kinetics of multiple ligand loss and dynamic processes, as witnessed during the establishment of the soft protein corona. In the presence of persistent ligand loss, there stands a chance for the NP itself to be influenced, in which the remodeling of surface roughness is likely to be observed. Under such conditions, under-coordinated atoms (referred to as adatoms) are more prone to oxidation or atom-exchange with respect to their fully coordinated counterparts.<sup>359</sup> The dynamic processes of surface roughness variation can be visualized by using *in situ* liquid-TEM imaging. An updated modality of a gas-supplement equipment might even enable this system to image living cells at nanometer resolution.<sup>360</sup> Beyond projections, reconstruction of the whole NP through tomographic TEM (3D TEM) permits the view from varying directions to reach unbiased conclusions.<sup>361</sup>

The interactions between X-rays and matter are determined by the elemental composition of the matter and the energies of the photons. Hard X-ray spectroscopy involves promoting a core electron of an atom to unoccupied levels by absorption of the incident X-ray photon, followed by emission of a lower energy photon during electron decay to fill the hole. Both XANES (also called NEXAFS at energies below 1 keV) and EXAFS can provide quantitative information about chemical bonding, the oxidation state of the absorbing atom, the local atomic environment such as coordination number, type, and length of the metal–ligand bond, independent of the state of aggregation (NPs, ions, clusters).<sup>153</sup> Thus, they are not only used to study the molecular reactions preceding the nucleation of colloidal NPs but also can be applied to investigate NP assembly and NP uptake by cells and related toxicity.

Supramolecular assemblies have been characterized using XANES. For example, Kenji *et al.* were inspired by coordination assemblies of organic building blocks, which occurred in many biotic systems, and these systems attained exemplary performance in redox and photonic reactions optimized for the cellular environment.<sup>362</sup> Synchrotron EXAFS was used to help establish the coordination pattern

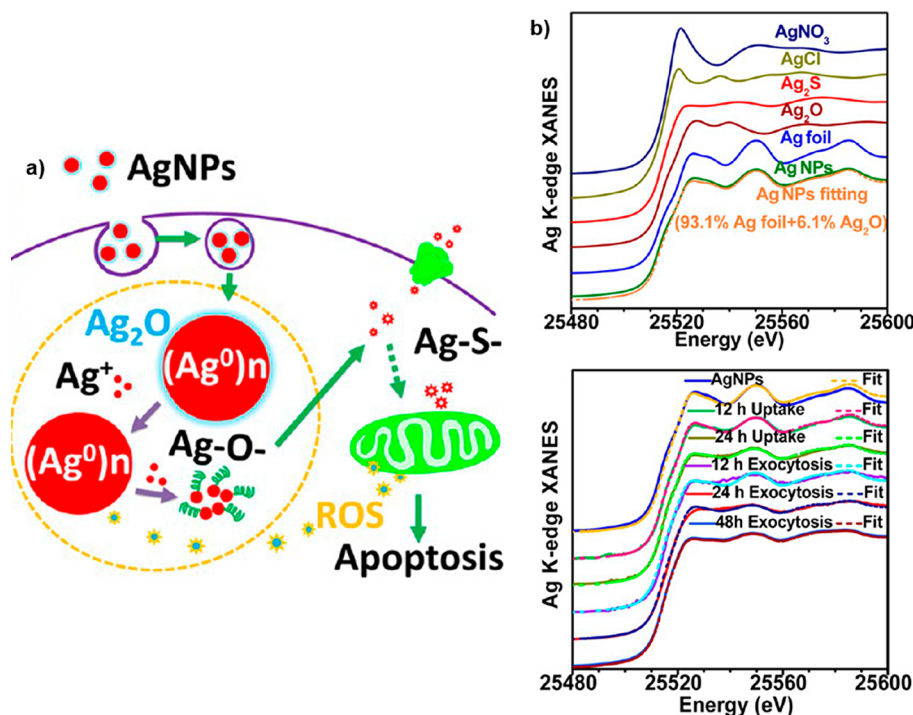


Figure 17. (a) Schematic illustration of the mechanism of toxicity of Ag NPs. Adapted from ref 22. Copyright 2015 American Chemical Society. (b) Different chemical species of Ag as indicated in normalized Ag L<sub>3</sub>-edge XANES. Reprinted with permission from ref 22.

of Zn<sup>2+</sup> and the supramolecular geometry of the interparticle bridges. Fourier-transformed XAFS plots of Zn<sup>2+</sup> in the nanoscale sheets were found to be nearly identical to that of [Zn<sub>4</sub>(μ<sub>4</sub>-O)]<sup>6+</sup>SP clusters in zinc stearate, indicating that the coordination clusters in nanosheets have the same coordination geometry with Zn<sup>2+</sup> stearate. These results, along with additional complementary experimental data sets (XRD, EDX, *etc.*), demonstrate that the assembly was driven by coordination bonds rather than other intermolecular forces.<sup>362</sup>

Nanoparticles can be related to their catalytic properties, such as in the case of metal NPs.<sup>363,364</sup> Metal clusters and metal complexes show a number of chemical and catalytic activities that can be explored by a combination of optical and X-ray spectroscopies. Examples are entatic state model complexes showing catalytic activity due to charge and electron transfer between the metal center and its ligand sphere. Studies involve the activation of catalytic activity by optically exciting metal complexes and probing them by means of EXAFS and XANES, raising the possibility of studying photoactivated complexes *in operando*.<sup>188,365</sup> The photocatalytic activity of Cu-based metal clusters has been studied through such combinations of optical and X-ray spectroscopies.<sup>366</sup> These studies involved the activation of catalytic activity by optically exciting metal complexes and probing them by means of EXAFS and XANES. The XAS showed shifts in the XANES edges due to changes in the metal oxidation state, while EXAFS tracked local changes of the structural environment surrounding the metal site. The complementary use of optical and X-ray techniques enabled the study of a wide range of different time scales.<sup>188</sup> Such studies could also be carried out in cells. For example, the genotoxicity of Ag NPs has been investigated by testing the DNA and chromosomal damage to CHO-K1 cells according to Organization for Economic Cooperation and Development

guidelines, and a ROS and Ag<sup>+</sup>-releasing mechanism was proposed (Figure 17a).<sup>367</sup> Further, as discussed above in a different context, Chen *et al.* (and others) reported the intracellular stability and chemical state of Ag NPs with the help of XANES spectroscopy (Figure 17b), together with a degradation study, proved the quick dissolution of Ag NPs inside cells and that the released Ag<sup>+</sup> was oxidized to Ag-O<sup>-</sup> species, subsequently stabilized by thiol groups, forming Ag-S bonds within the cells. The degradation of Ag NPs inside cells increased ROS production, decreased cell viability, and decreased the ultimate toxicity to cells.<sup>20,23,24</sup> This ion-releasing and redox-related mechanism of toxicity has also been found in ZnO<sub>2</sub>, CeO<sub>2</sub>, and other metal oxide NPs.<sup>368,369</sup> Thus, XANES spectroscopy is a powerful method to study the oxidation states of NPs inside cells, ion release, and surface redox and oxidative stress-related mechanisms of toxicities. This information can aid the safe design of NPs by inhibiting the dissolution of metal ions of NPs or to modulate oxidative stress.<sup>370–372</sup>

In another example, Gong *et al.*<sup>373</sup> applied XANES and EXAFS to investigate the behavior of dispersed Au atoms in distinct carbon-dot-supported Au NPs. They found that dispersed Au atoms in NPs, compared with small Au clusters, enable to react efficiently with glutathione (GSH) to form Au-S bonds and to reduce the GSH levels in cells. Taking advantage of XANES and EXAFS, researchers observed the dispersion of Au<sup>0</sup> as a peak at ~2.5 Å and confirmed that the GSH depletion is due to the atomic-level dispersed Au, which highlights the potential of atomic economy in NP design. Thus, by deciphering the chemical mechanism of NP-bio interactions, X-ray-based spectroscopy could provide insights into cellular regulation with NPs.

Today's questions in NP research and particularly in toxicity in human tissue go far beyond studying oxidation state. In this context, studying the electronic structure of the

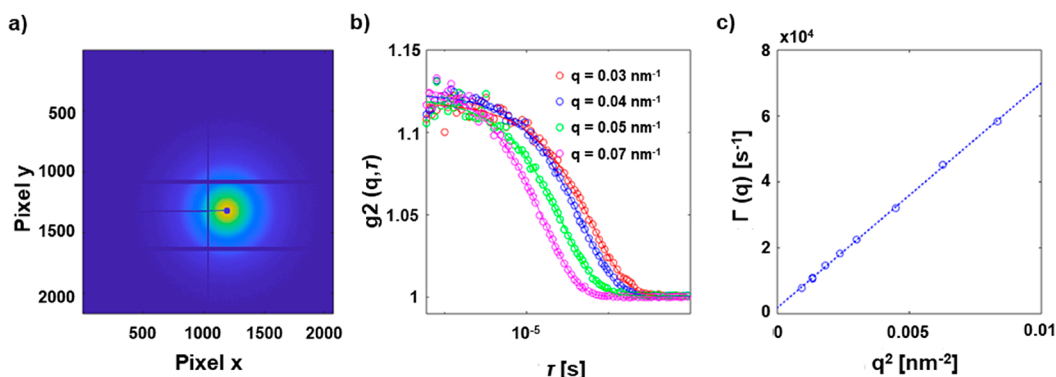


Figure 18. (a) SAXS pattern of an aqueous dispersion of 50 nm-diameter Au NPs. (b) Autocorrelation functions  $g(q, \tau)$  for different scattering vectors  $q$ . The autocorrelation function was fitted by a diffusion model  $g(q, \tau) \propto \exp(-2 \times \Gamma(q))$  with  $\Gamma(q) = D(q) \times q^2 + c$ . The diffusion coefficient  $D$  was fitted from the  $\Gamma(q)$  data, leading with the Stokes–Einstein equation (assuming 22 °C and using the viscosity of water) to an effective hydrodynamic diameter of 66 nm. These data were recorded at Deutsches Elektronen-Synchrotron (DESY) for this work by X. Sun, F. Otto, C. Sanchez-Cano, N. Feliu, F. Westermeier, and W. J. Parak and have not been published previously.

central metal atom (M) and differentiating between various metal ligands (e.g., carbon, nitrogen, oxygen) during NP uptake is important. However, conventional hard X-ray spectroscopy is not able to distinguish between M–C, M–N, and M–O ligands. This limitation could be circumvented by the recent implementation of high-energy resolution spectrometers, which provide a superb opportunity to access the types, protonation states, and ionization energies of ligands bound to metals.<sup>374–376</sup> Moreover, with the same experimental setup, high-energy-resolution fluorescence detected-XANES and X-ray emission spectroscopy (XES) can provide complementary information about the highest occupied and lowest unoccupied electronic states. Thus far, the method was successfully applied to shed light on weak noncovalent bonding of CO<sub>2</sub> to NPs, the roles of a central carbon in the nitrogenase iron–molybdenum cofactor, and photocatalysis.<sup>377–379</sup> Furthermore, the implementation of high-energy-resolution spectrometers facilitates measurements of hard X-ray magnetic circular dichroism combined with resonant inelastic X-ray scattering (RIXS-MCD) on magnetic NPs relevant in biomedical applications as contrast agents. The RIXS-MCD method enables the determination of the size distributions of superparamagnetic iron oxide NPs in frozen samples and in concentrated solutions, which are below the detection limits of light-scattering probes.<sup>380–382</sup>

An alternative method to monitoring oxidation and spin-state changes is XES, which spectrally disperses the X-ray fluorescence beyond elemental sensitivity and records spectral emission line-shapes of  $K_{\alpha}$  and  $K_{\beta}$  emission. These shapes are characteristic of the oxidation and spin states and of the chemical environment of the NPs.<sup>383–386</sup> The high resolution of XES enables elemental determination, and XES greatly benefits from not requiring monochromatic X-ray radiation, as needed for XANES spectroscopy (the latter typically operating at bandwidths,  $\Delta E$ , relative to the photon energy,  $E$ , of  $\Delta E/E \approx 10^{-4}$ ), thereby exploiting the full flux of many X-ray sources, such as undulators at synchrotron radiation facilities. Indeed, XES is particularly well suited for heavier elements in solution and cellular phases because the total fluorescence yield greatly increases from  $\sim 1\%$  for light elements (C, N, O, etc.) versus  $\sim 30\%$  for 3d transition metals (Mn, Fe, Co, etc.) to  $>80\%$  for 4d and 5d transition metals.<sup>387</sup> Spectral filters can further reduce fluorescent

background from organic matter. X-ray emission is widely used in analytical techniques such as proton-induced X-ray emission<sup>388</sup> and is often combined with monochromatic X-ray sources to study NPs with resonant RIXS, statically and dynamically.<sup>383–386</sup> With advances in relatively simple high-resolution spectrometers and fast line and area detectors, pink-beam sources can provide a high chemical specificity if required or increased flux at lower spectral resolution, providing sufficient elemental sensitivity to distinguish heavier elements in NPs from organic matter. The development of microcalorimeter pixel arrays with high spectral resolution is relatively recent in the field of X-ray spectroscopy and has great potential for combining X-ray emission spectroscopy, multiplexed recording, and even imaging.

Finally, classical X-ray-based spectroscopies, such as XPS, provide information about the surfaces of NPs. XPS has been used to probe the degradation of labile and stable NPs (Ag and Pt, respectively), once internalized by cancer cells.<sup>389</sup> The results showed that in 48 h, only 30% of the stable Pt internalized was oxidized (to Pt<sup>II</sup> or Pt<sup>IV</sup>), while all of the labile Ag NPs were degraded in the same time (forming inside cells nanoclusters, AgO, AgS, or AgCl species).

In parallel to the advantages outlined in the previous section on scattering techniques, through the use of synchrotron sources (especially from the fourth generation),<sup>330–333</sup> X-ray spectroscopy can be carried out locally with high spatial resolution, giving way to improved imaging modalities.

## METHODS FOR OBSERVING THE COLLOIDAL PROPERTIES OF NANOPARTICLES IN BIOLOGICAL ENVIRONMENTS

When coherent X-rays are scattered from disordered samples, such as an assembly of NPs or proteins, the photons scattered by the individual objects interfere and give rise to characteristic modulation of the scattered intensities. These patterns, usually referred to as speckle patterns, contain information about the exact spatial arrangement of the individual sample objects. Movements of the sample lead to corresponding changes of the scattering pattern. These changes can be quantified by calculating the time intensity autocorrelation function  $g(q, \tau) = \langle I(q, t) \times I(q, t + \tau) \rangle / \langle I(q) \rangle^2$  for a given point of the scattering pattern, a technique known

as XPCS,<sup>158,390</sup> the X-ray analogue of DLS. As an ensemble-averaging technique, XPCS allows for measuring the dynamics of all objects scattering at a particular length scale. In the simplest case of unhindered Brownian motion of a colloidal NP, the hydrodynamic diameter can be directly obtained, which changes depending on the state and surrounding medium of the colloidal NPs,<sup>161</sup> as shown in Figure 18. It thus offers the possibility of monitoring colloidal stability or the size of a shell of adsorbed proteins, which slows down the free diffusion of a single NP. Moreover, XPCS gives access to dynamics that are directly associated with a certain length scale in a sample by the momentum transfer wave vector  $q$ . In the case of NP internalization by endocytosis/phagocytosis, hindered NP movement can be observed by  $q$ - and thus length-scale-dependent measurements.

The advent of fast 2D X-ray detectors with framing rates in the milli- and even microsecond time ranges offers the possibility of observing direction-dependent dynamics by XPCS,<sup>391,392</sup> which is beneficial in flowing systems or in directionally ordered structures as can be ubiquitously found in biological specimens, starting from individual cell organelles like the Golgi apparatus, individual cells like myocytes, up to complete organs like the heart. Changes in the dynamics, due, for example, to colloidal disintegration or the adsorption of proteins, can be tracked by calculating the two-time intensity correlation function  $g(q, t_1, t_2)$ , which gives access to nonstationary dynamics and thereby enables following the temporal evolution of sample systems.<sup>393</sup> One major challenge of most X-ray-based techniques, and in particular XPCS experiments, when applied to biological samples systems, is beam damage (see below for details about this topic). One possibility for minimizing damage is to employ XPCS based on speckle visibility, where the degradation of a speckle pattern is observed as a function of illumination time. As each measurement can be performed on a fresh sample spot, this greatly reduces the dose to the sample.<sup>394,395</sup> In principle, measurements in this direction could offer *in situ* monitoring of NP degradation (which would lead to reduced diameters) or changes in surface chemistry, which would change the state of agglomeration and thus alter the effective hydrodynamic diameter. In particular, colloidal stability of NP-based drugs in biological environment containing salt and large amounts of proteins (e.g., in blood) could be monitored.

Until now, XPCS has been used primarily to study the dynamics of colloidal glasses, gels, and polymers.<sup>396</sup> In analogy to such systems, biological soft matter exhibits complex dynamics over many time and length scales, including nondiffusive, anisotropic, and spatially and temporally heterogeneous dynamics.<sup>397</sup> Studying and understanding these dynamics, ranging from localized fast rattling-like motions of, for example, spatially confined NPs to slow network dynamics, could help to assign characteristic dynamic “signatures” to different cellular compartments and binding states. Beyond the state of the NP and its ligand shell in response to the complex environment mentioned above, analyses on the ensemble level are possible that quantify and characterize the fraction of localized NPs, as has been shown for gel-forming Au NP suspensions.<sup>398</sup> Although the underlying questions in studying colloidal glasses and gels *versus* biological soft matter are quite different, the capability of XPCS to develop a complex microscopic picture of the

system under study offers exciting possibilities. The increasing quality of photon sources, in particular with the advent of the fourth generation of synchrotron sources, in terms of coherent flux and coherence lengths helps to improve the signal-to-noise ratios, thus allowing XPCS studies of weakly scattering samples, as demonstrated recently for concentrated lysozyme solutions.<sup>399</sup> Modern free-electron lasers (FELs) have superior coherence properties and high-repetition rates that result in outstanding temporal resolution.<sup>399</sup> However, the high brilliance and ultrashort pulse lengths lead to radiation damage being a severe problem beyond single-shot studies. Nevertheless, FEL-XPCS studies of radiation-sensitive samples have been demonstrated and are therefore also conceivable for biological systems.<sup>400</sup>

First steps using related techniques have already been applied for monitoring the release of drugs from carrier NPs. In recent years it has been realized that the cellular distribution and delivery of NPs to cells under *in vitro* and *in vivo* conditions can be very different, primarily due to shear stresses generated by the fluid flow inside the body.<sup>401–405</sup> The shear stress generated by the blood flow through a healthy artery is  $\sim 1$  Pa. As the stress generated is inversely proportional to  $r^3$  ( $r$  being radius of the vessel), the shear stress is enhanced by almost 1 order of magnitude ( $\sim 10$ – $20$  Pa) in stenosed vessels. The fluid shear stress contributes to regulating specific cellular processes and determines the efficacy of intracellular drug delivery. The interactions of NPs with cells depend on NP composition, charge, concentration, and shape as well as on the types of cells. In general, cationic NPs interact more strongly with cells due to negatively charged groups on the cell membrane<sup>406</sup> (although this may not be true for bigger particles),<sup>238</sup> and shear stress can further stimulate this interaction. The shear stress can affect ligand–receptor adhesion for NPs to cells, resulting in altered cellular uptake of the NPs and hence varied drug delivery. In recent years, mechano-sensitive drug delivery systems have been demonstrated where payload is released under enhanced stress. It has been suggested that shear-based drug delivery can be more powerful than biological and chemical methods, especially in conditions such as atherosclerosis where disease-specific markers are not well identified. Two routes have been demonstrated: (i) Shear-activated nanotherapeutics, where supraparticulate NPs (of the size of natural platelets) are composites of smaller NPs (with drugs), which are stable under normal blood flow, but break into individual NPs under high local shear stress in an obstructed region, thus delivering the drug or drugs.<sup>405</sup> (ii) Vesicles loaded with drugs change their shape from spherical to lenticular shapes at elevated shear stresses in semiclogged portions, thus releasing drugs either due to pore formation or disruption of the vesicles (Figure 19).<sup>402</sup> The exact mechanism can vary with the nature of the instabilities of the vesicles under shear stress. This discussion highlights the importance of fluidic shear stress both in tuning the cell-NP interaction as well as in targeted drug delivery. X-ray-based techniques like SAXS, XPCS, and X-ray fluorescence correlation spectroscopy in microfluidic devices, which emulate *in vivo* environments by mimicking fluid flow conditions of the body (including flexible channels and pulsating flows), will provide real-time structure and dynamics information on the interaction of the NPs carrying drugs to cells. Another exciting possibility is to use *in situ* grazing incidence X-ray diffraction from a monolayer consisting of NPs and cells at the air–water

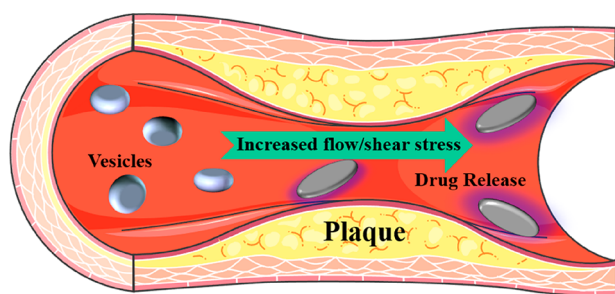


**Figure 19.** Schematic of shear-stress-induced drug delivery using shape changes of the drug-loaded vesicles. Cartoon created using images modified from Servier Medical Art (Servier, [www.servier.com](http://www.servier.com)), under a CC-BY 3.0 International License.

interface undergoing shear in an interfacial rheology setup. An experiment of this type has recently been demonstrated, wherein changes in the lipid–protein monolayers were quantitatively studied as a function of shear stress.<sup>407</sup>

### CHALLENGES FOR THE APPLICATION OF X-RAY-BASED TECHNIQUES TO BIOLOGICAL SAMPLES: RADIATION DAMAGE

Although X-ray-based techniques are promising tools to study NP-drugs and other nanomaterials *in situ*, there are still issues that must be addressed before they can be used to their full potential. For example, there is a lack of suitable labeling methods that enable detecting simultaneously the different components of NP-drugs. Moreover, while probing the variations in the chemical properties of metal nanomaterials using XAS with nm resolution has been possible *in vitro*,<sup>148,408–412</sup> its application to biological samples has been limited due to concentration and sensitivity issues. Using longer acquisition times to obtain meaningful spectra is not always possible, as it normally causes unwanted radiation damage. Also, to achieve time-lapse *in vivo* recordings using X-rays, the challenge is to keep organisms alive; prolonged excitation time can lead to significant beam damage to biological samples. In particular, it remains a great challenge to track the fate and degradation/transformation of NPs *in vivo*, as the pristine NPs may break down and corrode into smaller NPs, clusters, molecules, or ions, due to the cellular and biomolecular interactions under the biological settings. Thus, concerning long-term tissue penetration, sometimes only some debris from the original NPs might be able to be translocated into an individual cell, or cells only would retain few NPs after a long-term therapy or upon a low-dose administration. These circumstances demand extremely high detection sensitivity and resolution of X-ray-based techniques.

Most synchrotron-based X-ray techniques are not capable of analyzing large numbers of samples in a short time. Therefore, they cannot provide data from significant cell populations, limiting the strength of results obtained to some extent. Most of these issues are due to the experimental approaches or set-ups currently used to acquire data using X-ray-based methods. As such, these limitations might be partially or totally overcome by a series of technical improvements currently available or in the process of being implemented. For example, the XFM beamline at the Australian Synchrotron can perform high-throughput analyses, and one study analyzed the uptake of ZnO NPs with roughly 1000 cells.<sup>413</sup> Also, large-area and solid-angle XRF detector

arrays are capable of achieving high-count rates in extremely short times, enabling the collection of on-the-fly, real-time elemental images or high-resolution XAS image stacks minimizing irradiation times,<sup>414–416</sup> while CCD-based energy dispersive 2D detectors can be used to acquire full-field XRF images (both 2D and 3D).<sup>417</sup> Developments in silicon drift detector array chips will increase throughput of the large-area, XRF detector arrays by orders of magnitude.<sup>418</sup> Additionally, the fourth generation of synchrotron radiation sources (ESRF, MAX IV, and upcoming implementation of APS-U and PETRA IV at DESY) will provide access to much brighter and more coherent X-ray photon beams.<sup>330–333</sup> These advances will help to increase the sensitivity of X-ray-based analytic techniques (e.g., sub-ppm for XRF imaging currently).<sup>149</sup> Moreover, such improvements can dramatically reduce the irradiation time needed to obtain good quality data, enabling information collecting from larger populations and minimizing the damage to samples.

In fact, potential beam damage is one of the significant hurdles in advancing X-ray-based analysis toward more *in vivo* applications. Ideally, X-rays should be only an interrogator, leaving the sample (e.g., the NP-based drug) and its environment (e.g., tissue) unaffected. However, if exposure to X-rays is too severe, it can destroy biological molecules and damage tissues. Any radiation would be harmful, especially in terms of cumulative dose, which accounts for its own long-term health risks. Classified as a Group 1 carcinogen by the World Health Organization,<sup>419</sup> any exposure to X-rays can cause DNA mutations, genetic damage, and further the consequent occurrence of cancers. For instance, leukemias have long been known to occur after detrimental radiation of several hundreds of mSv,<sup>420</sup> but according to the widely accepted linear no threshold model, the risk to develop this type of cancer is assumed to increase linearly with dose from zero, and significant effects have recently been reported with doses as low as 50 mSv;<sup>421</sup> although recent reports suggest that the role of radiation on cancer risk is far more complex.<sup>422</sup> In contrast, for general clinical diagnosis in hospitals, the emerging risks of low-dose X-ray radiation below 10 mGy (or 10 mSv considering RBE = 1) are rather low, whereas the cumulative risk of cancer from diagnostic X-ray exposure was estimated to be approximately 0.6–1.8% to the age of 75 years.<sup>423</sup> Nevertheless, radiation risk cannot be excluded from the young and occupational populations.<sup>424,425</sup> Therefore, damage caused by X-rays is an important issue concerning its use in biomedical applications.<sup>426</sup> The mechanism of radiation injury depends predominantly on the changes of biological macromolecules with exposure to X-rays. Radiation can directly interact with biological macromolecules and induce their ionization and excitation, resulting in molecular structure changes and loss of biological activity. Free radicals formed by X-rays can, in turn, damage biomolecules and, in particular, DNA. Meanwhile, the ionized and excited molecules are unstable, and the electronic structure within the molecules can be changed. This process can induce decomposition of molecules and changes in their structure, leading to the loss of biological function, especially when chromosomal DNA is affected.

Importantly, in the study of living organisms, radiative injury depends on many factors, including exposure-related factors (e.g., the irradiation time, dosage, fractionation, the size of the exposed area, and its site) and biological factors (e.g., physical structure, hormonal status, oxygen status, tissue

renewal rate, and capillary density). Among them, acute high-dose irradiation may cause more tissue damage, including acute and chronic injuries, than long-term low-dose exposure with the same total dose. The extent of radiation damage often differs between different biological tissues and organs (e.g., skin, bone marrow, etc.). For instance, when the entire or a part of the body is exposed to X-rays, the skin, as an external organ, is first damaged to initiate and to promote skin radiation injury, including acute skin burns, chronic skin fibrosis, and, rarely, skin cancer.<sup>427–429</sup> Bone marrow is one of the main sensitive target tissues following ionizing radiation exposure.<sup>430,431</sup> Various hematopoietic stem and progenitor cells, naive hematopoietic cells in the bone marrow, and mature blood cells in lymphatic tissues are sensitive to radiation. Particularly when the bone marrow is exposed to large doses of X-rays, hematopoietic stem cells suffer a greater degree of radiation damage, and their self-renewal, proliferation, and differentiation will appear unbalanced, manifested as weakened self-renewal, resulting in serious reductions or even depletions of hematopoietic stem cells, which ultimately leads to bone marrow hematopoietic failure and loss of immune function. Although tremendous progress has been made in the prevention and treatment of radiation damage, there remains major scientific issues that need to be studied and overcome. These issues include not only the differences in radiosensitivity of different tissues and organs and the physiological damage caused to sensitive tissues and organs under high-dose irradiation but also the development of countermeasures against normal tissue radiation injury. The cumulative radiation dose should also be considered in preclinical animal models. In order to reach an optimal signal-to-noise ratio and high spatial resolution in X-ray-based analyses, relatively high radiation doses are necessary. Such high doses will not allow repeated measurements since high total body doses are lethal because of the bone marrow suppression. Second, high radiation doses certainly affect the experimental animal models and outcomes, that is, immune responses, tumor microenvironment, and/or tumor growth. Thus, the fate and therapeutic effect of NPs measured by X-ray-based methods should be re-evaluated using multimodality methods considering the effects of cumulative radiation doses on the animals.

For *in vivo* X-ray imaging of living organisms, radiation parameters such as dose limits need to be established. Here, a molecular understanding of radiation damage in model systems, such as NPs co-crystallized with proteins,<sup>432</sup> might help to determine these parameters. X-rays can interact with water in the cells, causing water molecules to ionize or to be excited, to form highly active free radicals and peroxides after a series of reactions. These species actions on biological macromolecules can lead to changes in molecular structure and function, causing dysfunction and systemic lesions. In this context, X-ray protein crystallography may provide important insights into radiation damage at the molecular level, because it has a strong background on studying the effects of irradiating hydrated biological macromolecules with X-rays.<sup>433</sup> In protein crystals, prolonged exposure to X-rays may alter structural features such as side chains or oxidation states of metal ions within the protein or affect global parameters such as unit cell dimensions.<sup>434</sup> Strategies to overcome the site-specific and global radiation damage are, for example, low-temperature data collection<sup>435</sup> and the determination of dose limits.<sup>436</sup> Typically, synchrotron-based

characterization of biological samples has been conducted through the use of microfluidics or using frozen or crystallized samples. Recent advances in near-ambient X-ray spectroscopy open the door to studying the behavior of NPs in biological samples under near-physiological conditions.<sup>437</sup> With the advent of serial crystallography methods, including experiments with XFEL sources, most studies are carried out at room temperature. Here, radiation damage is mitigated by using a large number of irradiated species. Either the radiation is distributed over a large number of crystals or, in the case of XFEL studies, the diffraction outruns the destruction of the crystals. Thus, only minimal radiation damage is observed in the final data.<sup>438</sup> For investigation of nano–bio interactions, these serial approaches might be suitable for minimizing radiation damage in cellular studies. Here, a high throughput of cellular material could ensure limited radiation damage after data processing. Such an approach also requires further development of serial X-ray-based imaging techniques, as discussed above.

There are strategies to reduce the impact of radiation damage. While large biological objects can readily be investigated by X-rays, microscopy of small biological objects, such as cells with high spatial resolution, risks potential radiation damage.<sup>439</sup> Due to the ionizing nature of X-rays, radicals can be formed that lead to the cleavage of chemical bonds and cause structural changes,<sup>440</sup> which become particularly obvious when nonconductive biological objects are analyzed.<sup>441</sup> According to the empirical Rose criterion, the dose required for imaging an object reliably against the background noise increases with the desired resolution.<sup>442</sup> Thus, the achievable resolution is ultimately limited by the X-ray dose that can be applied before radiation damage occurs.<sup>443,444</sup> The impact of radiation damage on biological samples critically depends on their environment and sample preparation. For many mammalian cells already,  $\approx 10$  Gy is deadly.<sup>445</sup> Elemental redistributions in XRF of unfixed vanadocytes and mass loss in dried chromosomes were observed for doses  $>10^5$  Gy.<sup>446,447</sup> As the resistance against radiation damage rises exponentially with decreasing temperature,<sup>448</sup> structure determination by X-ray-based biocrystallography could be greatly improved when done at cryogenic temperatures, as much higher radiation doses can be applied than at room temperature.<sup>449</sup> When investigated under cryogenic conditions, the diffraction signal of lysozyme crystals remained visible up to radiation doses of  $10^7$  Gy.<sup>450</sup> In X-ray microscopy, the tolerable radiation dose for imaging before artifacts due to radiation damage occur was calculated to be  $10^8$ – $10^9$  Gy.<sup>451</sup> An additional advantage of cryogenic sample preparation, particularly for X-ray fluorescence analysis, is the preservation of the location of ions as close to the natural, hydrated state as possible. This feature was demonstrated by imaging the elemental distribution within duckweed roots,<sup>452</sup> green algae,<sup>453</sup> and fibroblast cells.<sup>454</sup> While cryo-preparation of the samples is usually performed in the biological laboratories, transfer systems are required to deliver the frozen samples free of contaminants to the experiment. During measurements, the samples are kept in the frozen state either by a cryo-stream<sup>452</sup> or in a vacuum chamber using cooled sample stages.<sup>453</sup>

Another possibility would be to harness the molecular machinery of cells. Consider that in addition to the direct and indirect effects discussed above, X-ray radiation can trigger a series of biochemical and molecular signaling events

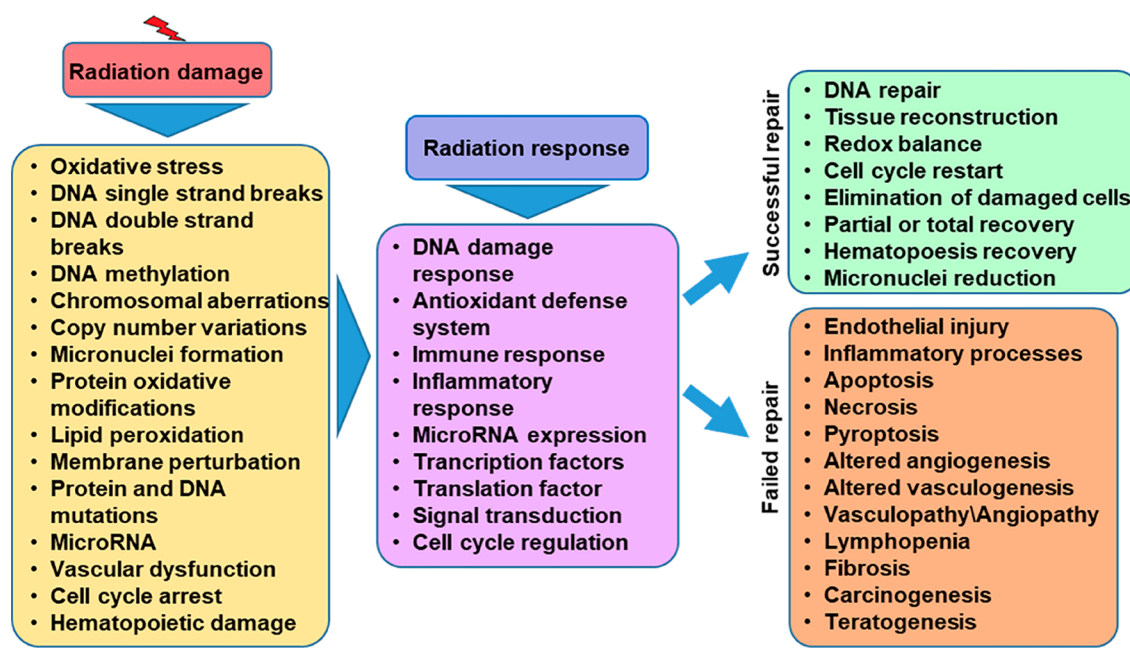


Figure 20. Mechanisms involved in radiation damage and subsequent radiation response.

together forming or providing the radiation response of the organism (Figure 20) that may either repair the radiation-induced damage or result in long-term physiological changes or cell death. DNA damage can be caused even by irradiation as low as 1 mGy, and DNA repair proteins are recruited to these damaged sites.<sup>455</sup> Important factors in radiation response are DNA repair,<sup>455,456</sup> antioxidant defense systems,<sup>457</sup> and immune and inflammatory responses.<sup>458–460</sup> These systems provide the organism with highly effective protection against radiation-induced ROS and DNA damage, but they can also trigger long-term adverse effects. The efficiency of these radioprotective systems is reduced, and even plays a reverse role in the case of high-dose irradiation. This response is due to (i) abundant generation of radiation-induced ROS that affects the oxidant–antioxidant balance of the organism and causes potentially lethal DNA damage and (ii) radiation-induced mutations caused by erroneous repair. Consequently, high-dose irradiation can result in the alteration of enzyme activities and trigger uncontrolled inflammatory responses,<sup>461</sup> which in turn can cause secondary vascular dysfunction and tissue damage with the subsequent activation of a variety of cell death mechanisms, such as apoptosis, necrosis, fibrosis, *etc.*<sup>462</sup>

To reduce radiation damage during X-ray-based *in vivo* research and in clinical radiotherapy, different natural or synthetic radioprotective agents have been shown to moderate radiation-induced molecular and cellular damage and/or to restore the physiological balance of the organism *in vitro*, *in vivo*, or in human randomized controlled trials. The radioprotective effect of such compounds is provided mostly by their antioxidative and immunomodulatory features, as they are able to suppress free radical production, remove already generated free radicals, and reduce radiation-induced inflammatory response.<sup>463</sup> Another approach to mitigating radiation damage is the use of local radioenhancers, which would achieve higher on-site radiation at tumor cells or at the region of interest by applying lower overall radiation doses.<sup>464</sup> Despite the large number of radioenhancers synthesized and

studied even at the level of clinical trials,<sup>465</sup> they are not largely used in clinical practice. Moreover, their application in NP research is also challenging, as it requires additional studies on whether the particular radioenhancer interacts with the NPs directly or has any indirect effects on the NP-based drug or NP carrier delivery.

When considering the applications of X-rays applied to biological samples, the use of the above-discussed imaging and spectroscopic techniques, especially to large biological specimens (such as whole mice or humans) will also need to address the issue of the trade-off between X-ray tissue penetration and the quality of the signals obtained. As described above, X-ray radiation can be divided into low-penetrating soft and tender X-rays (100 eV to 1 keV and 1 to 5 keV, respectively, penetrating up to a few  $\mu\text{m}$ ) and high-penetrating hard X-rays (5 keV and higher). However, the penetration of hard X-rays is controlled by their energy. As such, X-rays with energies of *ca.* 15 keV are needed to penetrate over 1 cm of tissues, while much higher energies are required to analyze whole organisms. Up to 50 keV, the interactions of hard X-rays with tissue are dominated by photoabsorption events, which enable acquisition of multiple images and spectra with low background. It is thus possible to obtain easily high-quality XRF maps, XAS spectra, or scattering images (among others) in cell samples or *ex vivo* tissue samples (up to a couple of cm thick). However, at energies over 50 keV, the interaction between X-rays and tissue is dominated by inelastic Compton scattering. Although not critical for medical imaging (which uses X-rays in the energy range 10–150 keV), such scattering events can lead to the generation of large background noise and make it difficult to acquire maps of most elements, and other images and spectroscopic data. Thus, it will be necessary to develop improved acquisition and/or data analysis methods to reduce the background created by Compton scattering before certain X-ray-based analytics (*i.e.*, XRF, or XAS-based techniques) can be properly applied *in situ*. There is progress in this direction, as described above. In

a recent report, the localization of Au NPs on both tumor models and objects with human-size scales was determined with XFI by applying a spatial filtering scheme for background reduction, applying a local dose of only 10 mGy within the scanning X-ray beam volume, resulting in an even lower effective organ dose, as only parts of the body were scanned by XFI.<sup>57</sup>

Finally, most X-ray techniques that can be used to study NP-drugs in organisms currently require the use of synchrotron facilities. Therefore, the methodologies developed for those synchrotron-based tools will need to be transferred to benchtop environments if we want to apply X-ray-based analytics to clinically relevant situations. Although XRF elemental maps can be obtained from mice using current benchtop X-ray sources,<sup>466</sup> they cannot reach the flux, coherence, or subcellular resolution achieved by synchrotron-based nanoprobe beamlines and still need to be improved significantly to reach adequate performance.

### PERSPECTIVES AND OUTLOOK

Tissue is nontransparent to probes used in many analytical methods. However, for future biomedical applications concerning delivery, imaging, and diagnostics, the use of *in situ* analytics that include monitoring what is happening inside tissue at the (sub-) cellular level will be important. In biological media, NPs may interact with cells, organelles, and molecules,<sup>353</sup> resulting in variations in aggregation, distribution, surface properties, and chemical environment and even in the structures of the NPs. Meanwhile, the biological functions and structures of the biological components are also affected by nano–bio interactions. For example, many metal NPs have been designed for nanomedicine. Compared to traditional pharmaceuticals, NP-based drug delivery may exhibit distinct pharmacokinetic and pharmacodynamics properties, which rely on step-by-step interactions between the NPs and the biological targets. The intracellular localization and the chemical transformation (valence state or chemical environment variation) of the NPs are critical to their biological functions and may help us to understand the degradation of NPs and the toxicological mechanisms of NPs. When NPs are treated with external stimuli to react with biological systems, *in situ* analyses could provide direct and visual details on physiological and pathological development. These details would offer better understanding of dynamic regulation in biological homeostasis. However, it is not currently possible to obtain detailed and comprehensive understanding of the (biological or molecular) events that affect NPs once inside the body of animals and humans. Detailed analytics can be achieved by testing blood samples, which, unfortunately, is not a local technique. It is possible to perform local analytics *ex vivo* on dissected organs, which is neither *in situ* nor applicable to humans. Thus, comprehensive *in situ* analytics at the molecular/cellular level are needed that make the body “transparent”, in order to observe the site of action. Therefore, the aim of this Review lies in highlighting the need for developing X-ray-based methods that are suitable for studying nanomaterials in complicated biological environments. Applications to humans and translation to the clinic of the techniques discussed here will often not be possible within a short time frame, but *in vivo* work on animals is already in the exploration stage.

This methodology would apply generally to all optically nontransparent samples and could also be used for other

applications, such as environmental analysis and toxicology. Nanomedicine needs to look to other fields dealing with nano–bio interactions for inspiration. In this respect, toxicology has been using X-rays to track and to monitor the distributions of metal and metal–organic NPs in plants and animals for decades, and similar approaches could be straightforwardly adapted for drug delivery. XRF and STXM can be combined with XANES to identify the intracellular fate of ZnO NPs, with which it was found that toxicity can arise due to the dissolution of Zn and its complexation with molecules in the cell.<sup>467</sup> In animals, the biodistribution of copper NPs in earthworms was monitored by XRF and the speciation of the copper by EXAFS.<sup>468</sup> Additionally, the woody tissue of plants makes them ideal for testing X-ray based characterization techniques. SAXS has been used to monitor the formation and trafficking of Zn-based MOFs in plants.<sup>469</sup> In another experiment, after uptake by algae, EXAFS was used to determine that Ag NPs can dissolve into Ag<sup>+</sup>, but then reaccumulate into different cellular compartments.<sup>470</sup> By combining, X-ray microscopy, XANES, and electron microscopy, it was found that a wide size range of Au NPs can be taken up into the vasculatures of land plants, but only the smallest (~3.5 nm) can then be internalized into the plant cells.<sup>471</sup>

For breakthroughs in applications in humans, it will be necessary to address not only the issues of potential radiation damage but also the development of improved laboratory X-ray sources and table-top or compact synchrotrons for clinical applications with low flux. Current laboratory X-ray sources can generate stable (both in emission and position) and reasonably brilliant ( $10^7$ – $10^8$  ph/s in the focus) micro- and nanofocused hard X-ray beams with certain levels of coherence that enable imaging on small animals and *ex vivo* tissue samples.<sup>243,248</sup> Still, they normally produce polychromatic or broadband radiation that cannot be tuned and with much lower overall brilliance (at least 1000 times lower) and coherence than synchrotron sources, which makes it difficult to translate many synchrotron-based X-ray techniques to a laboratory or clinical environment. It is possible to produce highly monochromatic and collimated hard X-ray beams (*i.e.*, with energies between 15 and 35 keV) with a brilliance (about  $10^{10}$  ph/s) intermediate between that of laboratory sources and synchrotron facilities using CLS based on inverse Compton scattering.<sup>472,473</sup> CLS can be installed in biomedical research institutions or hospitals and produces radiation that is stable enough for the acquisition of X-ray imaging,<sup>474</sup> including *in vivo* experiments,<sup>285–287</sup> but also can be used to perform X-ray spectroscopy experiments (*i.e.*, XAS).<sup>475</sup> Still, NP-based drugs are normally found at very low concentrations inside patients. Therefore, CLS would need to improve greatly before we can start thinking about applying such techniques to study NP-based drugs *in situ*, if possible at all.

The technological requirements for moving from synchrotron to conventional sources required for any successful translation to human patients already seems possible, in certain cases. One example of this opportunity is the application of gratings-based set-ups for the diagnosis of lung conditions using dark-field imaging.<sup>476–479</sup> Gratings-based methods were demonstrated for phase-contrast imaging using synchrotron sources almost 20 years ago.<sup>480,481</sup> The same approach was later used to acquire both phase-contrast<sup>482</sup> and dark-field images<sup>483</sup> with conventional X-ray

sources, helping to bring them closer to the clinic. Gratings-based dark-field imaging proved to be promising and has been employed successfully in *in vivo* preclinical studies with animals of different sizes, from mice<sup>476–478</sup> to pigs.<sup>479</sup> Current efforts are directed to optimize the technique for use in humans, by testing it on cadavers,<sup>484,485</sup> and will hopefully translate into clinical practice in the near future. Nevertheless, analytical methodologies that can be used to study NP-based drugs with laboratory instruments must be developed and optimized, which can be done now using state-of-the-art synchrotron facilities.

Next, we consider other potential medical applications of X-ray-based imaging for possible future clinical use. A number of pilot studies described above have illustrated the potential for imaging small animals with synchrotron X-ray-based methods. No single method yields all relevant information, and therefore, multimodal imaging should be considered, complementing the assessment by synchrotron X-rays with other non-invasive imaging approaches, preferably employing multimodal labels such as Au NPs. This strategy would enable combining longitudinal animal studies with synchrotron X-rays in *in vivo*–*in situ* assessments of intact animals or excised tissue for final examinations *ex vivo*. Another exciting opportunity would be to collect human tissue, for example, from organ transplantation or tumor resection surgery, to keep that tissue functional, and to study these specimens with synchrotron X-ray technologies.<sup>486</sup> Similarly, bioreactors containing and preserving large tissue constructs and 3D *in vitro* tumor models for drug evaluation could also be used.<sup>487,488</sup> Analyses of the perfused tissue could provide valuable insight into cellular uptake of NPs and subsequent responses. For example, for tomography with resolution below 1  $\mu\text{m}$ , one could study 3D receptor distributions on tumors or other cells and thus tumor heterogeneity. It may be possible to detect single receptor-scale events using Au NPs and high-affinity antibodies, thus elucidating the targeting process. This insight could help to achieve accurate molecular imaging where still living tissue could be imaged and investigated with single-receptor resolution and sensitivity to understand and to improve drug delivery by nanocarriers.

Cancer is the leading cause of death worldwide. It is estimated that by 2030, the number of cancer cases will increase by more than 50% to 22 million per year.<sup>489</sup> Early detection and optimal therapy of cancer largely depend on patho-anatomical information provided by imaging. Nearly all aspects of patient care require precise visualization of spatial information, that is, the tumor site, its anatomic relation to adjacent structures including displacement and/or infiltration of healthy organs as well as probable spreading to distant organs. Treatment decisions are made by multidisciplinary teams consisting of medical specialists of various disciplines, who collect history, clinical information, family and genetic data, laboratory data, and imaging data about the patient. Spatial information provided by imaging is an essential pillar of many diagnostic as well as therapeutic interventions, such as biopsy, surgery, radiation therapy, and minimally invasive focal as well as systemic therapies. Therapy planning and response are not only based on precise information on the localization, extension, and spreading of the tumor but also on the individual anatomy of the healthy structures. The overall quality of patient care depends on the quality of cancer imaging and repeated imaging over the course of years

of patient care. Over the last five decades, medical imaging technologies have been improved by the invention of cross-sectional imaging technologies providing unforeseen opportunities for patient care. Various methods of ultrasound, CT, MRI, and positron emission tomography (PET/CT and PET/MRI), along with advances in computer science, provide high-resolution 3D visualization of anatomical and functional tumor features. While macroscopic medical imaging has improved impressively, the final diagnoses of cancer and the definite decisions on therapeutic strategies inevitably require microscopic information about tumor pathobiology on the cellular, subcellular, and molecular levels. Medical imaging often reaches its intrinsic limits with *ca.* 0.5–0.1 mm spatial resolution. This limit is not only technological but also due to human anatomical and physiological restrictions related to the size of the human body, tissue movement resulting from, for example, a beating heart, breathing, and bowel peristalsis, as well as the need for the lowest possible radiation exposure to the patient and limited examination time. To bridge this gap of the “nano–bio interface”, tissue often has to be sampled for further examination outside of the body. It is important to realize that small tissue samples must represent the disease characteristics and consequently critically depend on the right selection and extraction of tissue out of a heterogeneous tumor and peritumoral tissue identified by macroscopic imaging. A pathway of optimum cancer diagnostics in the clinical setting should follow a stepwise approach from macro- to microscale, bridging the nano–bio interface: (i) detection and localization of suspicious, potentially cancerous lesions by whole-body imaging (CT, MR, PET/CT, PET/MR); (ii) visualization of local tumor extensions and tumor heterogeneity by local high-resolution multiparametric imaging; (iii) high-precision sampling of representative tumor tissue by sophisticated image-guided biopsy methods; (iv) microstructural characterization of cellular, subcellular, and molecular features using ultrahigh-resolution synchrotron imaging; and finally (v) integration and evaluation of the entire set of multiplexed data exploiting deep-learning bioinformatic methods, leading to clinically relevant information on diagnosis, potential treatment, and prognosis. Possible fields of application are widely spread and include a variety of cancers, for example, prostate, breast, lung, pancreas, *etc.*

Another potential medical application would be XFI *in vivo* cell tracking in live animals, for example, tracking T cells (labeled with metal NPs or molecules suitable for XFI detection, such as iohexol) in immune-mediated inflammatory diseases (IMIDs). These diseases are a group of seemingly unrelated medical conditions affecting multiple organs, such as autoimmune hepatitis, nephritis, multiple sclerosis, and inflammatory bowel disease (IBD). All of these diseases are characterized by dysregulated immune response and nonhealing tissue damage, which promote a vicious cycle leading to chronic disease.<sup>490–492</sup> Furthermore, chronic inflammation can promote the development of cancer. IBD, for example, is associated with colorectal cancer, especially in patients suffering from chronic intestinal inflammation. IMIDs are already among the leading causes of mortality in developed countries, and their prevalence is increasing.<sup>490–492</sup> However, in most cases, current therapies are palliative and do not offer cures. Indeed, most therapies are based on immune-suppressive drugs, but are not able to reestablish homeostasis between the immune system, the tissue, and the

microbiota. The resulting problems are relapsing flares and opportunistic infections that occur as a consequence of immune suppression. Thus, there is a major need for improved targeted therapies. Of note, CD4<sup>+</sup> T cells are characteristic of the inflammation seen in IMIDs, and recent genome-wide association studies indicate that they do play key roles in the etiology of IMIDs and especially IBD.<sup>493</sup> These data are further supported by murine studies, which have shown that an imbalance of effector T helper (T<sub>H</sub>) subsets and regulatory T cells, such as Foxp3<sup>+</sup> T regulatory (T<sub>REG</sub>) and IL-10-producing Foxp3<sup>Neg</sup> type 1 regulatory T cells (T<sub>R1</sub>), plays important roles in IMIDs.<sup>494–499</sup> CD4<sup>+</sup> T cells are central players in adaptive immune responses. Naïve CD4<sup>+</sup> T cells differentiate into a plethora of T<sub>H</sub> subsets, including T<sub>H</sub>1, T<sub>H</sub>2, T<sub>H</sub>17, and T<sub>H</sub>22 effector T cells with exquisite levels of functional specialization. Accordingly, one problem to understand is the spatiotemporal dynamics of these T-helper cell subsets during IMIDs and cancer. Note that inflammatory responses are different in distinct IMIDs and cancer. Intravital microscopy could be useful for this task, as it has been used successfully to explore *in vivo* and *in situ* immunological responses in surface tissues of animals (100–200 μm deep).<sup>107–109</sup> However, until now, there has been no *in vivo* imaging method that would allow tracking several different T cell subsets at the same time in an entire animal with sufficient spatial and temporal resolution. There are trade-offs between increasing spatial *versus* temporal resolution, but detection of a small local number of marked T cells should be possible. Furthermore, current therapies are known to modulate T-helper cell responses. Therefore, a suitable *in vivo* imaging technology would have the potential not only to answer basic scientific questions but also to identify biomarkers for diagnoses of different IMIDs and to track the responses to specific therapies. By using different XFI tracers (either molecular or NP-based) that have similar sensitivities, several different types of immune cells could be tracked in a single measurement. The different T cells could be preloaded with different contrast, providing molecular agents or NPs *via* endocytosis, as has been demonstrated for stem cells and macrophages.<sup>500</sup> By spatial filtering, the imaging sensitivity, in terms of the minimum local amount of XRF tracers, could be minimized, meaning that a small number of XFI-labeled immune cells could be visible *via* XFI in living animals.

Radiation damage has been discussed as a looming hurdle concerning the safety of *in vivo* X-ray analytics. On the other hand, such radiation damage to tissue *via* NPs could also be used for *treatment*, in which X-rays are intentionally used to destroy malignant tissue. Here, X-ray-based imaging techniques for detecting metallic NPs have important potential roles in radiation therapy. Ideally targeted delivery of metallic NPs to a tumor can be leveraged to increase the efficacy of radiation therapy.<sup>501–503</sup> On one hand, high-resolution imaging of NPs could provide more accurate, single-cell localization of the tumor prior to irradiation, thus largely sparing surrounding healthy tissue.<sup>504,505</sup> X-rays interacting with strongly absorbing metallic NPs deposit greater fractions of incident photon energy, thereby releasing higher amounts of low-energy secondary electrons, fluorescence X-rays, and ROS where needed. Both secondary electrons and ROS can further increase cellular damage, so that metallic NPs selectively accumulated in tumor tissue could be used as radiation sensitizers for cancer therapy. While the physical

processes involved in the mechanisms of NP-mediated radiosensitization are being modeled with increasing accuracy,<sup>506,507</sup> the roles of related chemical and biological processes are not fully understood.<sup>504,507</sup> Since measurements of radiation-induced free radicals are quite complex, only a few experiments have performed to date. For example, it was found that Au NPs directly and indirectly increase hydroxyl and superoxide production in water.<sup>508–510</sup> Experiments with macrophages incubated with Au and FeO<sub>x</sub> NPs could visualize the spatial patterns of hydroxyl radicals and superoxide anions produced by fluorescence X-rays and Auger electrons that were emitted upon cell irradiation with a scanning polychromatic synchrotron microbeam. These experiments showed that, while enhanced radical production from Auger electrons is limited to a range of *ca.* 100 μm from the NP-loaded cell, fluorescence X-rays can increase this production up to a distance of 1.5 mm for FeO<sub>x</sub> NPs and to 2 mm for Au NPs, respectively. Therefore, for enhancing radiation-induced cell damage for cancer treatment, *in situ* spatial distributions of specific NP systems, as well as biokinetics, possible toxicity, and tumor-targeting efficiencies will need to be thoroughly investigated prior to clinical implementation.

While this Review has predominantly addressed synchrotron-based X-ray analytics, the potential of XFELs should also be highlighted. XFELs, offering mJ pulse energies at hard X-ray energies and delivered in subhundred fs pulses, provide additional opportunities for structural investigations of NPs in both the physical and life sciences. These studies are typically performed either by exploiting the short pulse duration for time-resolved investigations<sup>511</sup> or by leveraging the extreme pulse intensity to “outrun” radiation damage (caused by the X-ray–matter interactions) to determine the structures of noncrystalline (bio) materials at high resolution.<sup>512</sup> Indeed, ultrafast pump–probe capabilities with XFELs have been demonstrated using solution-based samples.<sup>513</sup> Pump–probe methods enable powerful means of data collection, including fs X-ray crystallography and temporal resolution of chemical processes spanning charge transfer and bond cleavage. Moreover, ultrafast pump–probe capabilities are superbly positioned to access NP dynamics in biological samples and are crucial in assessing the viability of some nanomaterials-based therapeutic approaches such as highly localized pulsed photothermal heating.<sup>514</sup>

In general, using coherent single-particle imaging (SPI) with free electron lasers, the 3D structures of biological samples can be investigated. SPI has progressed from observations of single cells,<sup>515,516</sup> cellular substructures,<sup>517</sup> and large viruses<sup>518</sup> to the determination of the conformational landscape of smaller viruses.<sup>519</sup> Simulations now suggest that the structures of single protein molecules can be determined at sub-nm length scales during experimental time allocated at high-repetition rate XFELs.<sup>520</sup> Such high rates of data collection have been shown to be feasible at, for example, European XFEL (EuXFEL).<sup>521</sup> For inorganic NPs, a large number of X-ray structural investigations are reported from diverse materials such as iron/silica,<sup>522</sup> soot,<sup>523</sup> gold/palladium,<sup>524</sup> thiol/gold,<sup>525</sup> and others, including from heterogeneous populations.<sup>526</sup> These investigations inform both the development of methods applicable to the life sciences and, as outlined earlier, biofunctionalized inorganic NPs (bio–NPs) may be used as carriers to transport biologically active compounds (BAC) such as small

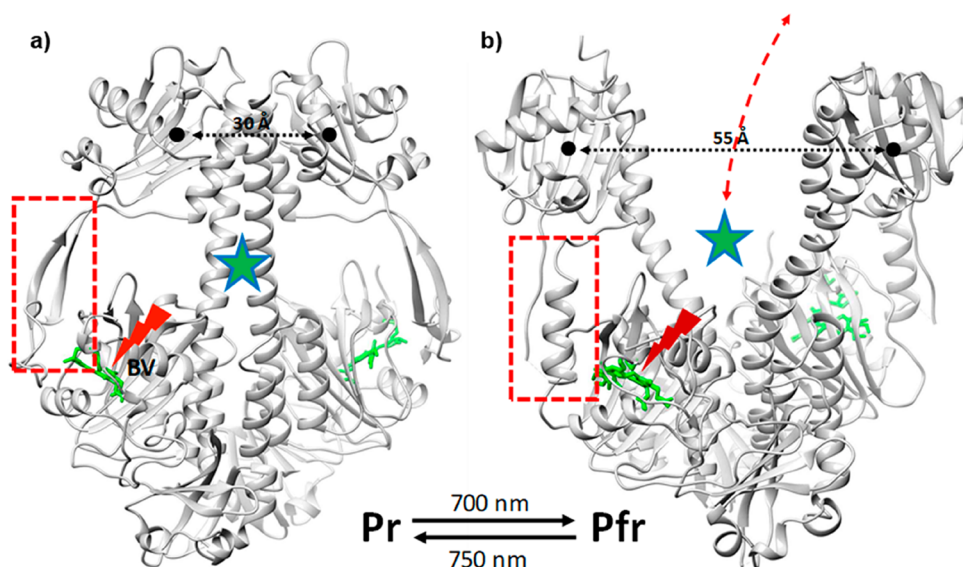


**Figure 21.** Structural changes in phytochrome photosensory core modules. (a) The *Stigmatella aurantiaca* photochrome P2 in the Pr state.<sup>529</sup> The central biliverdin (BV) chromophore is marked. The chromophore absorbs 700 nm red light. Upon light absorption, it isomerizes from a Z configuration to an E configuration. The configurational change triggers a large conformational change. Centroid distance of the movable domain: 30 Å. The sensory tongue (red dashed box) adopts a  $\beta$ -sheet structure. The BAC (green star) is bound. (b) Reaction product after light absorption as depicted by the *Deinococcus radiodurans* phytochrome in the Pfr state.<sup>530</sup> The chromophore absorbs at 750 nm in the far red. The centroid distance of the movable domain is 55 Å. The sensory tongue (red box) then adopts an  $\alpha$ -helical structure. The BAC (green star) is free to leave. The reaction between Pr and Pfr states is reversible to facilitate uptake and release of the BAC.

molecules, peptides, and drugs. One concept is to release BACs (or “drugs”) from their light-sensitive NP carriers by application of an optical laser. Phytochromes are light sensitive and were originally identified in plants and then subsequently found in many other organisms.<sup>527</sup> The large structural changes of the phytochromes upon red light illumination are unmatched (Figure 21). Red light is relatively harmless and, most importantly, penetrates deep into soft tissue. It is conceivable to engineer phytochrome constructs that are specifically optimized for uptake and release of BACs. An advantage would be that intense red light could be applied simultaneously and localized to multiple positions allowing for the treatment of multiple sites at the same time. To investigate the mechanism of BAC uptake and release by these light controlled bioinorganic nanomachines, their structures must be determined to high enough resolution that is roughly equivalent to the amplitude of the structural changes after light illumination.<sup>528–530</sup> Resolution between 1 and 2 nm should be sufficient (Figure 21). These experiments are likely to become feasible in the near future with existing free electron lasers.<sup>521</sup> We anticipate that such SPI experiments are extremely “photon hungry”, both in photons per X-ray pulse and in the number of pulses (and hence diffraction images) collected.<sup>531</sup> The EuXFEL is presently the world’s highest repetition rate XFEL, offering up to 3520 measured images per sec—more than an order of magnitude more than the next XFEL source. This repetition rate enables the collection of large data sets in reasonable measurement times and bodes well for the applicability of this method to both organic and inorganic NPs.<sup>532</sup>

Improvements in the development of X-ray light sources will enable their use for biological/medical experiments that have not yet been feasible. Inorganic NPs, due to their high X-ray absorption cross sections and their potential con-

jugation with BACs/drugs, are an important part of the molecular and nanoscience toolkits for exploiting such developments. We anticipate that there will be increases in the uses of X-ray techniques to explore the fates and mechanisms of therapeutic nanomaterials once administered to animal models and patients. We further expect applications to experiments in laboratory, preclinical, and clinical environments, as large efforts are currently directed to developing improved compact X-ray sources. We foresee that X-rays will have important, fundamental roles in the advance of nanomedicine toward its maturity over the next decades.

## AUTHOR INFORMATION

### Corresponding Author

**Wolfgang J. Parak** – Mathematics, Informatics, and Natural Sciences (MIN) Faculty, University of Hamburg, 20354 Hamburg, Germany; Center for Cooperative Research in Biomaterials (CIC biomaGUNE), Basque Research and Technology Alliance (BRTA), 20014 Donostia San Sebastián, Spain; School of Chemistry and Chemical Engineering, Frontiers Science Center for Transformative Molecules and National Center for Translational Medicine, Shanghai Jiao Tong University, Shanghai 200240, China; [orcid.org/0000-0003-1672-6650](https://orcid.org/0000-0003-1672-6650); Email: [wolfgang.parak@uni.hamburg.de](mailto:wolfgang.parak@uni.hamburg.de)

### Authors

**Carlos Sanchez-Cano** – Center for Cooperative Research in Biomaterials (CIC biomaGUNE), Basque Research and Technology Alliance (BRTA), 20014 Donostia San Sebastián, Spain; [orcid.org/0000-0002-9522-0019](https://orcid.org/0000-0002-9522-0019)  
**Ramon A. Alvarez-Puebla** – Universitat Rovira i Virgili, 43007 Tarragona, Spain; ICREA, 08010 Barcelona, Spain; [orcid.org/0000-0003-4770-5756](https://orcid.org/0000-0003-4770-5756)

- John M. Abendroth** – Department of Materials Science and Engineering, Stanford University, Stanford, California 94305, United States; [orcid.org/0000-0002-2369-4311](https://orcid.org/0000-0002-2369-4311)
- Tobias Beck** – Mathematics, Informatics, and Natural Sciences (MIN) Faculty, University of Hamburg, 20354 Hamburg, Germany; [orcid.org/0000-0001-7398-3982](https://orcid.org/0000-0001-7398-3982)
- Robert Blick** – Mathematics, Informatics, and Natural Sciences (MIN) Faculty, University of Hamburg, 20354 Hamburg, Germany
- Yuan Cao** – Department of Chemical Engineering and Biointerfaces Institute, University of Michigan, Ann Arbor, Michigan 48109, United States; [orcid.org/0000-0002-3544-2664](https://orcid.org/0000-0002-3544-2664)
- Frank Caruso** – ARC Centre of Excellence in Convergent Bio-Nano Science and Technology and the Department of Chemical Engineering, The University of Melbourne, Parkville, Victoria 3010, Australia; [orcid.org/0000-0002-0197-497X](https://orcid.org/0000-0002-0197-497X)
- Indranath Chakraborty** – Mathematics, Informatics, and Natural Sciences (MIN) Faculty, University of Hamburg, 20354 Hamburg, Germany
- Henry N. Chapman** – Mathematics, Informatics, and Natural Sciences (MIN) Faculty, University of Hamburg, 20354 Hamburg, Germany; Centre for Ultrafast Imaging, Universität Hamburg, 22761 Hamburg, Germany; Deutsches Elektronen-Synchrotron DESY, 22607 Hamburg, Germany; [orcid.org/0000-0002-4655-1743](https://orcid.org/0000-0002-4655-1743)
- Chunying Chen** – National Center for Nanoscience and Technology (NCNST), 100190 Beijing, China; [orcid.org/0000-0002-6027-0315](https://orcid.org/0000-0002-6027-0315)
- Bruce E. Cohen** – The Molecular Foundry and Division of Molecular Biophysics and Integrated Bioimaging, Lawrence Berkeley National Laboratory, Berkeley, California 94720, United States; [orcid.org/0000-0003-3655-3638](https://orcid.org/0000-0003-3655-3638)
- Andre L. C. Conceição** – Deutsches Elektronen-Synchrotron DESY, 22607 Hamburg, Germany
- David P. Cormode** – Radiology Department, University of Pennsylvania, Philadelphia, Pennsylvania 19104, United States; [orcid.org/0000-0002-8391-9500](https://orcid.org/0000-0002-8391-9500)
- Daxiang Cui** – School of Chemistry and Chemical Engineering, Frontiers Science Center for Transformative Molecules and National Center for Translational Medicine, Shanghai Jiao Tong University, Shanghai 200240, China; [orcid.org/0000-0003-4513-905X](https://orcid.org/0000-0003-4513-905X)
- Kenneth A. Dawson** – University College Dublin, D04 VIW8 Dublin, Ireland; [orcid.org/0000-0002-0568-6588](https://orcid.org/0000-0002-0568-6588)
- Gerald Falkenberg** – Deutsches Elektronen-Synchrotron DESY, 22607 Hamburg, Germany
- Chunhai Fan** – School of Chemistry and Chemical Engineering, Frontiers Science Center for Transformative Molecules and National Center for Translational Medicine, Shanghai Jiao Tong University, Shanghai 200240, China; [orcid.org/0000-0002-7171-7338](https://orcid.org/0000-0002-7171-7338)
- Neus Feliu** – Mathematics, Informatics, and Natural Sciences (MIN) Faculty, University of Hamburg, 20354 Hamburg, Germany; CAN, Fraunhofer Institut, 20146 Hamburg, Germany; [orcid.org/0000-0002-7886-1711](https://orcid.org/0000-0002-7886-1711)
- Mingyuan Gao** – Department of Radiotherapy and Radiation Oncology, University Medical Center Hamburg-Eppendorf, 20246 Hamburg, Germany; [orcid.org/0000-0002-7360-3684](https://orcid.org/0000-0002-7360-3684)
- Elisabetta Gargioni** – Department of Radiotherapy and Radiation Oncology, University Medical Center Hamburg-Eppendorf, 20246 Hamburg, Germany
- Claus-C. Glüer** – Section Biomedical Imaging, Department of Radiology and Neuroradiology, University Medical Clinic Schleswig-Holstein and Christian-Albrechts-University Kiel, 24105 Kiel, Germany
- Florian Grüner** – Mathematics, Informatics, and Natural Sciences (MIN) Faculty, University of Hamburg, 20354 Hamburg, Germany; Universität Hamburg and Center for Free-Electron Laser Science, 22761 Hamburg, Germany
- Moustapha Hassan** – Karolinska University Hospital, Huddinge, and Karolinska Institutet, 17177 Stockholm, Sweden; [orcid.org/0000-0003-1927-5859](https://orcid.org/0000-0003-1927-5859)
- Yong Hu** – College of Engineering and Applied Sciences, Nanjing University, Nanjing 210093, China; [orcid.org/0000-0002-5394-6743](https://orcid.org/0000-0002-5394-6743)
- Yalan Huang** – Mathematics, Informatics, and Natural Sciences (MIN) Faculty, University of Hamburg, 20354 Hamburg, Germany
- Samuel Huber** – Department of Radiotherapy and Radiation Oncology, University Medical Center Hamburg-Eppendorf, 20246 Hamburg, Germany
- Nils Huse** – Mathematics, Informatics, and Natural Sciences (MIN) Faculty, University of Hamburg, 20354 Hamburg, Germany; [orcid.org/0000-0002-3281-7600](https://orcid.org/0000-0002-3281-7600)
- Yanan Kang** – Mathematics, Informatics, and Natural Sciences (MIN) Faculty, University of Hamburg, 20354 Hamburg, Germany
- Ali Khademhosseini** – Terasaki Institute for Biomedical Innovation, Los Angeles, California 90049, United States; [orcid.org/0000-0002-2692-1524](https://orcid.org/0000-0002-2692-1524)
- Thomas F. Keller** – Mathematics, Informatics, and Natural Sciences (MIN) Faculty, University of Hamburg, 20354 Hamburg, Germany; Deutsches Elektronen-Synchrotron DESY, 22607 Hamburg, Germany; [orcid.org/0000-0002-3770-6344](https://orcid.org/0000-0002-3770-6344)
- Christian Körnig** – Mathematics, Informatics, and Natural Sciences (MIN) Faculty, University of Hamburg, 20354 Hamburg, Germany; Universität Hamburg and Center for Free-Electron Laser Science, 22761 Hamburg, Germany
- Nicholas A. Kotov** – Department of Chemical Engineering, Biointerfaces Institute, and Department of Materials Science and Engineering, University of Michigan, Ann Arbor, Michigan 48109, United States; Michigan Institute for Translational Nanotechnology (MITRAN), Ypsilanti, Michigan 48198, United States; [orcid.org/0000-0002-6864-5804](https://orcid.org/0000-0002-6864-5804)
- Dorota Koziej** – Mathematics, Informatics, and Natural Sciences (MIN) Faculty, University of Hamburg, 20354 Hamburg, Germany
- Xing-Jie Liang** – National Center for Nanoscience and Technology (NCNST), 100190 Beijing, China; [orcid.org/0000-0002-4793-1705](https://orcid.org/0000-0002-4793-1705)
- Beibei Liu** – Department of Radiotherapy and Radiation Oncology, University Medical Center Hamburg-Eppendorf, 20246 Hamburg, Germany
- Sijin Liu** – State Key Laboratory of Environmental Chemistry and Ecotoxicology, Research Center for Eco-Environmental Sciences, Chinese Academy of Sciences, Beijing 100085, China

- Yang Liu** – Mathematics, Informatics, and Natural Sciences (MIN) Faculty, University of Hamburg, 20354 Hamburg, Germany
- Ziyao Liu** – Mathematics, Informatics, and Natural Sciences (MIN) Faculty, University of Hamburg, 20354 Hamburg, Germany
- Luis M. Liz-Marzán** – Center for Cooperative Research in Biomaterials (CIC biomaGUNE), Basque Research and Technology Alliance (BRTA), 20014 Donostia San Sebastián, Spain; Ikerbasque, Basque Foundation for Science, 48013 Bilbao, Spain; Centro de Investigación Biomédica en Red de Bioingeniería, Biomateriales y Nanomedicina (CIBER-BBN), 20014 Donostia-San Sebastián, Spain; [orcid.org/0000-0002-6647-1353](https://orcid.org/0000-0002-6647-1353)
- Xiaowei Ma** – National Center for Nanoscience and Technology (NCNST), 100190 Beijing, China
- Andres Machicote** – Department of Radiotherapy and Radiation Oncology, University Medical Center Hamburg-Eppendorf, 20246 Hamburg, Germany
- Wolfgang Maison** – Mathematics, Informatics, and Natural Sciences (MIN) Faculty, University of Hamburg, 20354 Hamburg, Germany; [orcid.org/0000-0003-2793-5722](https://orcid.org/0000-0003-2793-5722)
- Adrian P. Mancuso** – European XFEL, 22869 Schenefeld, Germany; Department of Chemistry and Physics, La Trobe Institute for Molecular Science, La Trobe University, Melbourne 3086, Victoria, Australia
- Saad Megahed** – Mathematics, Informatics, and Natural Sciences (MIN) Faculty, University of Hamburg, 20354 Hamburg, Germany
- Bert Nickel** – Sektion Physik, Ludwig Maximilians Universität München, 80539 München, Germany; [orcid.org/0000-0002-0254-8841](https://orcid.org/0000-0002-0254-8841)
- Ferdinand Otto** – Mathematics, Informatics, and Natural Sciences (MIN) Faculty, University of Hamburg, 20354 Hamburg, Germany
- Cristina Palencia** – Mathematics, Informatics, and Natural Sciences (MIN) Faculty, University of Hamburg, 20354 Hamburg, Germany; [orcid.org/0000-0002-3505-6376](https://orcid.org/0000-0002-3505-6376)
- Sakura Pascarelli** – European XFEL, 22869 Schenefeld, Germany
- Arwen Pearson** – Mathematics, Informatics, and Natural Sciences (MIN) Faculty, University of Hamburg, 20354 Hamburg, Germany
- Oula Peñate-Medina** – Section Biomedical Imaging, Department of Radiology and Neuroradiology, University Medical Clinic Schleswig-Holstein and Christian-Albrechts-University Kiel, 24105 Kiel, Germany; [orcid.org/0000-0001-9878-5309](https://orcid.org/0000-0001-9878-5309)
- Bing Qi** – Mathematics, Informatics, and Natural Sciences (MIN) Faculty, University of Hamburg, 20354 Hamburg, Germany
- Joachim Rädler** – Sektion Physik, Ludwig Maximilians Universität München, 80539 München, Germany
- Joseph J. Richardson** – ARC Centre of Excellence in Convergent Bio-Nano Science and Technology and the Department of Chemical Engineering, The University of Melbourne, Parkville, Victoria 3010, Australia; [orcid.org/0000-0001-8618-4127](https://orcid.org/0000-0001-8618-4127)
- Axel Rosenhahn** – Department of Radiotherapy and Radiation Oncology, University Medical Center Hamburg-Eppendorf, 20246 Hamburg, Germany; [orcid.org/0000-0001-9393-7190](https://orcid.org/0000-0001-9393-7190)
- Kai Rothkamm** – Department of Radiotherapy and Radiation Oncology, University Medical Center Hamburg-Eppendorf, 20246 Hamburg, Germany; [orcid.org/0000-0001-7414-5729](https://orcid.org/0000-0001-7414-5729)
- Michael Rübhausen** – Mathematics, Informatics, and Natural Sciences (MIN) Faculty, University of Hamburg, 20354 Hamburg, Germany
- Milan K. Sanyal** – Saha Institute of Nuclear Physics, Kolkata 700064, India
- Raymond E. Schaak** – Department of Chemistry, Department of Chemical Engineering, and Materials Research Institute, The Pennsylvania State University, University Park, Pennsylvania 16802, United States; [orcid.org/0000-0002-7468-8181](https://orcid.org/0000-0002-7468-8181)
- Heinz-Peter Schlemmer** – Department of Radiology, German Cancer Research Center (DKFZ), 69120 Heidelberg, Germany
- Marius Schmidt** – Department of Physics, University of Wisconsin-Milwaukee, Milwaukee, Wisconsin 53211, United States; [orcid.org/0000-0002-0962-9468](https://orcid.org/0000-0002-0962-9468)
- Oliver Schmutzler** – Mathematics, Informatics, and Natural Sciences (MIN) Faculty, University of Hamburg, 20354 Hamburg, Germany; Universität Hamburg and Center for Free-Electron Laser Science, 22761 Hamburg, Germany
- Theo Schotten** – CAN, Fraunhofer Institut, 20146 Hamburg, Germany
- Florian Schulz** – Mathematics, Informatics, and Natural Sciences (MIN) Faculty, University of Hamburg, 20354 Hamburg, Germany
- A. K. Sood** – Department of Physics, Indian Institute of Science, Bangalore 560012, India; [orcid.org/0000-0002-4157-361X](https://orcid.org/0000-0002-4157-361X)
- Kathryn M. Spiers** – Deutsches Elektronen-Synchrotron DESY, 22607 Hamburg, Germany
- Theresa Stauffer** – Mathematics, Informatics, and Natural Sciences (MIN) Faculty, University of Hamburg, 20354 Hamburg, Germany; Universität Hamburg and Center for Free-Electron Laser Science, 22761 Hamburg, Germany
- Dominik M. Stemer** – California NanoSystems Institute and Department of Materials Science and Engineering, University of California, Los Angeles, Los Angeles, California 90095, United States; [orcid.org/0000-0002-5528-1773](https://orcid.org/0000-0002-5528-1773)
- Andreas Stierle** – Mathematics, Informatics, and Natural Sciences (MIN) Faculty, University of Hamburg, 20354 Hamburg, Germany; Deutsches Elektronen-Synchrotron DESY, 22607 Hamburg, Germany; [orcid.org/0000-0002-0303-6282](https://orcid.org/0000-0002-0303-6282)
- Xing Sun** – Mathematics, Informatics, and Natural Sciences (MIN) Faculty, University of Hamburg, 20354 Hamburg, Germany; Molecular Science and Biomedicine Laboratory (MBL) State Key Laboratory of Chemo/Biosensing and Chemometrics College of Chemistry and Chemical Engineering, Hunan University, Changsha 410082, P.R. China
- Gohar Tsakanova** – Institute of Molecular Biology of National Academy of Sciences of Republic of Armenia, 0014 Yerevan, Armenia; CANDLE Synchrotron Research Institute, 0040 Yerevan, Armenia
- Paul S. Weiss** – California NanoSystems Institute, Department of Chemistry and Biochemistry, Department of Bioengineering, and Department of Materials Science and Engineering, University of California, Los Angeles, Los Angeles, California 90095, United States; [orcid.org/0000-0001-9393-7190](https://orcid.org/0000-0001-9393-7190)

Angeles, California 90095, United States; [orcid.org/0000-0001-5527-6248](https://orcid.org/0000-0001-5527-6248)

**Horst Weller** – Mathematics, Informatics, and Natural Sciences (MIN) Faculty, University of Hamburg, 20354 Hamburg, Germany; CAN, Fraunhofer Institut, 20146 Hamburg, Germany; [orcid.org/0000-0003-2967-6955](https://orcid.org/0000-0003-2967-6955)

**Fabian Westermeier** – Deutsches Elektronen-Synchrotron DESY, 22607 Hamburg, Germany

**Ming Xu** – State Key Laboratory of Environmental Chemistry and Ecotoxicology, Research Center for Eco-Environmental Sciences, Chinese Academy of Sciences, Beijing 100085, China; [orcid.org/0000-0002-4499-6116](https://orcid.org/0000-0002-4499-6116)

**Huijie Yan** – Mathematics, Informatics, and Natural Sciences (MIN) Faculty, University of Hamburg, 20354 Hamburg, Germany

**Yuan Zeng** – Mathematics, Informatics, and Natural Sciences (MIN) Faculty, University of Hamburg, 20354 Hamburg, Germany

**Ying Zhao** – Karolinska University Hospital, Huddinge, and Karolinska Institutet, 17177 Stockholm, Sweden

**Yuliang Zhao** – National Center for Nanoscience and Technology (NCNST), 100190 Beijing, China; [orcid.org/0000-0002-9586-9360](https://orcid.org/0000-0002-9586-9360)

**Dingcheng Zhu** – Mathematics, Informatics, and Natural Sciences (MIN) Faculty, University of Hamburg, 20354 Hamburg, Germany; [orcid.org/0000-0002-5636-4976](https://orcid.org/0000-0002-5636-4976)

**Ying Zhu** – Bioimaging Center, Shanghai Synchrotron Radiation Facility, Zhangjiang Laboratory, Shanghai Advanced Research Institute, Chinese Academy of Sciences, Shanghai 201210, China; Division of Physical Biology, CAS Key Laboratory of Interfacial Physics and Technology, Shanghai Institute of Applied Physics, Chinese Academy of Sciences, Shanghai 201800, China; [orcid.org/0000-0003-0418-919X](https://orcid.org/0000-0003-0418-919X)

Complete contact information is available at: <https://pubs.acs.org/10.1021/acsnano.0c09563>

## Notes

The authors declare no competing financial interest.

## ACKNOWLEDGMENTS

Parts of this work were supported by the Cluster of Excellence 'Advanced Imaging of Matter' of the Deutsche Forschungsgemeinschaft (DFG) - EXC 2056 - project ID 390715994. Part of this work was performed under the Maria de Maeztu Units of Excellence Programme - grant no. MDM-2017-0720 Ministry of Science, Innovation and Universities. C.S.C. thanks Gipuzkoa Foru Aldundia (Gipuzkoa Fellows program; grant no. 2019-FELL-000018-01/62/2019) for financial support. R.A.A.P. acknowledges the Ministerio de Economía y Competitividad (CTQ2017-88648R), the Generalitat de Catalunya (2017SGR883), and the Universitat Rovira i Virgili (2019PFR-URV-B2-02) for financial support. F.C. acknowledges the award of a National Health and Medical Research Council Senior Principal Research Fellowship (GNT1135806) and support from the Australian Research Council Centre of Excellence in Convergent Bio-Nano Science and Technology (project no. CE140100036). F.G., C.K., Y.L., and O.S. acknowledge DESY (Hamburg, Germany), a member of the Helmholtz Association HGF, for the provision of experimental facilities. Parts of this research

were carried out at PETRA III, and we would like to thank the beamline team for assistance in using P21.1. C.F. and Y.Z. thank the National Key R&D Program of China (2016YFA0400900) for financial support. Y.Z. also acknowledges the Key Research Program of Frontier Sciences (QYZDJ-SSW-SLH031) and the LU Jiaxi International Team of the Chinese Academy of Sciences. Y.H., Y.K., Y.L., Z.L., B.Q., X.S., and H.Y. acknowledge the Chinese Scholarship Council for funding. N.K. thanks the Alexander von Humboldt Foundation for a Visiting Professorship. L.M.L.-M. acknowledges funding by the European Research Council (ERC AdG 4DbioSERS, no. 787510). A.K.S. and M.K.S. thank the Department of Science and Technology, India, for support. K.R. acknowledges support by BMBF grant nos. 02NUK032 and 02NUK035B. D.M.S. and P.S.W. thank the U.S. National Science Foundation, grant no. CHE-2004238, for support. Part of the phytochrome work is supported by BioXFEL STC grant no. NSF-1231306.

## DEDICATION

This article is dedicated to our co-author, colleague, and friend Dr. Theo Schotten, who sadly passed away the day the galley proofs of our article were received, and who will be sadly missed.

## VOCABULARY

**Synchrotron radiation**, electromagnetic radiation emitted by electrons (or other charged particles) traveling at near the speed of light when their direction is altered by an external magnetic field; **synchrotron brilliance**, indicates the quality of a synchrotron source and can be defined as the number of photons within a bandwidth of 0.1% of the central wavelength with the same angular divergence found per unit area of the beam every second; **synchrotron emittance**, average distribution of the relative position and momentum of the electron beam of the synchrotron. Low synchrotron emittances normally lead to smaller X-ray beams and higher brilliance; **diffraction limited storage ring**, a synchrotron storage ring that maintains an electron beam with similar or lower emittance than the smaller X-ray photon beam that it produces; **coherent X-rays**, X-ray radiation with a fixed relationship between their properties, normally referred to as X-rays with a constant difference between their phases; **collimated X-ray beam**, X-ray beam with high spatial coherence. This means that its photons follow parallel or almost parallel trajectories and will not get dispersed with distance; **free electron laser**, fourth-generation synchrotron radiation sources that produce short pulses of highly coherent and extremely brilliant radiation.

## REFERENCES

- (1) Holding, J. D.; Lindup, W. E.; Laer, C. v.; Vreeburg, G. C.; Schilling, V.; Wilson, J. A.; Stell, P. M. Phase I Trial of a Cisplatin-Albumin Complex for the Treatment of Cancer of the Head and Neck. *Br. J. Clin. Pharmacol.* **1992**, *33*, 75–81.
- (2) Hawkins, M. J.; Soon-Shiong, P.; Desai, N. Protein Nano-particles as Drug Carriers in Clinical Medicine. *Adv. Drug Delivery Rev.* **2008**, *60*, 876–885.
- (3) Barenholz, Y. Doxil® — The First FDA-Approved Nano-Drug: Lessons Learned. *J. Controlled Release* **2012**, *160*, 117–134.
- (4) Abrantes, C. G.; Duarte, D.; Reis, C. P. An Overview of Pharmaceutical Excipients: Safe or Not Safe? *J. Pharm. Sci.* **2016**, *105*, 2019–2026.

- (5) Junghanns, J.-U. A. H.; Müller, R. H. Nanocrystal Technology, Drug Delivery and Clinical Applications. *Int. J. Nanomed.* **2008**, *3*, 295–309.
- (6) Limaye, V.; Fortwengel, G.; Limaye, D. Regulatory Roadmap for Nanotechnology Based Medicines. *Int. J. Drug Regul. Aff.* **2014**, *2*, 33–41.
- (7) Roy, S.; Liu, Z.; Sun, X.; Gharib, M.; Yan, H.; Huang, Y.; Megahed, S.; Schnabel, M.; Zhu, D.; Feliu, N.; Chakraborty, I.; Sanchez-Cano, C.; Alkilany, A. M.; Parak, W. J. Assembly and Degradation of Inorganic Nanoparticles in Biological Environments. *Bioconjugate Chem.* **2019**, *30*, 2751–2762.
- (8) Pelaz, B.; Alexiou, C.; Alvarez-Puebla, R. A. A.; Alves, F.; Andrews, A. M.; Ashraf, S.; Balogh, L. P.; Ballerini, L.; Bestetti, A.; Brendel, C.; Bosi, S.; Carril, M.; Chan, W. C. W.; Chen, C.; Chen, X.; Chen, X.; Cheng, Z.; Cui, D.; Du, J.; Dullin, C.; et al. Diverse Applications of Nanomedicine. *ACS Nano* **2017**, *11*, 2313–2381.
- (9) Feliu, N.; Docter, D.; Heine, M.; Del Pino, P.; Ashraf, S.; Kolosnjaj-Tabi, J.; Macchiarelli, P.; Nielsen, P.; Alloyeau, D.; Gazeau, F.; Stauber, R. H.; Parak, W. J. *In Vivo* Degeneration and the Fate of Inorganic Nanoparticles. *Chem. Soc. Rev.* **2016**, *45*, 2440–2457.
- (10) Rosenblum, D.; Joshi, N.; Tao, W.; Karp, J. M.; Peer, D. Progress and Challenges towards Targeted Delivery of Cancer Therapeutics. *Nat. Commun.* **2018**, *9*, 1410.
- (11) Narum, S. M.; Le, T.; Le, D. P.; Lee, J. C.; Donahue, N. D.; Yang, W.; Wilhelm, S. Chapter 4 - Passive Targeting in Nanomedicine: Fundamental Concepts, Body Interactions, and Clinical Potential. In *Nanoparticles for Biomedical Applications*; Chung, E. J., Leon, L., Rinaldi, C., Eds.; Elsevier: Amsterdam, The Netherlands, 2020; pp 37–53.
- (12) Salvati, A.; Pitek, A. S.; Monopoli, M. P.; Prapainop, K.; Bombelli, F. B.; Hristov, D. R.; Kelly, P. M.; Aberg, C.; Mahon, E.; Dawson, K. A. Transferrin-Functionalized Nanoparticles Lose Their Targeting Capabilities When a Biomolecule Corona Adsorbs on the Surface. *Nat. Nanotechnol.* **2013**, *8*, 137–143.
- (13) Colombo, M.; Fiandra, L.; Alessio, G.; Mazzucchelli, S.; Nebuloni, M.; De Palma, C.; Kantner, K.; Pelaz, B.; Rotem, R.; Corsi, F.; Parak, W. J.; Prosperi, D. Tumour Homing and Therapeutic Effect of Colloidal Nanoparticles Depend on the Number of Attached Antibodies. *Nat. Commun.* **2016**, *7*, 13818.
- (14) Fasting, C.; Schalley, C. A.; Weber, M.; Seitz, O.; Hecht, S.; Kokschi, B.; Dervede, J.; Graf, C.; Knapp, E.-W.; Haag, R. Multivalency as a Chemical Organization and Action Principle. *Angew. Chem., Int. Ed.* **2012**, *51*, 10472–10498.
- (15) Kreyling, W. G.; Abdelmonem, A. M.; Ali, Z.; Alves, F.; Geiser, M.; Haberl, N.; Hartmann, R.; Hirn, S.; de Aberasturi, D. J.; Kantner, K.; Khadem-Saba, G.; Montenegro, J. M.; Rejman, J.; Rojo, T.; de Larramendi, I. R.; Ufartes, R.; Wenk, A.; Parak, W. J. *In Vivo* Integrity of Polymer-Coated Gold Nanoparticles. *Nat. Nanotechnol.* **2015**, *10*, 619–623.
- (16) Bruinink, A.; Wang, J.; Wick, P. Effect of Particle Agglomeration in Nanotoxicology. *Arch. Toxicol.* **2015**, *89*, 659–675.
- (17) Carrillo-Carrion, C.; Bocanegra, A. I.; Arnaiz, B.; Feliu, N.; Zhu, D.; Parak, W. J. Triple-Labeling of Polymer-Coated Quantum Dots and Adsorbed Proteins for Tracing Their Fate in Cell Cultures. *ACS Nano* **2019**, *13*, 4631–4639.
- (18) Guan, S.; Rosenecker, J. Nanotechnologies in Delivery of mRNA Therapeutics Using Nonviral Vector-Based Delivery Systems. *Gene Ther.* **2017**, *24*, 133–143.
- (19) Sharma, V. K.; Siskova, K. M.; Zboril, R.; Gardea-Torresdey, J. L. Organic-Coated Silver Nanoparticles in Biological and Environmental Conditions: Fate, Stability and Toxicity. *Adv. Colloid Interface Sci.* **2014**, *204*, 15–34.
- (20) Jiang, X. M.; Miclaus, T.; Wang, L. M.; Foldbjerg, R.; Sutherland, D. S.; Autrup, H.; Chen, C. Y.; Beer, C. Fast Intracellular Dissolution and Persistent Cellular Uptake of Silver Nanoparticles in CHO-K1 Cells: Implication for Cytotoxicity. *Nanotoxicology* **2015**, *9*, 181–189.
- (21) Manshian, B. B.; Pfeiffer, C.; Pelaz, B.; Heimerl, T.; Gallego, M.; Moller, M.; del Pino, P.; Himmelreich, U.; Parak, W. J.; Soenen, S. J. High-Content Imaging and Gene Expression Approaches to Unravel the Effect of Surface Functionality on Cellular Interactions of Silver Nanoparticles. *ACS Nano* **2015**, *9*, 10431–10444.
- (22) Wang, L. M.; Zhang, T. L.; Li, P. Y.; Huang, W. X.; Tang, J. L.; Wang, P. Y.; Liu, J.; Yuan, Q. X.; Bai, R.; Li, B.; Zhang, K.; Zhao, Y. L.; Chen, C. Y. Use of Synchrotron Radiation-Analytical Techniques to Reveal Chemical Origin of Silver-Nanoparticle Cytotoxicity. *ACS Nano* **2015**, *9*, 6532–6547.
- (23) Veronesi, G.; Aude-Garcia, C.; Kieffer, I.; Gallon, T.; Delangle, P.; Herlin-Boime, N.; Rabilloud, T.; Carrière, M. Exposure-Dependent Ag<sup>+</sup> Release from Silver Nanoparticles and Its Complexation in Ag<sub>2</sub>S Sites in Primary Murine Macrophages. *Nanoscale* **2015**, *7*, 7323–7330.
- (24) Veronesi, G.; Deniaud, A.; Gallon, T.; Jouneau, P.-H.; Villanova, J.; Delangle, P.; Carrière, M.; Kieffer, I.; Charbonnier, P.; Mintz, E.; Michaud-Soret, I. Visualization, Quantification and Coordination of Ag<sup>+</sup> Ions Released from Silver Nanoparticles in Hepatocytes. *Nanoscale* **2016**, *8*, 17012–17021.
- (25) Rejman, J.; Nazareus, M.; Jimenez de Aberasturi, D.; Said, A. H.; Feliu, N.; Parak, W. J. Some Thoughts about the Intracellular Location of Nanoparticles and the Resulting Consequences. *J. Colloid Interface Sci.* **2016**, *482*, 260–266.
- (26) Angelov, B.; Angelova, A.; Mutafchieva, R.; Lesieur, S.; Vainio, U.; Garamus, V. M.; Jensen, G. V.; Pedersen, J. S. SAXS Investigation of a Cubic to a Sponge (L3) Phase Transition in Self-Assembled Lipid Nanocarriers. *Phys. Chem. Chem. Phys.* **2011**, *13*, 3073–3081.
- (27) Mertins, O.; Mathews, P. D.; Angelova, A. Advances in the Design of pH-Sensitive Cubosome Liquid Crystalline Nanocarriers for Drug Delivery Applications. *Nanomaterials* **2020**, *10*, 963.
- (28) Salentinig, S.; Tangso, K. J.; Hawley, A.; Boyd, B. J. pH-Driven Colloidal Transformations Based on the Vasoactive Drug Nicergoline. *Langmuir* **2014**, *30*, 14776–14781.
- (29) Angelov, B.; Angelova, A.; Garamus, V. M.; Drechsler, M.; Willumeit, R.; Mutafchieva, R.; Štěpánek, P.; Lesieur, S. Earliest Stage of the Tetrahedral Nanochannel Formation in Cubosome Particles from Unilamellar Nanovesicles. *Langmuir* **2012**, *28*, 16647–16655.
- (30) Reimhult, E. Nanoparticle-Triggered Release from Lipid Membrane Vesicles. *New Biotechnol.* **2015**, *32*, 665–672.
- (31) Peñate-Medina, O.; Peñate-Medina, T.; Humbert, J.; Qi, B.; Baum, W.; Will, O.; Damm, T.; Glüer, C. Using Alendronic Acid Coupled Fluorescently Labelled SM Liposomes as a Vehicle for Bone Targeting. *Curr. Pharm. Des.* **2020**, *26*, 6021–6027.
- (32) Peñate-Medina, T.; Kraas, E.; Luo, K.; Humbert, J.; Zhu, H.; Mertens, F.; Gerle, M.; Rochweder, A.; Damoah, C.; Will, O.; Acil, Y.; Kairemo, K.; Wiltfang, J.; Glüer, C. C.; Scherließ, R.; Sebens, S.; Peñate-Medina, O. Utilizing ICG Spectroscopic Properties for Real-Time Nanoparticle Release Quantification *In Vitro* and *In Vivo* in Imaging Setups. *Curr. Pharm. Des.* **2020**, *26*, 3828–3833.
- (33) Mi, P. Stimuli-Responsive Nanocarriers for Drug Delivery, Tumor Imaging, Therapy and Theranostics. *Theranostics* **2020**, *10*, 4557–4588.
- (34) Tian, B.; Fernandez-Bravo, A.; Najafaghdam, H.; Torquato, N. A.; Altoe, M. V. P.; Teitelboim, A.; Tajon, C. A.; Tian, Y.; Borys, N. J.; Barnard, E. S.; Anwar, M.; Chan, E. M.; Schuck, P. J.; Cohen, B. E. Low Irradiance Multiphoton Imaging with Alloyed Lanthanide Nanocrystals. *Nat. Commun.* **2018**, *9*, 3082.
- (35) Levy, E. S.; Tajon, C. A.; Bischof, T. S.; Iafrazi, J.; Fernandez-Bravo, A.; Garfield, D. J.; Chamanzar, M.; Maharbiz, M. M.; Sohal, V. S.; Schuck, P. J.; Cohen, B. E.; Chan, E. M. Energy-Looping Nanoparticles: Harnessing Excited-State Absorption for Deep-Tissue Imaging. *ACS Nano* **2016**, *10*, 8423–8433.
- (36) Chien, Y.-H.; Chou, Y.-L.; Wang, S.-W.; Hung, S.-T.; Liau, M.-C.; Chao, Y.-J.; Su, C.-H.; Yeh, C.-S. Near-Infrared Light Photocontrolled Targeting, Bioimaging, and Chemotherapy with Caged Upconversion Nanoparticles *In Vitro* and *In Vivo*. *ACS Nano* **2013**, *7*, 8516–8528.

- (37) Jalani, G.; Tam, V.; Vetrone, F.; Cerruti, M. Seeing, Targeting and Delivering with Upconverting Nanoparticles. *J. Am. Chem. Soc.* **2018**, *140*, 10923–10931.
- (38) Lai, J.; Shah, B. P.; Zhang, Y.; Yang, L.; Lee, K.-B. Real-Time Monitoring of ATP-Responsive Drug Release Using Mesoporous-Silica-Coated Multicolor Upconversion Nanoparticles. *ACS Nano* **2015**, *9*, 5234–5245.
- (39) Nam, S. H.; Bae, Y. M.; Park, Y. I.; Kim, J. H.; Kim, H. M.; Choi, J. S.; Lee, K. T.; Hyeon, T.; Suh, Y. D. Long-Term Real-Time Tracking of Lanthanide Ion Doped Upconverting Nanoparticles in Living Cells. *Angew. Chem., Int. Ed.* **2011**, *50*, 6093–6097.
- (40) Wu, S.; Han, G.; Milliron, D. J.; Aloni, S.; Altoe, V.; Talapin, D. V.; Cohen, B. E.; Schuck, P. J. Non-Blinking and Photostable Upconverted Luminescence from Single Lanthanide-Doped Nanocrystals. *Proc. Natl. Acad. Sci. U. S. A.* **2009**, *106*, 10917–10921.
- (41) Vetrone, F.; Naccache, R.; Zamarron, A.; Juarranz de la Fuente, A.; Sanz-Rodriguez, F.; Martinez Maestro, L.; Martin Rodriguez, E.; Jaque, D.; Garcia Sole, J.; Capobianco, J. A. Temperature Sensing Using Fluorescent Nanothermometers. *ACS Nano* **2010**, *4*, 3254–3258.
- (42) Ortgies, D. H.; Tan, M.; Ximendes, E. C.; del Rosal, B.; Hu, J.; Xu, L.; Wang, X.; Martin Rodriguez, E.; Jacinto, C.; Fernandez, N.; Chen, G.; Jaque, D. Lifetime-Encoded Infrared-Emitting Nanoparticles for *in Vivo* Multiplexed Imaging. *ACS Nano* **2018**, *12*, 4362–4368.
- (43) Lay, A.; Wang, D. S.; Wisser, M. D.; Mehlenbacher, R. D.; Lin, Y.; Goodman, M. B.; Mao, W. L.; Dionne, J. A. Upconverting Nanoparticles as Optical Sensors of Nano- to Micro-Newton Forces. *Nano Lett.* **2017**, *17*, 4172–4177.
- (44) Ma, Y.; Bao, J.; Zhang, Y.; Li, Z.; Zhou, X.; Wan, C.; Huang, L.; Zhao, Y.; Han, G.; Xue, T. Mammalian Near-Infrared Image Vision through Injectable and Self-Powered Retinal Nanoantennae. *Cell* **2019**, *177*, 243–255.
- (45) Chen, S.; Weitemier, A. Z.; Zeng, X.; He, L.; Wang, X.; Tao, Y.; Huang, A. J. Y.; Hashimoto, Y.; Kano, M.; Iwasaki, H.; Parajuli, L. K.; Okabe, S.; Teh, D. B. L.; All, A. H.; Tsutsui-Kimura, I.; Tanaka, K. F.; Liu, X.; McHugh, T. J. Near-Infrared Deep Brain Stimulation *via* Upconversion Nanoparticle Mediated Optogenetics. *Science* **2018**, *359*, 679–684.
- (46) Mann, V. R.; Powers, A. S.; Tilley, D. C.; Sack, J. T.; Cohen, B. E. Azide–Alkyne Click Conjugation on Quantum Dots by Selective Copper Coordination. *ACS Nano* **2018**, *12*, 4469–4477.
- (47) Thal, L. B.; Mann, V. R.; Sprinzen, D.; McBride, J. R.; Reid, K. R.; Tomlinson, I. D.; McMahon, D. G.; Cohen, B. E.; Rosenthal, S. J. Ligand-Conjugated Quantum Dots for Fast Sub-Diffraction Protein Tracking in Acute Brain Slices. *Biomater. Sci.* **2020**, *8*, 837–845.
- (48) Wichner, S. M.; Mann, V. R.; Powers, A. S.; Segal, M. A.; Mir, M.; Bandaria, J. N.; DeWitt, M. A.; Darzacq, X.; Yildiz, A.; Cohen, B. E. Covalent Protein Labeling and Improved Single-Molecule Optical Properties of Aqueous CdSe/CdS Quantum Dots. *ACS Nano* **2017**, *11*, 6773–6781.
- (49) Colombo, M.; Mazzucchelli, S.; Montenegro, J. M.; Galbiati, E.; Corsi, F.; Parak, W. J.; Prosperi, D. Protein Oriented Ligation on Nanoparticles Exploiting O6-Alkylguanine-DNA Transferase (SNAP) Genetically Encoded Fusion. *Small* **2012**, *8*, 1492–1497.
- (50) Alkilany, A. M.; Zhu, L.; Weller, H.; Mews, A.; Parak, W.; Barz, M.; Feliu, N. Ligand Density on Nanoparticles: A Parameter with Critical Impact on Nanomedicine. *Adv. Drug Delivery Rev.* **2019**, *143*, 22–36.
- (51) Kriemen, E.; Holzapfel, M.; Ruf, E.; Rehbein, J.; Maison, W. Synthesis and Structural Analysis of 1,4,7,10-Tetraazacyclododecane-1,4,7,10-Tetraazidoethylacetic Acid (DOTAZA) Complexes. *Eur. J. Inorg. Chem.* **2015**, *2015*, 5368–5378.
- (52) Ali, Z.; Abbasi, A. Z.; Zhang, F.; Arosio, P.; Lascialfari, A.; Casula, M. F.; Wenk, A.; Kreyling, W.; Plapper, R.; Seidel, M.; Niessner, R.; Knoll, J.; Seubert, A.; Parak, W. J. Multifunctional Nanoparticles for Dual Imaging. *Anal. Chem.* **2011**, *83*, 2877–2882.
- (53) Price, E. W.; Orvig, C. Matching Chelators to Radiometals for Radiopharmaceuticals. *Chem. Soc. Rev.* **2014**, *43*, 260–290.
- (54) Holzapfel, M.; Mutas, M.; Chandralingam, S.; von Salisch, C.; Peric, N.; Segelke, T.; Fischer, M.; Chakraborty, I.; Parak, W. J.; Frangioni, J. V.; Maison, W. Nonradioactive Cell Assay for the Evaluation of Modular Prostate-Specific Membrane Antigen Targeting Ligands *via* Inductively Coupled Plasma Mass Spectrometry. *J. Med. Chem.* **2019**, *62*, 10912–10918.
- (55) Wahsner, J.; Gale, E. M.; Rodríguez-Rodríguez, A.; Caravan, P. Chemistry of MRI Contrast Agents: Current Challenges and New Frontiers. *Chem. Rev.* **2019**, *119*, 957–1057.
- (56) He, S.; Song, J.; Qu, J.; Cheng, Z. Crucial Breakthrough of Second Near-Infrared Biological Window Fluorophores: Design and Synthesis toward Multimodal Imaging and Theranostics. *Chem. Soc. Rev.* **2018**, *47*, 4258–4278.
- (57) Grüner, F.; Blumendorf, F.; Schmutzler, O.; Staufer, T.; Bradbury, M.; Wiesner, U.; Rosentreter, T.; Loers, G.; Lutz, D.; Richter, B.; Fischer, M.; Schulz, F.; Steiner, S.; Warmer, M.; Burkhardt, A.; Meents, A.; Kupinski, M.; Hoeschen, C. Localising Functionalised Gold-Nanoparticles in Murine Spinal Cords by X-Ray Fluorescence Imaging and Background-Reduction Through Spatial Filtering for Human-Sized Objects. *Sci. Rep.* **2018**, *8*, 16561.
- (58) Avery, R. K.; Albadawi, H.; Akbari, M.; Zhang, Y. S.; Duggan, M. J.; Sahani, D. V.; Olsen, B. D.; Khademhosseini, A.; Oklu, R. An Injectable Shear-Thinning Biomaterial for Endovascular Embolization. *Sci. Transl. Med.* **2016**, *8*, No. 365ra156.
- (59) Carrillo-Carrion, C.; Carril, M.; Parak, W. J. Techniques for the Experimental Investigation of the Protein Corona. *Curr. Opin. Biotechnol.* **2017**, *46*, 106–113.
- (60) Witzler, M.; Küllmer, F.; Günther, K. Validating a Single-Particle ICP-MS Method to Measure Nanoparticles in Human Whole Blood for Nanotoxicology. *Anal. Lett.* **2018**, *51*, 587–599.
- (61) Wang, W.-Y.; Yao, C.; Shao, Y.-F.; Mu, H.-J.; Sun, K.-X. Determination of Puerarin in Rabbit Aqueous Humor by Liquid Chromatography Tandem Mass Spectrometry Using Microdialysis Sampling after Topical Administration of Puerarin PAMAM Dendrimer Complex. *J. Pharm. Biomed. Anal.* **2011**, *56*, 825–829.
- (62) Epemolu, O.; Mayer, I.; Hope, F.; Scullion, P.; Desmond, P. Liquid Chromatography/Mass Spectrometric Bioanalysis of a Modified  $\gamma$ -Cyclodextrin (Org 25969) and Rocuronium Bromide (Org 9426) in Guinea Pig Plasma and Urine: Its Application to Determine the Plasma Pharmacokinetics of Org 25969. *Rapid Commun. Mass Spectrom.* **2002**, *16*, 1946–1952.
- (63) Liu, Z.; Escudero, A.; Carrillo-Carrion, C.; Chakraborty, I.; Zhu, D.; Gallego, M.; Parak, W. J.; Feliu, N. Biodegradation of Bi-Labeled Polymer-Coated Rare-Earth Nanoparticles in Adherent Cell Cultures. *Chem. Mater.* **2020**, *32*, 245–254.
- (64) Gowda, G. A. N.; Djukovic, D. Overview of Mass Spectrometry-Based Metabolomics: Opportunities and Challenges. In *Mass Spectrometry in Metabolomics: Methods and Protocols*; Raftery, D., Ed.; Springer: New York, 2014; pp 3–12.
- (65) Talamini, L.; Violatto, M. B.; Cai, Q.; Monopoli, M. P.; Kantner, K.; Krpetić, Z. e.; Perez-Potti, A.; Cookman, J.; Garry, D.; Silveira, C. P.; Boselli, L.; Pelaz, B.; Serchi, T.; Cambier, S. b.; Gutleb, A. C.; Feliu, N.; Yan, Y.; Salmona, M.; Parak, W. J.; Dawson, K. A.; Bigini, P. Influence of Size and Shape on the Anatomical Distribution of Endotoxin-Free Gold Nanoparticles. *ACS Nano* **2017**, *11*, 5519–5529.
- (66) Xu, M.; Soliman, M. G.; Sun, X.; Pelaz, B.; Feliu, N.; Parak, W. J.; Liu, S. How Entanglement of Different Physicochemical Properties Complicates the Prediction of *in Vitro* and *in Vivo* Interactions of Gold Nanoparticles. *ACS Nano* **2018**, *12*, 10104–10113.
- (67) Amini-Nik, S.; Kraemer, D.; Cowan, M. L.; Gunaratne, K.; Nadesan, P.; Alman, B. A.; Miller, R. J. Ultrafast Mid-IR Laser Scalpel: Protein Signals of the Fundamental Limits to Minimally Invasive Surgery. *PLoS One* **2010**, *5*, e13053.
- (68) Kwiatkowski, M.; Wurlitzer, M.; Krutilin, A.; Kiani, P.; Nimer, R.; Omid, M.; Mannaa, A.; Bussmann, T.; Bartkowiak, K.; Kruber,

- S.; Uschold, S.; Steffen, P.; Lubberstedt, J.; Kupker, N.; Petersen, H.; Knecht, R.; Hansen, N. O.; Zarrine-Afsar, A.; Robertson, W. D.; Miller, R. J. D.; Schluter, H. Homogenization of Tissues via Picosecond-Infrared Laser (PIRL) Ablation: Giving a Closer View on the *in-Vivo* Composition of Protein Species as Compared to Mechanical Homogenization. *J. Proteomics* **2016**, *134*, 193–202.
- (69) Rompp, A.; Guenther, S.; Takats, Z.; Spengler, B. Mass Spectrometry Imaging with High Resolution in Mass and Space (HR(2) MSI) for Reliable Investigation of Drug Compound Distributions on the Cellular Level. *Anal. Bioanal. Chem.* **2011**, *401*, 65–73.
- (70) Abramowski, P.; Kraus, O.; Rohn, S.; Riecken, K.; Fehse, B.; Schluter, H. Combined Application of RGB Marking and Mass Spectrometric Imaging Facilitates Detection of Tumor Heterogeneity. *Cancer Genomics Proteomics* **2015**, *12*, 179–187.
- (71) Cui, Y.; Cao, W.; He, Y.; Zhao, Q.; Wakazaki, M.; Zhuang, X.; Gao, J.; Zeng, Y.; Gao, C.; Ding, Y.; Wong, H. Y.; Wong, W. S.; Lam, H. K.; Wang, P.; Ueda, T.; Rojas-Pierce, M.; Toyooka, K.; Kang, B.-H.; Jiang, L. A Whole-Cell Electron Tomography Model of Vacuole Biogenesis in *Arabidopsis* Root Cells. *Nat. Plants* **2019**, *5*, 95–105.
- (72) Zachs, T.; Schertel, A.; Medeiros, J.; Weiss, G. L.; Hugener, J.; Matos, J.; Pilhofer, M. Fully Automated, Sequential Focused Ion Beam Milling for Cryo-Electron Tomography. *eLife* **2020**, *9*, No. e52286.
- (73) Lučić, V.; Rigort, A.; Baumeister, W. Cryo-Electron Tomography: The Challenge of Doing Structural Biology *in Situ*. *J. Cell Biol.* **2013**, *202*, 407–419.
- (74) Wu, H.; Friedrich, H.; Patterson, J. P.; Sommerdijk, N. A. J. M.; de Jonge, N. Liquid-Phase Electron Microscopy for Soft Matter Science and Biology. *Adv. Mater.* **2020**, *32*, 2001582.
- (75) Koo, K.; Dae, K. S.; Hahn, Y. K.; Yuk, J. M. Live Cell Electron Microscopy Using Graphene Veils. *Nano Lett.* **2020**, *20*, 4708–4713.
- (76) Kennedy, E.; Nelson, E. M.; Damiano, J.; Timp, G. Gene Expression in Electron-Beam-Irradiated Bacteria in Reply to “Live Cell Electron Microscopy Is Probably Impossible. *ACS Nano* **2017**, *11*, 3–7.
- (77) de Jonge, N.; Peckys, D. B. Live Cell Electron Microscopy Is Probably Impossible. *ACS Nano* **2016**, *10*, 9061–9063.
- (78) Key, J.; Leary, J. F. Nanoparticles for Multimodal *in Vivo* Imaging in Nanomedicine. *Int. J. Nanomed.* **2014**, *9*, 711–726.
- (79) Leary, J. F. Design of Sophisticated Shaped, Multilayered, and Multifunctional Nanoparticles for Combined *in-Vivo* Imaging and Advanced Drug Delivery. *Proc. SPIE* **2019**, *10891*, 108910R.
- (80) van Schadowijk, R.; Krug, J. R.; Shen, D.; Sankar Gupta, K. B. S.; Vergeldt, F. J.; Bisseling, T.; Webb, A. G.; Van As, H.; Velders, A. H.; de Groot, H. J. M.; Alia, A. Magnetic Resonance Microscopy at Cellular Resolution and Localised Spectroscopy of *Medicago truncatula* at 22.3 T. *Sci. Rep.* **2020**, *10*, 971.
- (81) Lee, C. H.; Bengtsson, N.; Chrzanowski, S. M.; Flint, J. J.; Walter, G. A.; Blackband, S. J. Magnetic Resonance Microscopy (MRM) of Single Mammalian Myofibers and Myonuclei. *Sci. Rep.* **2017**, *7*, 39496.
- (82) Lee, C. H.; Flint, J. J.; Hansen, B.; Blackband, S. J. Investigation of the Subcellular Architecture of L7 Neurons of *Aplysia californica* Using Magnetic Resonance Microscopy (MRM) at 7.8 Microns. *Sci. Rep.* **2015**, *5*, 11147.
- (83) Li, T.; Zhou, J.; Wang, L.; Zhang, H.; Song, C.; de la Fuente, J. M.; Pan, Y.; Song, J.; Zhang, C.; Cui, D. Photo-Fenton-Like Metal-Protein Self-Assemblies as Multifunctional Tumor Therapeutic Agent. *Adv. Healthcare Mater.* **2019**, *8*, 1900192.
- (84) Liu, Y.; Pan, Y.; Cao, W.; Xia, F.; Liu, B.; Niu, J.; Alfranca, G.; Sun, X.; Ma, L.; Fuente, J. M. d. l.; Song, J.; Ni, J.; Cui, D. A Tumor Microenvironment Responsive Biodegradable CaCO<sub>3</sub>/MnO<sub>2</sub>-Based Nanoplatform for the Enhanced Photodynamic Therapy and Improved PD-L1 Immunotherapy. *Theranostics* **2019**, *9*, 6867–6884.
- (85) Ding, B.; Zheng, P.; Ma, P. a.; Lin, J. Manganese Oxide Nanomaterials: Synthesis, Properties, and Theranostic Applications. *Adv. Mater.* **2020**, *32*, 1905823.
- (86) Shen, Z.; Chen, T.; Ma, X.; Ren, W.; Zhou, Z.; Zhu, G.; Zhang, A.; Liu, Y.; Song, J.; Li, Z.; Ruan, H.; Fan, W.; Lin, L.; Munasinghe, J.; Chen, X.; Wu, A. Multifunctional Theranostic Nanoparticles Based on Exceedingly Small Magnetic Iron Oxide Nanoparticles for T1-Weighted Magnetic Resonance Imaging and Chemotherapy. *ACS Nano* **2017**, *11*, 10992–11004.
- (87) Tassa, C.; Shaw, S. Y.; Weissleder, R. Dextran-Coated Iron Oxide Nanoparticles: A Versatile Platform for Targeted Molecular Imaging, Molecular Diagnostics, and Therapy. *Acc. Chem. Res.* **2011**, *44*, 842–852.
- (88) Ladd, M. E.; Bachert, P.; Meyerspeer, M.; Moser, E.; Nagel, A. M.; Norris, D. G.; Schmitter, S.; Speck, O.; Straub, S.; Zaiss, M. Pros and Cons of Ultra-High-Field MRI/MRS for Human Application. *Prog. Nucl. Magn. Reson. Spectrosc.* **2018**, *109*, 1–50.
- (89) Zhang, F.; Ali, Z.; Amin, F.; Feltz, A.; Oheim, M.; Parak, W. J. Ion and pH Sensing with Colloidal Nanoparticles: Influence of Surface Charge on Sensing and Colloidal Properties. *ChemPhysChem* **2010**, *11*, 730–735.
- (90) Lay, A.; Sheppard, O. H.; Siefe, C.; McLellan, C. A.; Mehlenbacher, R. D.; Fischer, S.; Goodman, M. B.; Dionne, J. A. Optically Robust and Biocompatible Mechanosensitive Upconverting Nanoparticles. *ACS Cent. Sci.* **2019**, *5*, 1211–1222.
- (91) Mehlenbacher, R. D.; Kolbl, R.; Lay, A.; Dionne, J. A. Nanomaterials for *in Vivo* Imaging of Mechanical Forces and Electrical Fields. *Nature Rev. Mater.* **2018**, *3*, 17080.
- (92) Rasmussen, J. C.; Tan, I. C.; Marshall, M. V.; Fife, C. E.; Sevick-Muraca, E. M. Lymphatic Imaging in Humans with Near-Infrared Fluorescence. *Curr. Opin. Biotechnol.* **2009**, *20*, 74–82.
- (93) Song, C.; Li, Y.; Li, T.; Yang, Y.; Huang, Z.; de la Fuente, J. M.; Ni, J.; Cui, D. Long-Circulating Drug-Dye-Based Micelles with Ultrahigh pH-Sensitivity for Deep Tumor Penetration and Superior Chemo-Photothermal Therapy. *Adv. Funct. Mater.* **2020**, *30*, 1906309.
- (94) Pan, S.; Pei, L.; Zhang, A.; Zhang, Y.; Zhang, C.; Huang, M.; Huang, Z.; Liu, B.; Wang, L.; Ma, L.; Zhang, Q.; Cui, D. Passion Fruit-Like Exosome-PMA/Au-BSA@Ce6 Nanovehicles for Real-Time Fluorescence Imaging and Enhanced Targeted Photodynamic Therapy with Deep Penetration and Superior Retention Behavior in Tumor. *Biomaterials* **2020**, *230*, 119606.
- (95) Zhang, A.; Pan, S.; Zhang, Y.; Chang, J.; Cheng, J.; Huang, Z.; Li, T.; Zhang, C.; Fuente, J. M. d. l.; Zhang, Q.; Cui, D. Carbon-Gold Hybrid Nanoparticles for Real-Time Imaging, Photothermal/Photodynamic and Nanozyme Oxidative Therapy. *Theranostics* **2019**, *9*, 3443–3458.
- (96) Sudheendra, L.; Das, G. K.; Li, C.; Stark, D.; Cena, J.; Cherry, S.; Kennedy, I. M. NaGdF<sub>4</sub>:Eu<sup>3+</sup> Nanoparticles for Enhanced X-Ray Excited Optical Imaging. *Chem. Mater.* **2014**, *26*, 1881–1888.
- (97) Hsu, C.-C.; Lin, S.-L.; Chang, C. A. Lanthanide-Doped Core-Shell-Shell Nanocomposite for Dual Photodynamic Therapy and Luminescence Imaging by a Single X-Ray Excitation Source. *ACS Appl. Mater. Interfaces* **2018**, *10*, 7859–7870.
- (98) Ma, J.; Huang, P.; He, M.; Pan, L.; Zhou, Z.; Feng, L.; Gao, G.; Cui, D. Folic Acid-Conjugated LaF<sub>3</sub>:Yb,Tm@SiO<sub>2</sub> Nanoparticles for Targeting Dual-Modality Imaging of Upconversion Luminescence and X-Ray Computed Tomography. *J. Phys. Chem. B* **2012**, *116*, 14062–14070.
- (99) Pujals, S.; Feiner-Gracia, N.; Delcanale, P.; Voets, I.; Albertazzi, L. Super-Resolution Microscopy as a Powerful Tool to Study Complex Synthetic Materials. *Nat. Rev. Chem.* **2019**, *3*, 68–84.
- (100) Möckl, L.; Lamb, D. C.; Bräuchle, C. Super-Resolved Fluorescence Microscopy: Nobel Prize in Chemistry 2014 for Eric Betzig, Stefan Hell, and William E. Moerner. *Angew. Chem., Int. Ed.* **2014**, *53*, 13972–13977.

- (101) Schermelleh, L.; Heintzmann, R.; Leonhardt, H. A Guide to Super-Resolution Fluorescence Microscopy. *J. Cell Biol.* **2010**, *190*, 165–175.
- (102) Huang, B.; Bates, M.; Zhuang, X. Super-Resolution Fluorescence Microscopy. *Annu. Rev. Biochem.* **2009**, *78*, 993–1016.
- (103) Ma, X.; Hartmann, R.; Jimenez de Aberasturi, D.; Yang, F.; Soenen, S. J. H.; Manshian, B. B.; Franz, J.; Valdeperez, D.; Pelaz, B.; Feliu, N.; Hampp, N.; Riethmuller, C.; Vieker, H.; Frese, N.; Golzhauser, A.; Simonich, M.; Tanguay, R. L.; Liang, X.-J.; Parak, W. J. Colloidal Gold Nanoparticles Induce Changes in Cellular and Subcellular Morphology. *ACS Nano* **2017**, *11*, 7807–7820.
- (104) Itano, M. S.; Neumann, A. K.; Liu, P.; Zhang, F.; Gratton, E.; Parak, W. J.; Thompson, N. L.; Jacobson, K. DC-SIGN and Influenza Hemagglutinin Dynamics in Plasma Membrane Microdomains are Markedly Different. *Biophys. J.* **2011**, *100*, 2662–2670.
- (105) Smith, A. M.; Mancini, M. C.; Nie, S. M. BIOIMAGING Second Window for *in Vivo* Imaging. *Nat. Nanotechnol.* **2009**, *4*, 710–711.
- (106) Dong, N.-N.; Pedroni, M.; Piccinelli, F.; Conti, G.; Sbarbati, A.; Ramirez-Hernandez, J. E.; Maestro, L. M.; Iglesias-De La Cruz, M. C.; Sanz-Rodriguez, F.; Juarranz, A.; Chen, F.; Vetrone, F.; Capobianco, J. A.; Sole, J. G.; Bettinelli, M.; Jaque, D.; Speghini, A. NIR-to-NIR Two-Photon Excited  $\text{CaF}_2:\text{Tm}^{3+}, \text{Yb}^{3+}$  Nanoparticles: Multifunctional Nanoprobes for Highly Penetrating Fluorescence Bio-Imaging. *ACS Nano* **2011**, *5*, 8665.
- (107) Lopez, M. J.; Seyed-Razavi, Y.; Yamaguchi, T.; Ortiz, G.; Sendra, V. G.; Harris, D. L.; Jamali, A.; Hamrah, P. Multiphoton Intravital Microscopy of Mandibular Draining Lymph Nodes: A Mouse Model to Study Corneal Immune Responses. *Front. Immunol.* **2020**, *11*, 39.
- (108) Ishii, M. Intravital Imaging Technology Reveals Immune System Dynamics *in Vivo*. *Allergol. Int.* **2016**, *65*, 225–227.
- (109) Pittet, M. J.; Garris, C. S.; Arlauckas, S. P.; Weissleder, R. Recording the Wild Lives of Immune Cells. *Sci. Immunol.* **2018**, *3*, No. eaaq0491.
- (110) Witte, M.; Jaspers, S.; Wenck, H.; Rübhausen, M.; Fischer, F. Noise Reduction and Quantification of Fiber Orientations in Greyscale Images. *PLoS One* **2020**, *15*, e0227534.
- (111) Mellem, D.; Sattler, M.; Pagel-Wolff, S.; Jaspers, S.; Wenck, H.; Rübhausen, M. A.; Fischer, F. Fragmentation of the Mitochondrial Network in Skin *in Vivo*. *PLoS One* **2017**, *12*, e0174469.
- (112) Huser, T.; Chan, J. Raman Spectroscopy for Physiological Investigations of Tissues and Cells. *Adv. Drug Delivery Rev.* **2015**, *89*, 57–70.
- (113) Langer, J.; Jimenez de Aberasturi, D.; Aizpurua, J.; Alvarez-Puebla, R. A.; Auguie, B.; Baumberg, J. J.; Bazan, G. C.; Bell, S. E. J.; Boisen, A.; Brolo, A. G.; Choo, J.; Cialla-May, D.; Deckert, V.; Fabris, L.; Faulds, K.; Garcia de Abajo, F. J.; Goodacre, R.; Graham, D.; Haes, A. J.; Haynes, C. L.; et al. Present and Future of Surface-Enhanced Raman Scattering. *ACS Nano* **2020**, *14*, 28–117.
- (114) Aydin, O.; Altas, M.; Kahraman, M.; Bayrak, O. F.; Culha, M. Differentiation of Healthy Brain Tissue and Tumors Using Surface-Enhanced Raman Scattering. *Appl. Spectrosc.* **2009**, *63*, 1095–1100.
- (115) Rivera Gil, P.; Vazquez, C. V.; Giannini, V.; Callao, M. P.; Parak, W. J.; Duarte, M. A. C.; Alvarez-Puebla, R. A. Plasmonic Nanoprobes for Real-Time Optical Monitoring of Nitric Oxide inside Living Cells. *Angew. Chem., Int. Ed.* **2013**, *52*, 13694–13698.
- (116) Köker, T.; Tang, N.; Tian, C.; Zhang, W.; Wang, X.; Martel, R.; Pinaud, F. Cellular Imaging by Targeted Assembly of Hot-Spot SERS and Photoacoustic Nanoprobes Using Split-Fluorescent Protein Scaffolds. *Nat. Commun.* **2018**, *9*, 607.
- (117) Lenzi, E.; Jimenez de Aberasturi, D.; Liz-Marzán, L. M. Surface-Enhanced Raman Scattering Tags for Three-Dimensional Bioimaging and Biomarker Detection. *ACS Sensors* **2019**, *4*, 1126–1137.
- (118) Álvarez-Puebla, R. A. Effects of the Excitation Wavelength on the SERS Spectrum. *J. Phys. Chem. Lett.* **2012**, *3*, 857–866.
- (119) Smith, B. R.; Gambhir, S. S. Nanomaterials for *in Vivo* Imaging. *Chem. Rev.* **2017**, *117*, 901–986.
- (120) Zavaleta, C. L.; Smith, B. R.; Walton, I.; Doering, W.; Davis, G.; Shojaei, B.; Natan, M. J.; Gambhir, S. S. Multiplexed Imaging of Surface Enhanced Raman Scattering Nanotags in Living Mice Using Noninvasive Raman Spectroscopy. *Proc. Natl. Acad. Sci. U. S. A.* **2009**, *106*, 13511.
- (121) Jimenez de Aberasturi, D.; Serrano-Montes, A. B.; Langer, J.; Henriksen-Lacey, M.; Parak, W. J.; Liz-Marzán, L. M. Encoded Gold Nanostars for Multiplexed SERS Cell Differentiation. *Chem. Mater.* **2016**, *28*, 6779–6790.
- (122) Jimenez de Aberasturi, D.; Henriksen-Lacey, M.; Litti, L.; Langer, J.; Liz-Marzán, L. M. Using SERS Tags to Image the Three-Dimensional Structure of Complex Cell Models. *Adv. Funct. Mater.* **2020**, *30*, 1909655.
- (123) Alvarez-Puebla, R. A.; Zubarev, E. R.; Kotov, N. A.; Liz-Marzán, L. M. Self-Assembled Nanorod Supercrystals for Ultra-sensitive SERS Diagnostics. *Nano Today* **2012**, *7*, 6–9.
- (124) Alvarez-Puebla, R. A.; Agarwal, A.; Manna, P.; Khanal, B. P.; Aldeanueva-Potel, P.; Carbo-Argibay, E.; Pazos-Perez, N.; Vigderman, L.; Zubarev, E. R.; Kotov, N. A.; Liz-Marzán, L. M. Gold Nanorods 3D-Supercrystals as Surface Enhanced Raman Scattering Spectroscopy Substrates for the Rapid Detection of Scrambled Prions. *Proc. Natl. Acad. Sci. U. S. A.* **2011**, *108*, 8157–8161.
- (125) Feliu, N.; Hassan, M.; Garcia Rico, E.; Cui, D.; Parak, W.; Alvarez-Puebla, R. SERS Quantification and Characterization of Proteins and Other Biomolecules. *Langmuir* **2017**, *33*, 9711–9730.
- (126) Carrillo-Carrion, C.; Martinez, R.; Navarro Poupard, M. F.; Pelaz, B.; Polo, E.; Arenas-Vivo, A.; Olgiatei, A.; Taboada, P.; Soliman, M. G.; Catalan, U.; Fernandez-Castillejo, S.; Sola, R.; Parak, W. J.; Horcajada, P.; Alvarez-Puebla, R. A.; del Pino, P. Aqueous Stable Gold Nanostar/ZIF-8 Nanocomposites for Light-Triggered Release of Active Cargo inside Living Cells. *Angew. Chem., Int. Ed.* **2019**, *58*, 7078–7082.
- (127) Gerling, M.; Zhao, Y.; Nania, S.; Norberg, K. J.; Verbeke, C. S.; Englert, B.; Kuiper, R. V.; Bergstrom, A.; Hassan, M.; Neesse, A.; Lohr, J. M.; Heuchel, R. L. Real-Time Assessment of Tissue Hypoxia *in Vivo* with Combined Photoacoustics and High-Frequency Ultrasound. *Theranostics* **2014**, *4*, 604–613.
- (128) Zhao, Y.; Zheng, W.; Hassan, M. Chapter 4 - Nanoparticles for Imaging Application. In *Frontiers of Nanoscience- Colloids for Nanobiotechnology. Synthesis, Characterization and Potential Applications*; Parak, W. J., Feliu, N., Eds.; Elsevier: Amsterdam, The Netherlands, 2020; Vol. 16, pp 67–88.
- (129) Lakshmanan, A.; Farhadi, A.; Nety, S. P.; Lee-Gosselin, A.; Bourdeau, R. W.; Maresca, D.; Shapiro, M. G. Molecular Engineering of Acoustic Protein Nanostructures. *ACS Nano* **2016**, *10*, 7314–7322.
- (130) Ling, B.; Lee, J.; Maresca, D.; Lee-Gosselin, A.; Malounda, D.; Swift, M. B.; Shapiro, M. G. Biomolecular Ultrasound Imaging of Phagolysosomal Function. *ACS Nano* **2020**, *14*, 12210–12221.
- (131) Shapiro, M. G.; Goodwill, P. W.; Neogy, A.; Yin, M.; Foster, F. S.; Schaffer, D. V.; Conolly, S. M. Biogenic Gas Nanostructures as Ultrasonic Molecular Reporters. *Nat. Nanotechnol.* **2014**, *9*, 311–316.
- (132) Fu, Q.; Zhu, R.; Song, J.; Yang, H.; Chen, X. Photoacoustic Imaging: Contrast Agents and Their Biomedical Applications. *Adv. Mater.* **2019**, *31*, 1805875.
- (133) Cai, Y.; Wei, Z.; Song, C.; Tang, C.; Han, W.; Dong, X. Optical Nano-Agents in the Second Near-Infrared Window for Biomedical Applications. *Chem. Soc. Rev.* **2019**, *48*, 22–37.
- (134) Shu, X.; Beckmann, L.; Zhang, H. F. Visible-Light Optical Coherence Tomography: A Review. *J. Biomed. Opt.* **2017**, *22*, 1–14.
- (135) Tan, A. C. S.; Tan, G. S.; Denniston, A. K.; Keane, P. A.; Ang, M.; Milea, D.; Chakravarthy, U.; Cheung, C. M. G. An Overview of the Clinical Applications of Optical Coherence Tomography Angiography. *Eye* **2018**, *32*, 262–286.

- (136) Pahlevaninezhad, H.; Khorasaninejad, M.; Huang, Y.-W.; Shi, Z.; Hariri, L. P.; Adams, D. C.; Ding, V.; Zhu, A.; Qiu, C.-W.; Capasso, F.; Suter, M. J. Nano-Optic Endoscope for High-Resolution Optical Coherence Tomography *in Vivo*. *Nat. Photonics* **2018**, *12*, 540–547.
- (137) Fujimoto, J. G. Optical Coherence Tomography for Ultrahigh Resolution *in Vivo* Imaging. *Nat. Biotechnol.* **2003**, *21*, 1361–1367.
- (138) Li, Y. L.; Seekell, K.; Yuan, H.; Robles, F. E.; Wax, A. Multispectral Nanoparticle Contrast Agents for True-Color Spectroscopic Optical Coherence Tomography. *Biomed. Opt. Express* **2012**, *3*, 1914–1923.
- (139) Liba, O.; SoRelle, E. D.; Sen, D.; de la Zerda, A. Contrast-Enhanced Optical Coherence Tomography with Picomolar Sensitivity for Functional *in Vivo* Imaging. *Sci. Rep.* **2016**, *6*, 23337.
- (140) Nguyen, V. P.; Li, Y.; Qian, W.; Liu, B.; Tian, C.; Zhang, W.; Huang, Z.; Ponduri, A.; Tarnowski, M.; Wang, X.; Paulus, Y. M. Contrast Agent Enhanced Multimodal Photoacoustic Microscopy and Optical Coherence Tomography for Imaging of Rabbit Choroidal and Retinal Vessels *in Vivo*. *Sci. Rep.* **2019**, *9*, 5945.
- (141) Si, P.; Yuan, E.; Liba, O.; Winetraub, Y.; Yousefi, S.; SoRelle, E. D.; Yecies, D. W.; Dutta, R.; de la Zerda, A. Gold Nanoprisms as Optical Coherence Tomography Contrast Agents in the Second Near-Infrared Window for Enhanced Angiography in Live Animals. *ACS Nano* **2018**, *12*, 11986–11994.
- (142) Tucker-Schwartz, J. M.; Beavers, K. R.; Sit, W. W.; Shah, A. T.; Duvall, C. L.; Skala, M. C. *In Vivo* Imaging of Nanoparticle Delivery and Tumor Microvasculature with Multimodal Optical Coherence Tomography. *Biomed. Opt. Express* **2014**, *5*, 1731–1743.
- (143) Weissleder, R. A Clearer Vision for *in Vivo* Imaging. *Nat. Biotechnol.* **2001**, *19*, 316–317.
- (144) Smith, A. M.; Mancini, M. C.; Nie, S. Second Window for *in Vivo* Imaging. *Nat. Nanotechnol.* **2009**, *4*, 710–711.
- (145) Kenry; Duan, Y.; Liu, B. Recent Advances of Optical Imaging in the Second Near-Infrared Window. *Adv. Mater.* **2018**, *30*, 1802394.
- (146) Liguori, C.; Frauenfelder, G.; Massaroni, C.; Saccomandi, P.; Giurazza, F.; Pitocco, F.; Marano, R.; Schena, E. Emerging Clinical Applications of Computed Tomography. *Med. Devices: Evidence Res.* **2015**, *8*, 265–278.
- (147) Momose, A.; Takeda, T.; Itai, Y.; Hirano, K. Phase-Contrast X-Ray Computed Tomography for Observing Biological Soft Tissues. *Nat. Med.* **1996**, *2*, 473–475.
- (148) Martínez-Criado, G.; Segura-Ruiz, J.; Alén, B.; Eymery, J.; Rogalev, A.; Tucoulou, R.; Homs, A. Exploring Single Semiconductor Nanowires with a Multimodal Hard X-ray Nanoprobe. *Adv. Mater.* **2014**, *26*, 7873–7879.
- (149) Decelle, J.; Veronesi, G.; Gallet, B.; Stryhanyuk, H.; Benettoni, P.; Schmidt, M.; Tucoulou, R.; Passarelli, M.; Bohic, S.; Clode, P.; Musat, N. Subcellular Chemical Imaging: New Avenues in Cell Biology. *Trends Cell Biol.* **2020**, *30*, 173–188.
- (150) Yano, J.; Yachandra, V. K. X-Ray Absorption Spectroscopy. *Photosynth. Res.* **2009**, *102*, 241.
- (151) Koziej, D. Revealing Complexity of Nanoparticle Synthesis in Solution by *in Situ* Hard X-Ray Spectroscopy—Today and Beyond. *Chem. Mater.* **2016**, *28*, 2478–2490.
- (152) Pushie, M. J.; Pickering, I. J.; Korbas, M.; Hackett, M. J.; George, G. N. Elemental and Chemically Specific X-Ray Fluorescence Imaging of Biological Systems. *Chem. Rev.* **2014**, *114*, 8499–8541.
- (153) Lamberti, C.; Bordiga, S.; Bonino, F.; Prestipino, C.; Berlier, G.; Capello, L.; D'Acapito, F.; Llabrés i Xamena, F. X.; Zecchina, A. Determination of the Oxidation and Coordination State of Copper on Different Cu-Based Catalysts by XANES Spectroscopy *in Situ* or *in Operando* Conditions. *Phys. Chem. Chem. Phys.* **2003**, *5*, 4502–4509.
- (154) Hémonnot, C. Y. J.; Koster, S. Imaging of Biological Materials and Cells by X-Ray Scattering and Diffraction. *ACS Nano* **2017**, *11*, 8542–8559.
- (155) Morrison, G. R.; Niemann, B. Differential Phase Contrast X-Ray Microscopy. In *X-Ray Microscopy and Spectromicroscopy: Status Report from the Fifth International Conference, Würzburg, August 19–23, 1996*; Thieme, J., Schmahl, G., Rudolph, D., Umbach, E., Eds.; Springer: Berlin, Heidelberg, 1998; pp 85–94.
- (156) Chen, H.; Wang, Z.; Gao, K.; Hou, Q.; Wang, D.; Wu, Z. Quantitative Phase Retrieval in X-Ray Zernike Phase Contrast Microscopy. *J. Synchrotron Radiat.* **2015**, *22*, 1056–1061.
- (157) Yang, Y.; Cheng, Y.; Heine, R.; Baumbach, T. Contrast Transfer Functions for Zernike Phase Contrast in Full-Field Transmission Fard X-Ray Microscopy. *Opt. Express* **2016**, *24*, 6063–70.
- (158) Grübel, G.; Zontone, F. Correlation Spectroscopy with Coherent X-Rays. *J. Alloys Compd.* **2004**, *362*, 3–11.
- (159) Holmqvist, P.; Meester, V.; Westermeier, F.; Kleshchanok, D. Rotational Diffusion in Concentrated Platelet Systems Measured with X-Ray Photon Correlation Spectroscopy. *J. Chem. Phys.* **2013**, *139*, 084905.
- (160) Westermeier, F.; Pennicard, D.; Hirsemann, H.; Wagner, U. H.; Rau, C.; Graafsma, H.; Schall, P.; Lettinga, M. P.; Struth, B. Connecting Structure, Dynamics and Viscosity in Sheared Soft Colloidal Liquids: A Medley of Anisotropic Fluctuations. *Soft Matter* **2016**, *12*, 171–180.
- (161) Caronna, C.; Chushkin, Y.; Madsen, A.; Cupane, A. Dynamics of Nanoparticles in a Supercooled Liquid. *Phys. Rev. Lett.* **2008**, *100*, 055702.
- (162) Pearson, A. R.; von Stetten, D.; Huse, N. If You Can Get a Crystal Structure, Why Bother with Anything Else? *Synchrotron Radiat. News.* **2015**, *28*, 10–14.
- (163) Holder, C. F.; Schaak, R. E. Tutorial on Powder X-Ray Diffraction for Characterizing Nanoscale Materials. *ACS Nano* **2019**, *13*, 7359–7365.
- (164) Mourdikoudis, S.; Pallares, R. M.; Thanh, N. T. K. Characterization Techniques for Nanoparticles: Comparison and Complementarity upon Studying Nanoparticle Properties. *Nanoscale* **2018**, *10*, 12871–12934.
- (165) Liang, K.; Richardson, J. J.; Cui, J.; Caruso, F.; Doonan, C. J.; Falcro, P. Metal–Organic Framework Coatings as Cytoprotective Exoskeletons for Living Cells. *Adv. Mater.* **2016**, *28*, 7910–7914.
- (166) Lam, Y. Y.; Hawley, A.; Tan, A.; Boyd, B. J. Coupling *in Vitro* Cell Culture with Synchrotron SAXS to Understand the Bio-Interaction of Lipid-Based Liquid Crystalline Nanoparticles with Vascular Endothelial Cells. *Drug Delivery Transl. Res.* **2020**, *10*, 610–620.
- (167) Veronesi, G.; Brun, E.; Fayard, B.; Cotte, M.; Carrière, M. Structural Properties of Rutile TiO<sub>2</sub> Nanoparticles Accumulated in a Model of Gastrointestinal Epithelium Elucidated by Micro-Beam X-Ray Absorption Fine Structure Spectroscopy. *Appl. Phys. Lett.* **2012**, *100*, 214101.
- (168) Auffan, M.; Decome, L.; Rose, J.; Orsiere, T.; De Meo, M.; Briois, V.; Chaneac, C.; Olivi, L.; Berge-LeFranc, J.-I.; Botta, A.; Wiesner, M. R.; Bottero, J.-y. *In Vitro* Interactions between DMSA-Coated Maghemite Nanoparticles and Human Fibroblasts: A Physicochemical and Cyto-Genotoxicity Study. *Environ. Sci. Technol.* **2006**, *40*, 4367–4373.
- (169) Martínez-Criado, G.; Villanova, J.; Tucoulou, R.; Salomon, D.; Suuronen, J.-P.; Labouré, S.; Guilloud, C.; Valls, V.; Barrett, R.; Gagliardini, E.; Dabin, Y.; Baker, R.; Bohic, S.; Cohen, C.; Morse, J. ID16B: A Hard X-Ray Nanoprobe Beamline at the ESRF for Nano-Analysis. *J. Synchrotron Radiat.* **2016**, *23*, 344–352.
- (170) Cesar da Silva, J.; Pacureanu, A.; Yang, Y.; Bohic, S.; Morawe, C.; Barrett, R.; Cloetens, P. Efficient Concentration of High-Energy X-Rays for Diffraction-Limited Imaging Resolution. *Optica* **2017**, *4*, 492–495.
- (171) *Welcome to B24: Full Field Cryo-X-Ray Microscopy for the Life Sciences*; Diamond Light Source Ltd.: Oxfordshire, UK. <http://www.diamond.ac.uk/Instruments/Biological-Cryo-Imaging/B24.html> (accessed 2020-11-01).

- (172) Welcome to I08: The Diamond Scanning X-Ray Microscopy Beamline; Diamond Light Source Ltd.: Oxfordshire, UK. <http://www.diamond.ac.uk/Instruments/Imaging-and-Microscopy/I08.html> (accessed 2020-11-01).
- (173) Welcome to I14: Hard X-Ray Nanoprobe; Diamond Light Source Ltd.: Oxfordshire, UK. <https://www.diamond.ac.uk/Instruments/Imaging-and-Microscopy/I14.html> (accessed 2020-11-01).
- (174) Schroer, C. G.; Boye, P.; Feldkamp, J. M.; Patommel, J.; Samberg, D.; Schropp, A.; Schwab, A.; Stephan, S.; Falkenberg, G.; Wellenreuther, G.; Reimers, N. Hard X-Ray Nanoprobe at Beamline P06 at PETRA III. *Nucl. Instrum. Methods Phys. Res., Sect. A* **2010**, *616*, 93–97.
- (175) Pereiro, E.; Nicolás, J.; Ferrer, S.; Howells, M. R. A Soft X-Ray Beamline for Transmission X-Ray Microscopy at ALBA. *J. Synchrotron Radiat.* **2009**, *16*, 505–512.
- (176) Somogyi, A.; Medjoubi, K.; Baranton, G.; Le Roux, V.; Ribbens, M.; Polack, F.; Philippot, P.; Samama, J.-P. Optical Design and Multi-Length-Scale Scanning Spectro-Microscopy Possibilities at the Nanoscopium Beamline of Synchrotron Soleil. *J. Synchrotron Radiat.* **2015**, *22*, 1118–1129.
- (177) Kalbfleisch, S.; Neubauer, H.; Krüger, S. P.; Bartels, M.; Osterhoff, M.; Mai, D. D.; Giewekemeyer, K.; Hartmann, B.; Sprung, M.; Salditt, T.; et al. The Göttingen Holography Endstation of Beamline P10 at PETRA III/DESY. *AIP Conf. Proc.* **2010**, *1365*, 96–99.
- (178) PETRA III - Facility Information; DESY: Hamburg, Germany. [http://photon-science.desy.de/facilities/petra\\_iii/facility\\_information/index\\_eng.html](http://photon-science.desy.de/facilities/petra_iii/facility_information/index_eng.html). (accessed 2020-11-01).
- (179) Dullin, C.; dal Monego, S.; Larsson, E.; Mohammadi, S.; Krenkel, M.; Garrovo, C.; Biffi, S.; Lorenzon, A.; Markus, A.; Napp, J.; Salditt, T.; Accardo, A.; Alves, F.; Tromba, G. Functionalized Synchrotron in-Line Phase-Contrast Computed Tomography: A Novel Approach for Simultaneous Quantification of Structural Alterations and Localization of Barium-Labelled Alveolar Macrophages within Mouse Lung Samples. *J. Synchrotron Radiat.* **2015**, *22*, 143–155.
- (180) Chien, C.-C.; Chen, H.-H.; Lai, S.-F.; Wu, K.-C.; Cai, X.; Hwu, Y.; Petibois, C.; Chu, Y.; Margaritondo, G. Gold Nanoparticles as High-Resolution X-Ray Imaging Contrast Agents for the Analysis of Tumor-Related Micro-Vasculature. *J. Nanobiotechnol.* **2012**, *10*, 10.
- (181) Weinhardt, V.; Chen, J. H.; Ekman, A.; McDermott, G.; Le Gros, M. A.; Larabell, C. Imaging Cell Morphology and Physiology Using X-Rays. *Biochem. Soc. Trans.* **2019**, *47*, 489–508.
- (182) Midgley, P. A.; Ward, E. P.; Hungria, A. B.; Thomas, J. M. Nanotomography in the Chemical, Biological and Materials Sciences. *Chem. Soc. Rev.* **2007**, *36*, 1477–1494.
- (183) Schroer, C. G.; Seyrich, M.; Schropp, A.; Dohrmann, R.; Botta, S.; Wiljes, P.; Bruckner, D.; Kahnt, M.; Wittwer, F.; Grote, L.; Koziej, D.; Garrevoet, J.; Falkenberg, G. Ptychographic Nano-Analytical Microscope (PtyNAMi) at PETRA III: Signal-to-Background Optimization for Imaging with High Sensitivity. *Proc. SPIE* **2019**, *11112*, 111120D.
- (184) Shavorskiy, A.; Neppel, S.; Slaughter, D. S.; Cryan, J. P.; Siefermann, K. R.; Weise, F.; Lin, M.-F.; Bacellar, C.; Ziemkiewicz, M. P.; Zegkinoglou, I.; Fraund, M. W.; Khurmi, C.; Hertlein, M. P.; Wright, T. W.; Huse, N.; Schoenlein, R. W.; Tyliczszak, T.; Coslovich, G.; Robinson, J.; Kaindl, R. A.; et al. Sub-Nanosecond Time-Resolved Ambient-Pressure X-Ray Photoelectron Spectroscopy Setup for Pulsed and Constant Wave X-Ray Light Sources. *Rev. Sci. Instrum.* **2014**, *85*, 093102.
- (185) Neppel, S.; Mahl, J.; Tremsin, A. S.; Rude, B.; Qiao, R.; Yang, W.; Guo, J.; Gessner, O. Towards Efficient Time-Resolved X-Ray Absorption Studies of Electron Dynamics at Photocatalytic Interfaces. *Faraday Discuss.* **2016**, *194*, 659–682.
- (186) Allahgholi, A.; Becker, J.; Delfs, A.; Dinapoli, R.; Goettlicher, P.; Greiffenberg, D.; Henrich, B.; Hirsemann, H.; Kuhn, M.; Klanner, R.; Klyuev, A.; Krueger, H.; Lange, S.; Laurus, T.; Marras, A.; Mezza, D.; Mozzanica, A.; Niemann, M.; Poehlsen, J.; Schwandt, J.; et al. The Adaptive Gain Integrating Pixel Detector at the European XFEL. *J. Synchrotron Radiat.* **2019**, *26*, 74–82.
- (187) Zhang, Q.; Bahadur, D.; Dufresne, E. M.; Grybos, P.; Kmon, P.; Leheny, R. L.; Maj, P.; Narayanan, S.; Szczygiel, R.; Ramakrishnan, S.; Sandy, A. Dynamic Scaling of Colloidal Gel Formation at Intermediate Concentrations. *Phys. Rev. Lett.* **2017**, *119*, 178006.
- (188) Dicke, B.; Hoffmann, A.; Stanek, J.; Rampp, M. S.; Grimm-Lebsanft, B.; Biebl, F.; Rukser, D.; Maerz, B.; Göries, D.; Naumova, M.; Biednov, M.; Neuber, G.; Wetzel, A.; Hofmann, S. M.; Roedig, P.; Meents, A.; Bielecki, J.; Andreasson, J.; Beyerlein, K. R.; Chapman, H. N.; et al. Transferring the Entatic-State Principle to Copper Photochemistry. *Nat. Chem.* **2018**, *10*, 355–362.
- (189) Gallagher-Jones, M.; Dias, C. S. B.; Pryor, A., Jr.; Bouchmella, K.; Zhao, L.; Lo, Y. H.; Cardoso, M. B.; Shapiro, D.; Rodriguez, J.; Miao, J. Correlative Cellular Ptychography with Functionalized Nanoparticles at the Fe L-Edge. *Sci. Rep.* **2017**, *7*, 4757.
- (190) Hoffmann, A.; Citek, C.; Binder, S.; Goos, A.; Rübhausen, M.; Troeppler, O.; Ivanović-Burmazović, I.; Wasinger, E. C.; Stack, T. D. P.; Herres-Pawlis, S. Catalytic Phenol Hydroxylation with Dioxygen: Extension of the Tyrosinase Mechanism Beyond the Protein Matrix. *Angew. Chem., Int. Ed.* **2013**, *52*, 5398–5401.
- (191) Fiedler, H. D.; Drinkel, E. E.; Orzechowicz, B.; Leopoldino, E. C.; Souza, F. D.; Almerindo, G. I.; Perdonà, C.; Nome, F. Simultaneous Nondestructive Analysis of Palladium, Rhodium, Platinum, and Gold Nanoparticles Using Energy Dispersive X-Ray Fluorescence. *Anal. Chem.* **2013**, *85*, 10142–10148.
- (192) Zheng, W.; He, R.; Boada, R.; Subirana, M. A.; Ginman, T.; Ottosson, H.; Valiente, M.; Zhao, Y.; Hassan, M. A General Covalent Binding Model between Cytotoxic Selenocompounds and Albumin Revealed by Mass Spectrometry and X-Ray Absorption Spectroscopy. *Sci. Rep.* **2020**, *10*, 1274.
- (193) Uhlig, J.; Doriese, W. B.; Fowler, J. W.; Swetz, D. S.; Jaye, C.; Fischer, D. A.; Reintsema, C. D.; Bennett, D. A.; Vale, L. R.; Mandal, U.; O'Neil, G. C.; Miaja-Avila, L.; Joe, Y. I.; El Nahhas, A.; Fullagar, W.; Parnefjord Gustafsson, F.; Sundstrom, V.; Kurunthu, D.; Hilton, G. C.; Schmidt, D. R.; Ullom, J. N. High-Resolution X-Ray Emission Spectroscopy with Transition-Edge Sensors: Present Performance and Future Potential. *J. Synchrotron Radiat.* **2015**, *22*, 766–775.
- (194) Bandler, S. R.; Adams, J. S.; et al. Development of X-Ray Microcalorimeter Imaging Spectrometers for the X-Ray Surveyor Mission Concept. *Proc. SPIE* **2016**, *9905*, 99050Q.
- (195) Doriese, W. B.; Abbamonte, P.; Alpert, B. K.; Bennett, D. A.; Denison, E. V.; Fang, Y.; Fischer, D. A.; Fitzgerald, C. P.; Fowler, J. W.; Gard, J. D.; Hays-Wehle, J. P.; Hilton, G. C.; Jaye, C.; McChesney, J. L.; Miaja-Avila, L.; Morgan, K. M.; Joe, Y. I.; O'Neil, G. C.; Reintsema, C. D.; Rodolakis, F.; et al. A Practical Superconducting-Microcalorimeter X-Ray Spectrometer for Beamline and Laboratory Science. *Rev. Sci. Instrum.* **2017**, *88*, 053108.
- (196) den Herder, J. W.; Kelley, R. L.; Mitsuda, K.; Piro, L.; Bandler, S. R.; Bastia, P.; Boyce, K. R.; Bruin, M.; Chervenak, J. A.; Colasanti, L.; Doriese, W. B.; DiPirro, M.; Eckart, M. E.; Ezoe, Y.; Figueroa-Feliciano, E.; Ferrari, L.; Fujimoto, R.; Gatti, F.; Gendreau, K. C.; Gottardi, L.; et al. The X-Ray Microcalorimeter Spectrometer Onboard of IXO. *Proc. SPIE* **2010**, *7732*, 77321H.
- (197) Moosmann, J.; Ershov, A.; Altapova, V.; Baumbach, T.; Prasad, M. S.; LaBonne, C.; Xiao, X.; Kashef, J.; Hofmann, R. X-Ray Phase-Contrast *in Vivo* Microtomography Probes New Aspects of *Xenopus* Gastrulation. *Nature* **2013**, *497*, 374–377.
- (198) Moosmann, J.; Ershov, A.; Weinhardt, V.; Baumbach, T.; Prasad, M. S.; LaBonne, C.; Xiao, X.; Kashef, J.; Hofmann, R. Time-Lapse X-Ray Phase-Contrast Microtomography for *in Vivo* Imaging and Analysis of Morphogenesis. *Nat. Protoc.* **2014**, *9*, 294–304.
- (199) Chen, H.; Rogalski, M. M.; Anker, J. N. Advances in Functional X-Ray Imaging Techniques and Contrast Agents. *Phys. Chem. Chem. Phys.* **2012**, *14*, 13469–13486.

- (200) Kalinko, A.; Caliebe, W. A.; Schoch, R.; Bauer, M. A Von Hamos-Type Hard X-Ray Spectrometer at the PETRA III Beamline P64. *J. Synchrotron Radiat.* **2020**, *27*, 31–36.
- (201) Jones, S. A.; Shim, S.-H.; He, J.; Zhuang, X. Fast, Three-Dimensional Super-Resolution Imaging of Live Cells. *Nat. Methods* **2011**, *8*, 499–505.
- (202) Sahl, S. J.; Hell, S. W.; Jakobs, S. Fluorescence Nanoscopy in Cell Biology. *Nat. Rev. Mol. Cell Biol.* **2017**, *18*, 685–701.
- (203) Dai, M.; Jungmann, R.; Yin, P. Optical Imaging of Individual Biomolecules in Densely Packed Clusters. *Nat. Nanotechnol.* **2016**, *11*, 798–807.
- (204) Kaulich, B.; Thibault, P.; Gianoncelli, A.; Kiskinova, M. Transmission and Emission X-Ray Microscopy: Operation Modes, Contrast Mechanisms and Applications. *J. Phys.: Condens. Matter* **2011**, *23*, 083002.
- (205) Miao, J.; Ishikawa, T.; Robinson, I. K.; Murnane, M. M. Beyond Crystallography: Diffractive Imaging Using Coherent X-Ray Light Sources. *Science* **2015**, *348*, 530–535.
- (206) Hanssen, E.; Knoechel, C.; Dearnley, M.; Dixon, M. W.; Le Gros, M.; Larabell, C.; Tilley, L. Soft X-Ray Microscopy Analysis of Cell Volume and Hemoglobin Content in Erythrocytes Infected with Asexual and Sexual Stages of *Plasmodium falciparum*. *J. Struct. Biol.* **2012**, *177*, 224–232.
- (207) Yang, Y.; Li, W.; Liu, G.; Zhang, X.; Chen, J.; Wu, W.; Guan, Y.; Xiong, Y.; Tian, Y.; Wu, Z. 3D Visualization of Subcellular Structures of *Schizosaccharomyces pombe* by Hard X-Ray Tomography. *J. Microsc.* **2010**, *240*, 14–20.
- (208) Hubbell, J.; Seltzer, S. X-Ray Mass Attenuation Coefficients. Tables of X-Ray Mass Attenuation Coefficients and Mass Energy-Absorption Coefficients from 1 keV to 20 MeV for Elements  $Z = 1$  to 92 and 48 Additional Substances of Dosimetric Interest. NIST 5632; Physics Laboratory, NIST: Gaithersburg, MD, 2004.
- (209) Deng, J.; Lo, Y. H.; Gallagher-Jones, M.; Chen, S.; Pryor, A.; Jin, Q.; Hong, Y. P.; Nashed, Y. S. G.; Vogt, S.; Miao, J.; Jacobsen, C. Correlative 3D X-Ray Fluorescence and Ptychographic Tomography of Frozen-Hydrated Green Algae. *Sci. Adv.* **2018**, *4*, No. eaau4548.
- (210) Chen, Z. Y.; Liu, Y.; Sun, B. Y.; Li, H.; Dong, J. Q.; Zhang, L. J.; Wang, L. M.; Wang, P.; Zhao, Y. L.; Chen, C. Y. Polyhydroxylated Metallofullerenols Stimulate IL-1 Beta Secretion of Macrophage through TLRs/MyD88/NF-Kappa B Pathway and NLRP3 Inflammasome Activation. *Small* **2014**, *10*, 2362–2372.
- (211) Wang, J.; Liu, J.; Liu, Y.; Wang, L.; Cao, M.; Ji, Y.; Wu, X.; Xu, Y.; Bai, B.; Miao, Q.; Chen, C.; Zhao, Y. Gd-Hybridized Plasmonic Au-Nanocomposites Enhanced Tumor-Interior Drug Permeability in Multimodal Imaging-Guided Therapy. *Adv. Mater.* **2016**, *28*, 8950–8958.
- (212) Miao, J.; Förster, F.; Levi, O. Equally Sloped Tomography with Oversampling Reconstruction. *Phys. Rev. B: Condens. Matter Mater. Phys.* **2005**, *72*, 052103.
- (213) Lee, E.; Fahimian, B. P.; Iancu, C. V.; Suloway, C.; Murphy, G. E.; Wright, E. R.; Castaño-Díez, D.; Jensen, G. J.; Miao, J. Radiation Dose Reduction and Image Enhancement in Biological Imaging through Equally-Sloped Tomography. *J. Struct. Biol.* **2008**, *164*, 221–227.
- (214) Yao, S.; Fan, J.; Chen, Z.; Zong, Y.; Zhang, J.; Sun, Z.; Zhang, L.; Tai, R.; Liu, Z.; Chen, C.; Jiang, H. Three-Dimensional Ultrastructural Imaging Reveals the Nanoscale Architecture of Mammalian Cells. *IUCr* **2018**, *5*, 141–149.
- (215) Do, M.; Isaacson, S. A.; McDermott, G.; Le Gros, M. A.; Larabell, C. A. Imaging and Characterizing Cells Using Tomography. *Arch. Biochem. Biophys.* **2015**, *581*, 111–121.
- (216) Zheng, H.; Ji, Z.; Roy, K. R.; Gao, M.; Pan, Y.; Cai, X.; Wang, L.; Li, W.; Chang, C. H.; Kaweeteerawat, C.; Chen, C.; Xia, T.; Zhao, Y.; Li, R. Engineered Graphene Oxide Nanocomposite Capable of Preventing the Evolution of Antimicrobial Resistance. *ACS Nano* **2019**, *13*, 11488–11499.
- (217) Jiang, H.; Song, C.; Chen, C. C.; Xu, R.; Raines, K. S.; Fahimian, B. P.; Lu, C. H.; Lee, T. K.; Nakashima, A.; Urano, J.; Ishikawa, T.; Tamanoi, F.; Miao, J. Quantitative 3D Imaging of Whole, Unstained Cells by Using X-Ray Diffraction Microscopy. *Proc. Natl. Acad. Sci. U. S. A.* **2010**, *107*, 11234–11239.
- (218) Nishino, Y.; Takahashi, Y.; Imamoto, N.; Ishikawa, T.; Maeshima, K. Three-Dimensional Visualization of a Human Chromosome Using Coherent X-Ray Diffraction. *Phys. Rev. Lett.* **2009**, *102*, 018101.
- (219) Nelson, J.; Huang, X.; Steinbrener, J.; Shapiro, D.; Kirz, J.; Marchesini, S.; Neiman, A. M.; Turner, J. J.; Jacobsen, C. High-Resolution X-Ray Diffraction Microscopy of Specifically Labeled Yeast Cells. *Proc. Natl. Acad. Sci. U. S. A.* **2010**, *107*, 7235–7239.
- (220) de Jonge, M. D.; Holzner, C.; Baines, S. B.; Twining, B. S.; Ignatyev, K.; Diaz, J.; Howard, D. L.; Legnini, D.; Miceli, A.; McNulty, I.; Jacobsen, C. J.; Vogt, S. Quantitative 3D Elemental Microtomography of *Cyclotella meneghiniana* at 400-nm Resolution. *Proc. Natl. Acad. Sci. U. S. A.* **2010**, *107*, 15676–15680.
- (221) Cagno, S.; Brede, D. A.; Nuyts, G.; Vanmeert, F.; Pacureanu, A.; Tucoulou, R.; Cloetens, P.; Falkenberg, G.; Janssens, K.; Salbu, B.; Lind, O. C. Combined Computed Nanotomography and Nanoscopic X-Ray Fluorescence Imaging of Cobalt Nanoparticles in *Caenorhabditis elegans*. *Anal. Chem.* **2017**, *89*, 11435–11442.
- (222) James, S. A.; Burke, R.; Howard, D. L.; Spiers, K. M.; Paterson, D. J.; Murphy, S.; Ramm, G.; Kirkham, R.; Ryan, C. G.; de Jonge, M. D. Visualising Coordination Chemistry: Fluorescence X-Ray Absorption near Edge Structure Tomography. *Chem. Commun.* **2016**, *52*, 11834–11837.
- (223) Deng, J.; Vine, D. J.; Chen, S.; Nashed, Y. S.; Jin, Q.; Phillips, N. W.; Peterka, T.; Ross, R.; Vogt, S.; Jacobsen, C. J. Simultaneous Cryo X-Ray Ptychographic and Fluorescence Microscopy of Green Algae. *Proc. Natl. Acad. Sci. U. S. A.* **2015**, *112*, 2314–2319.
- (224) Jones, M. W.; Elgass, K. D.; Junker, M. D.; de Jonge, M. D.; van Riessen, G. A. Molar Concentration from Sequential 2-D Water-Window X-Ray Ptychography and X-Ray Fluorescence in Hydrated Cells. *Sci. Rep.* **2016**, *6*, 24280.
- (225) Ding, J.; Guan, Y.; Cong, Y.; Chen, L.; Li, Y. F.; Zhang, L.; Zhang, L.; Wang, J.; Bai, R.; Zhao, Y.; Chen, C.; Wang, L. Single-Particle Analysis for Structure and Iron Chemistry of Atmospheric Particulate Matter. *Anal. Chem.* **2020**, *92*, 975–982.
- (226) Le Gros, M. A.; McDermott, G.; Larabell, C. A. X-Ray Tomography of Whole Cells. *Curr. Opin. Struct. Biol.* **2005**, *15*, 593–600.
- (227) Brandenberger, C.; Mühlfeld, C.; Ali, Z.; Lenz, A.-G.; Schmid, O.; Parak, W. J.; Gehr, P.; Rothen-Rutishauser, B. Quantitative Evaluation of Cellular Uptake and Trafficking of Plain and Polyethylene Glycol-Coated Gold Nanoparticles. *Small* **2010**, *6*, 1669–1678.
- (228) Chapman, H. N.; Fu, J.; Jacobsen, C.; Williams, S. Dark-Field X-Ray Microscopy of Immunogold-Labeled Cells. *Microsc. Microanal.* **1996**, *2*, 53–62.
- (229) Matsuyama, S.; Shimura, M.; Mimura, H.; Fujii, M.; Yumoto, H.; Sano, Y.; Yabashi, M.; Nishino, Y.; Tamasaku, K.; Ishikawa, T.; Yamauchi, K. Trace Element Mapping of a Single Cell Using a Hard X-Ray Nanobeam Focused by a Kirkpatrick-Baez Mirror System. *X-Ray Spectrom.* **2009**, *38*, 89–94.
- (230) Kong, H.; Zhang, J.; Li, J.; Wang, J.; Shin, H.-J.; Tai, R.; Yan, Q.; Xia, K.; Hu, J.; Wang, L.; Zhu, Y.; Fan, C. Genetically Encoded X-Ray Cellular Imaging for Nanoscale Protein Localization. *Natl. Sci. Rev.* **2020**, *7*, 1218–1227.
- (231) Zhai, J.; Wang, Y.; Xu, C.; Zheng, L.; Wang, M.; Feng, W.; Gao, L.; Zhao, L.; Liu, R.; Gao, F.; Zhao, Y.; Chai, Z.; Gao, X. Facile Approach to Observe and Quantify the  $\alpha$ IIb $\beta$ 3 Integrin on a Single-Cell. *Anal. Chem.* **2015**, *87*, 2546–2549.
- (232) Metscher, B. D. MicroCT for Comparative Morphology: Simple Staining Methods Allow High-Contrast 3D Imaging of Diverse Non-Mineralized Animal Tissues. *BMC Physiol.* **2009**, *9*, 11.
- (233) Cloetens, P.; Barrett, R.; Baruchel, J.; Guigay, J.-P.; Schlenker, M. Phase Objects in Synchrotron Radiation Hard X-Ray Imaging. *J. Phys. D: Appl. Phys.* **1996**, *29* (1), 133–146.

- (234) Pfeiffer, F. X-Ray Ptychography. *Nat. Photonics* **2018**, *12*, 9–17.
- (235) Carmona, A.; Zogzas, C. E.; Roudeau, S.; Porcaro, F.; Garrovoet, J.; Spiers, K. M.; Salomé, M.; Cloetens, P.; Mukhopadhyay, S.; Ortega, R. SLC30A10 Mutation Involved in Parkinsonism Results in Manganese Accumulation within Nanovesicles of the Golgi Apparatus. *ACS Chem. Neurosci.* **2019**, *10*, 599–609.
- (236) Yuan, Y.; Chen, S.; Paunesku, T.; Gleber, S. C.; Liu, W. C.; Doty, C. B.; Mak, R.; Deng, J.; Jin, Q.; Lai, B.; Brister, K.; Flachenecker, C.; Jacobsen, C.; Vogt, S.; Woloschak, G. E. Epidermal Growth Factor Receptor Targeted Nuclear Delivery and High-Resolution Whole Cell X-Ray Imaging of Fe<sub>3</sub>O<sub>4</sub>@TiO<sub>2</sub> Nanoparticles in Cancer Cells. *ACS Nano* **2013**, *7*, 10502–10517.
- (237) Krenkel, M.; Toepferwien, M.; Alves, F.; Salditt, T. Three-Dimensional Single-Cell Imaging with X-Ray Waveguides in the Holographic Regime. *Acta Crystallogr., Sect. A: Found. Adv.* **2017**, *73*, 282–292.
- (238) Ashraf, S.; Said, A. H.; Hartmann, R.; Assmann, M.-A.; Feliu, N.; Lenz, P.; Parak, W. J. Quantitative Particle Uptake by Cells as Analyzed by Different Methods. *Angew. Chem., Int. Ed.* **2020**, *59*, 5438–5453.
- (239) Zhang, J.; Cai, X.; Zhang, Y.; Li, X.; Li, W.; Tian, Y.; Li, A.; Yu, X.; Fan, C.; Huang, Q. Imaging Cellular Uptake and Intracellular Distribution of TiO<sub>2</sub> Nanoparticles. *Anal. Methods* **2013**, *5*, 6611–6616.
- (240) Mei, L.; Zhang, X.; Yin, W.; Dong, X.; Guo, Z.; Fu, W.; Su, C.; Gu, Z.; Zhao, Y. Translocation, Biotransformation-Related Degradation, and Toxicity Assessment of Polyvinylpyrrolidone-Modified 2H-Phase Mano-MoS<sub>2</sub>. *Nanoscale* **2019**, *11*, 4767–4780.
- (241) Krenkel, M.; Markus, A.; Bartels, M.; Dullin, C.; Alves, F.; Salditt, T. Phase-Contrast Zoom Tomography Reveals Precise Locations of Macrophages in Mouse Lungs. *Sci. Rep.* **2015**, *5*, 9973.
- (242) Cedola, A.; Bravin, A.; Bukreeva, I.; Fratini, M.; Pacureanu, A.; Mittone, A.; Massimi, L.; Cloetens, P.; Coan, P.; Campi, G.; Spanò, R.; Brun, F.; Grigoryev, V.; Petrosino, V.; Venturi, C.; Mastrogiacomo, M.; Kerlero de Rosbo, N.; Uccelli, A. X-Ray Phase Contrast Tomography Reveals Early Vascular Alterations and Neuronal Loss in a Multiple Sclerosis Model. *Sci. Rep.* **2017**, *7*, 5890.
- (243) Töpferwien, M.; Krenkel, M.; Vincenz, D.; Stöber, F.; Oelschlegel, A. M.; Goldschmidt, J.; Salditt, T. Three-Dimensional Mouse Brain Cytoarchitecture Revealed by Laboratory-Based X-Ray Phase-Contrast Tomography. *Sci. Rep.* **2017**, *7*, 42847.
- (244) Töpferwien, M.; van der Meer, F.; Stadelmann, C.; Salditt, T. Three-Dimensional Virtual Histology of Human Cerebellum by X-Ray Phase-Contrast Tomography. *Proc. Natl. Acad. Sci. U. S. A.* **2018**, *115*, 6940.
- (245) Reichardt, M.; Töpferwien, M.; Khan, A.; Alves, F.; Salditt, T. Fiber Orientation in a Whole Mouse Heart Reconstructed by Laboratory Phase-Contrast Micro-CT. *J. Med. Imaging.* **2020**, *7*, 023501.
- (246) Töpferwien, M.; Doepfner, T. R.; Zechmeister, B.; Bähr, M.; Salditt, T. Multiscale X-Ray Phase-Contrast Tomography in a Mouse Model of Transient Focal Cerebral Ischemia. *Biomed. Opt. Express* **2019**, *10*, 92–103.
- (247) Bartels, M.; Hernandez, V. H.; Krenkel, M.; Moser, T.; Salditt, T. Phase Contrast Tomography of the Mouse Cochlea at Microfocus X-Ray Sources. *Appl. Phys. Lett.* **2013**, *103*, 083703.
- (248) Krenkel, M.; Töpferwien, M.; Dullin, C.; Alves, F.; Salditt, T. Propagation-Based Phase-Contrast Tomography for High-Resolution Lung Imaging with Laboratory Sources. *AIP Adv.* **2016**, *6*, 035007.
- (249) Bartels, M.; Priebe, M.; Wilke, R. N.; Krüger, S. P.; Giewekemeyer, K.; Kalbfleisch, S.; Olendrowitz, C.; Sprung, M.; Salditt, T. Low-Dose Three-Dimensional Hard X-Ray Imaging of Bacterial Cells. *Opt. Nanoscopy* **2012**, *1*, 10.
- (250) Nicolas, J.-D.; Bernhardt, M.; Krenkel, M.; Richter, C.; Luther, S.; Salditt, T. Combined Scanning X-Ray Diffraction and Holographic Imaging of Cardiomyocytes. *J. Appl. Crystallogr.* **2017**, *50*, 612–620.
- (251) Bartels, M.; Krenkel, M.; Cloetens, P.; Möbius, W.; Salditt, T. Myelinated Mouse Nerves Studied by X-Ray Phase Contrast Zoom Tomography. *J. Struct. Biol.* **2015**, *192*, S61–S68.
- (252) Raupach, R.; Flohr, T. G. Analytical Evaluation of the Signal and Noise Propagation in X-Ray Differential Phase-Contrast Computed Tomography. *Phys. Med. Biol.* **2011**, *56*, 2219–2244.
- (253) Wen, S.; Li, K.; Cai, H.; Chen, Q.; Shen, M.; Huang, Y.; Peng, C.; Hou, W.; Zhu, M.; Zhang, G.; Shi, X. Multifunctional Dendrimer-Entrapped Gold Nanoparticles for Dual Mode CT/MR Imaging Applications. *Biomaterials* **2013**, *34*, 1570–1580.
- (254) Zhang, J.; Li, C.; Zhang, X.; Huo, S.; Jin, S.; An, F.-F.; Wang, X.; Xue, X.; Okeke, C. I.; Duan, G.; Guo, F.; Zhang, X.; Hao, J.; Wang, P. C.; Zhang, J.; Liang, X.-J. *In Vivo* Tumor-Targeted Dual-Modal Fluorescence/CT Imaging Using a Nanoprobe Co-Loaded with an Aggregation-Induced Emission Dye and Gold Nanoparticles. *Biomaterials* **2015**, *42*, 103–111.
- (255) Xu, X.; Zhao, L.; Li, X.; Wang, P.; Zhao, J.; Shi, X.; Shen, M. Targeted Tumor SPECT/CT Dual Mode Imaging Using Multifunctional RGD-Modified Low Generation Dendrimer-Entrapped Gold Nanoparticles. *Biomater. Sci.* **2017**, *5*, 2393–2397.
- (256) Willemink, M. J.; Persson, M.; Pourmorteza, A.; Pelc, N. J.; Fleischmann, D. Photon-Counting CT: Technical Principles and Clinical Prospects. *Radiology* **2018**, *289*, 293–312.
- (257) Si-Mohamed, S.; Bar-Ness, D.; Sigovan, M.; Cormode, D. P.; Coulon, P.; Coche, E.; Vlassenbroek, A.; Normand, G.; Boussel, L.; Douek, P. Review of an Initial Experience with an Experimental Spectral Photon-Counting Computed Tomography System. *Nucl. Instrum. Methods Phys. Res., Sect. A* **2017**, *873*, 27–35.
- (258) Symons, R.; Krauss, B.; Sahbaee, P.; Cork, T. E.; Lakshmanan, M. N.; Bluemke, D. A.; Pourmorteza, A. Photon-Counting CT for Simultaneous Imaging of Multiple Contrast Agents in the Abdomen: An *in Vivo* Study. *Med. Phys.* **2017**, *44*, S120–S127.
- (259) Cormode, D. P.; Si-Mohamed, S.; Bar-Ness, D.; Sigovan, M.; Naha, P. C.; Balegamire, J.; Lavenne, F.; Coulon, P.; Roessler, E.; Bartels, M.; Rokni, M.; Blevis, I.; Boussel, L.; Douek, P. Multicolor Spectral Photon-Counting Computed Tomography: *In Vivo* Dual Contrast Imaging with a High Count Rate Scanner. *Sci. Rep.* **2017**, *7*, 4784.
- (260) Pan, D.; Schirra, C. O.; Senpan, A.; Schmieder, A. H.; Stacy, A. J.; Roessler, E.; Thran, A.; Wickline, S. A.; Proksa, R.; Lanza, G. M. An Early Investigation of Ytterbium Nanocolloids for Selective and Quantitative “Multicolor” Spectral CT Imaging. *ACS Nano* **2012**, *6*, 3364–3370.
- (261) Hsu, J. C.; Nieves, L. M.; Betzer, O.; Sadan, T.; Noël, P. B.; Popovtzer, R.; Cormode, D. P. Nanoparticle Contrast Agents for X-Ray Imaging Applications. *Wiley Interdiscip. Rev.: Nanomed. Nanobiotechnol.* **2020**, *12*, No. e1642.
- (262) Pan, D.; Roessler, E.; Schlomka, J.-P.; Caruthers, S. D.; Senpan, A.; Scott, M. J.; Allen, J. S.; Zhang, H.; Hu, G.; Gaffney, P. J.; Choi, E. T.; Rasche, V.; Wickline, S. A.; Proksa, R.; Lanza, G. M. Computed Tomography in Color: NanoK-Enhanced Spectral CT Molecular Imaging. *Angew. Chem., Int. Ed.* **2010**, *49*, 9635–9639.
- (263) Naha, P. C.; Hsu, J. C.; Kim, J.; Shah, S.; Bouché, M.; Si-Mohamed, S.; Rosario-Berrios, D. N.; Douek, P.; Hajfathalian, M.; Yasini, P.; Singh, S.; Rosen, M. A.; Morgan, M. A.; Cormode, D. P. Dextran-Coated Cerium Oxide Nanoparticles: A Computed Tomography Contrast Agent for Imaging the Gastrointestinal Tract and Inflammatory Bowel Disease. *ACS Nano* **2020**, *14*, 10187–10197.
- (264) Si-Mohamed, S.; Cormode, D. P.; Bar-Ness, D.; Sigovan, M.; Naha, P. C.; Langlois, J.-B.; Chalabreysse, L.; Coulon, P.; Blevis, I.; Roessler, E.; Erhard, K.; Boussel, L.; Douek, P. Evaluation of Spectral Photon Counting Computed Tomography K-Edge Imaging for Determination of Gold Nanoparticle Biodistribution *in Vivo*. *Nanoscale* **2017**, *9*, 18246–18257.

- (265) Kong, F.-Y.; Zhang, J.-W.; Li, R.-F.; Wang, Z.-X.; Wang, W.-J.; Wang, W. Unique Roles of Gold Nanoparticles in Drug Delivery, Targeting and Imaging Applications. *Molecules* **2017**, *22*, 1445.
- (266) Ando, H.; Abu Lila, A. S.; Tanaka, M.; Doi, Y.; Terada, Y.; Yagi, N.; Shimizu, T.; Okuhira, K.; Ishima, Y.; Ishida, T. Intratumoral Visualization of Oxaliplatin within a Liposomal Formulation Using X-Ray Fluorescence Spectrometry. *Mol. Pharmaceutics* **2018**, *15*, 403–409.
- (267) Sanchez-Cano, C.; Romero-Canelón, I.; Geraki, K.; Sadler, P. J. Microfocus X-Ray Fluorescence Mapping of Tumour Penetration by an Organoosmium Anticancer Complex. *J. Inorg. Biochem.* **2018**, *185*, 26–29.
- (268) Koba, R.; Fujita, H.; Nishibori, M.; Saeki, K.; Nagayoshi, K.; Sadakari, Y.; Nagai, S.; Sekizawa, O.; Nitta, K.; Manabe, T.; Ueki, T.; Ishida, T.; Oda, Y.; Nakamura, M. Quantitative Evaluation of the Intratumoral Distribution of Platinum in Oxaliplatin-Treated Rectal Cancer: *In Situ* Visualization of Platinum via Synchrotron Radiation X-Ray Fluorescence Spectrometry. *Int. J. Cancer* **2020**, *146*, 2498–2509.
- (269) Bulin, A.-L.; Broekgaarden, M.; Chaput, F.; Baisamy, V.; Garrevoet, J.; Busser, B.; Brueckner, D.; Youssef, A.; Ravanat, J.-L.; Dujardin, C.; Motto-Ros, V.; Lerouge, F.; Bohic, S.; Sancey, L.; Elleaume, H. Radiation Dose-Enhancement Is a Potent Radiotherapeutic Effect of Rare-Earth Composite Nanoscintillators in Preclinical Models of Glioblastoma. *Adv. Sci.* **2020**, *7*, 2001675.
- (270) Lehmann, S. G.; Toybou, D.; Pradas Del Real, A. E.; Arndt, D.; Tagmount, A.; Viau, M.; Safi, M.; Pacureanu, A.; Cloetens, P.; Bohic, S.; Salome, M.; Castillo-Michel, H.; Omana-Sanz, B.; Hofmann, A.; Vulpe, C.; Simonato, J. P.; Celle, C.; Charlet, L.; Gilbert, B. Crumpling of Silver Nanowires by Endolysosomes Strongly Reduces Toxicity. *Proc. Natl. Acad. Sci. U. S. A.* **2019**, *116*, 14893–14898.
- (271) Vitol, E. A.; Rozhkova, E. A.; Rose, V.; Stripe, B. D.; Young, N. R.; Cohen, E. E. W.; Leoni, L.; Novosad, V. Efficient Cisplatin Pro-Drug Delivery Visualized with Sub-100 nm Resolution: Interfacing Engineered Thermosensitive Magnetomicelles with a Living System. *Adv. Mater. Interfaces* **2014**, *1*, 1400182.
- (272) Sanchez-Cano, C.; Romero-Canelón, I.; Yang, Y.; Hands-Portman, I. J.; Bohic, S.; Cloetens, P.; Sadler, P. J. Synchrotron X-Ray Fluorescence Nanoprobe Reveals Target Sites for Organo-Osmium Complex in Human Ovarian Cancer Cells. *Chem. - Eur. J.* **2017**, *23*, 2512–2516.
- (273) Reith, F.; Etschmann, B.; Grosse, C.; Moors, H.; Benotmane, M. A.; Monsieurs, P.; Grass, G.; Doonan, C.; Vogt, S.; Lai, B.; Martinez-Criado, G.; George, G. N.; Nies, D. H.; Mergeay, M.; Pring, A.; Southam, G.; Brugger, J. Mechanisms of Gold Biomineralization in the Bacterium *Cupriavidus metallidurans*. *Proc. Natl. Acad. Sci. U. S. A.* **2009**, *106*, 17757–17762.
- (274) Korbass, M.; Blechinger, S. R.; Krone, P. H.; Pickering, I. J.; George, G. N. Localizing Organomercury Uptake and Accumulation in Zebrafish Larvae at the Tissue and Cellular Level. *Proc. Natl. Acad. Sci. U. S. A.* **2008**, *105*, 12108.
- (275) Schreiber, I.; Hesse, B.; Seim, C.; Castillo-Michel, H.; Villanova, J.; Laux, P.; Dreijack, N.; Penning, R.; Tucoulou, R.; Cotte, M.; Luch, A. Synchrotron-Based  $\nu$ -XRF Mapping and  $\mu$ -FTIR Microscopy Enable to Look into the Fate and Effects of Tattoo Pigments in Human Skin. *Sci. Rep.* **2017**, *7*, 11395.
- (276) Servin, A. D.; Castillo-Michel, H.; Hernandez-Viezas, J. A.; Diaz, B. C.; Peralta-Videa, J. R.; Gardea-Torresdey, J. L. Synchrotron Micro-XRF and Micro-XANES Confirmation of the Uptake and Translocation of TiO<sub>2</sub> Nanoparticles in Cucumber (*Cucumis sativus*) Plants. *Environ. Sci. Technol.* **2012**, *46*, 7637–7643.
- (277) Castillo-Michel, H. A.; Larue, C.; Pradas del Real, A. E.; Cotte, M.; Sarret, G. Practical Review on the Use of Synchrotron Based Micro- and Nano- X-Ray Fluorescence Mapping and X-Ray Absorption Spectroscopy to Investigate the Interactions between Plants and Engineered Nanomaterials. *Plant Physiol. Biochem.* **2017**, *110*, 13–32.
- (278) Schultke, E.; Menk, R.; Pinzer, B.; Astolfo, A.; Stampanoni, M.; Arfelli, F.; Harsan, L. A.; Nikkhah, G. Single-Cell Resolution in High-Resolution Synchrotron X-Ray CT Imaging with Gold Nanoparticles. *J. Synchrotron Radiat.* **2014**, *21*, 242–250.
- (279) Brümmer, T.; Debus, A.; Pausch, R.; Osterhoff, J.; Grüner, F. Design Study for a Compact Laser-Driven Source for Medical X-Ray Fluorescence Imaging. *Phys. Rev. Accel. Beams.* **2020**, *23*, 031601.
- (280) Chan, K. L. A.; Fale, P. L. V.; Atharawi, A.; Wehbe, K.; Cinque, G. Subcellular Mapping of Living Cells via Synchrotron MicroFTIR and ZnS Hemispheres. *Anal. Bioanal. Chem.* **2018**, *410*, 6477–6487.
- (281) Holman, H.-Y. N.; Miles, R.; Hao, Z.; Wozel, E.; Anderson, L. M.; Yang, H. Real-Time Chemical Imaging of Bacterial Activity in Biofilms Using Open-Channel Microfluidics and Synchrotron FTIR Spectromicroscopy. *Anal. Chem.* **2009**, *81*, 8564–8570.
- (282) Doherty, J.; Raouf, A.; Hussain, A.; Wolna, M.; Cinque, G.; Brown, M.; Gardner, P.; Denbigh, J. Live Single Cell Analysis Using Synchrotron FTIR Microspectroscopy: Development of a Simple Dynamic Flow System for Prolonged Sample Viability. *Analyst* **2019**, *144*, 997–1007.
- (283) Miller, L. M.; Bourassa, M. W.; Smith, R. J. FTIR Spectroscopic Imaging of Protein Aggregation in Living Cells. *Biochim. Biophys. Acta, Biomembr.* **2013**, *1828*, 2339–2346.
- (284) Pijanka, J.; Sockalingum, G. D.; Kohler, A.; Yang, Y.; Draux, F.; Parkes, G.; Lam, K. P.; Collins, D.; Dumas, P.; Sandt, C.; van Pittius, D. G.; Douce, G.; Manfait, M.; Untereiner, V.; Sule-Suso, J. Synchrotron-Based FTIR Spectra of Stained Single Cells. Towards a Clinical Application in Pathology. *Lab. Invest.* **2010**, *90*, 797–807.
- (285) Morgan, K. S.; Parsons, D.; Cmielewski, P.; McCarron, A.; Gradl, R.; Farrow, N.; Siu, K.; Takeuchi, A.; Suzuki, Y.; Uesugi, K.; Uesugi, M.; Yagi, N.; Hall, C.; Klein, M.; Maksimenko, A.; Stevenson, A.; Hausermann, D.; Dierolf, M.; Pfeiffer, F.; Donnelley, M. Methods for Dynamic Synchrotron X-Ray Respiratory Imaging in Live Animals. *J. Synchrotron Radiat.* **2020**, *27*, 164–175.
- (286) Gradl, R.; Dierolf, M.; Yang, L.; Hehn, L.; Günther, B.; Möller, W.; Kutschke, D.; Stoeger, T.; Gleich, B.; Achterhold, K.; Donnelley, M.; Pfeiffer, F.; Schmid, O.; Morgan, K. S. Visualizing Treatment Delivery and Deposition in Mouse Lungs Using *In Vivo* X-Ray Imaging. *J. Controlled Release* **2019**, *307*, 282–291.
- (287) Gradl, R.; Dierolf, M.; Günther, B.; Hehn, L.; Möller, W.; Kutschke, D.; Yang, L.; Donnelley, M.; Murrie, R.; Erl, A.; Stoeger, T.; Gleich, B.; Achterhold, K.; Schmid, O.; Pfeiffer, F.; Morgan, K. S. *In Vivo* Dynamic Phase-Contrast X-Ray Imaging Using a Compact Light Source. *Sci. Rep.* **2018**, *8*, 6788.
- (288) Vakili, M.; Merckens, S.; Gao, Y.; Gwozdz, P. V.; Vasireddi, R.; Sharpnack, L.; Meyer, A.; Blick, R. H.; Trebbin, M. 3D Micromachined Polyimide Mixing Devices for *In Situ* X-Ray Imaging of Solution-Based Block Copolymer Phase Transitions. *Langmuir* **2019**, *35*, 10435–10445.
- (289) Merckens, S.; Vakili, M.; Sanchez-Iglesias, A.; Litt, L.; Gao, Y.; Gwozdz, P. V.; Sharpnack, L.; Blick, R. H.; Liz-Marzan, L. M.; Grzelczak, M.; Trebbin, M. Time-Resolved Analysis of the Structural Dynamics of Assembling Gold Nanoparticles. *ACS Nano* **2019**, *13*, 6596–6604.
- (290) Bhat, A.; Gwozdz, P. V.; Seshadri, A.; Hoeft, M.; Blick, R. H. Tank Circuit for Ultrafast Single-Particle Detection in Micropores. *Phys. Rev. Lett.* **2018**, *121*, 078102.
- (291) Nolte, P.; Stierle, A.; Jin-Phillipp, N. Y.; Kasper, N.; Schulli, T. U.; Dosch, H. Shape Changes of Supported Rh Nanoparticles during Oxidation and Reduction Cycles. *Science* **2008**, *321*, 1654–1658.
- (292) Nolte, P.; Stierle, A.; Kasper, N.; Jin-Phillipp, N. Y.; Jeutter, N.; Dosch, H. Reversible Shape Changes of Pd Nanoparticles on MgO(100). *Nano Lett.* **2011**, *11*, 4697–4700.
- (293) Hejral, U.; Franz, D.; Volkov, S.; Francoual, S.; Stempfer, J.; Stierle, A. Identification of a Catalytically Highly Active Surface

Phase for CO Oxidation over PtRh Nanoparticles under *Operando* Reaction Conditions. *Phys. Rev. Lett.* **2018**, *120*, 126101.

(294) Nolte, P.; Stierle, A.; Kasper, N.; Jin-Phillipp, N. Y.; Reichert, H.; Rühm, A.; Okasinski, J.; Dosch, H.; Schöder, S. Combinatorial High-Energy X-Ray Microbeam Study of the Size-Dependent Oxidation of Pd Nanoparticles on MgO(100). *Phys. Rev. B: Condens. Matter Mater. Phys.* **2008**, *77*, 115444.

(295) Hejral, U.; Müller, P.; Balmes, O.; Pontoni, D.; Stierle, A. Tracking the Shape-Dependent Sintering of Platinum-Rhodium Model Catalysts under *Operando* Conditions. *Nat. Commun.* **2016**, *7*, 10964.

(296) Abuin, M.; Kim, Y. Y.; Runge, H.; Kulkarni, S.; Maier, S.; Dzhigaev, D.; Lazarev, S.; Gelisio, L.; Seitz, C.; Richard, M.-I.; Zhou, T.; Vonk, V.; Keller, T. F.; Vartanyants, I. A.; Stierle, A. Coherent X-Ray Imaging of CO-Adsorption-Induced Structural Changes in Pt Nanoparticles: Implications for Catalysis. *ACS Appl. Nano Mater.* **2019**, *2*, 4818–4824.

(297) Kawaguchi, T.; Keller, T. F.; Runge, H.; Gelisio, L.; Seitz, C.; Kim, Y. Y.; Maxey, E. R.; Cha, W.; Ulvestad, A.; Hruszkewycz, S. O.; Harder, R.; Vartanyants, I. A.; Stierle, A.; You, H. Gas-Induced Segregation in Pt-Rh Alloy Nanoparticles Observed by *In Situ* Bragg Coherent Diffraction Imaging. *Phys. Rev. Lett.* **2019**, *123*, 246001.

(298) Müller, P.; Hejral, U.; Rütt, U.; Stierle, A. *In Situ* Oxidation Study of Pd-Rh Nanoparticles on MgAl<sub>2</sub>O<sub>4</sub>(001). *Phys. Chem. Chem. Phys.* **2014**, *16*, 13866–13874.

(299) Sayes, C. M.; Wahi, R.; Kurian, P. A.; Liu, Y. P.; West, J. L.; Ausman, K. D.; Warheit, D. B.; Colvin, V. L. Correlating Nanoscale Titania Structure with Toxicity: A Cytotoxicity and Inflammatory Response Study with Human Dermal Fibroblasts and Human Lung Epithelial Cells. *Toxicol. Sci.* **2006**, *92*, 174–185.

(300) Zhang, Q.; Lai, W.; Yin, T.; Zhang, C.; Yue, C.; Cheng, J.; Wang, K.; Yang, Y.; Cui, D.; Parak, W. J. Investigation of the Viability of Cells upon Co-Exposure to Gold and Iron Oxide Nanoparticles. *Bioconjugate Chem.* **2018**, *29*, 2120–2125.

(301) Lo, Y. H.; Zhao, L.; Gallagher-Jones, M.; Rana, A.; Lodico, J. J.; Xiao, W.; Regan, B. C.; Miao, J. *In Situ* Coherent Diffractive Imaging. *Nat. Commun.* **2018**, *9*, 1826.

(302) Carril, M.; Padro, D.; del Pino, P.; Carrillo-Carrion, C.; Gallego, M.; Parak, W. J. *In Situ* Detection of the Protein Corona in Complex Environments. *Nat. Commun.* **2017**, *8*, 1542.

(303) Bruetzel, L. K.; Fischer, S.; Salditt, A.; Sedlak, S. M.; Nickel, B.; Lipfert, J. A Mo-Anode-Based In-House Source for Small-Angle X-Ray Scattering Measurements of Biological Macromolecules. *Rev. Sci. Instrum.* **2016**, *87*, 025103.

(304) Zhang, F.; Allen, A. J.; Levine, L. E.; Espinal, L.; Antonucci, J. M.; Skrtic, D.; O'Donnell, J. N.; Ilavsky, J. Ultra-Small-Angle X-Ray Scattering-X-Ray Photon Correlation Spectroscopy Studies of Incipient Structural Changes in Amorphous Calcium Phosphate-Based Dental Composites. *J. Biomed. Mater. Res., Part A* **2012**, *100*, 1293–1306.

(305) Reich, C.; Hochrein, M. B.; Krause, B.; Nickel, B. A Microfluidic Setup for Studies of Solid-Liquid Interfaces Using X-Ray Reflectivity and Fluorescence Microscopy. *Rev. Sci. Instrum.* **2005**, *76*, 095103.

(306) Saurel, D.; Segalini, J.; Jauregui, M.; Pendashteh, A.; Daffos, B.; Simon, P.; Casas-Cabanas, M. A SAXS Outlook on Disordered Carbonaceous Materials for Electrochemical Energy Storage. *Energy Stor. Mater.* **2019**, *21*, 162–173.

(307) Xia, Y.; Nguyen, T. D.; Yang, M.; Lee, B.; Santos, A.; Podsiadlo, P.; Tang, Z.; Glotzer, S. C.; Kotov, N. A. Self-Assembly of Self-Limiting Monodisperse Supraparticles from Polydisperse Nanoparticles. *Nat. Nanotechnol.* **2011**, *6*, 580–587.

(308) Merkens, S.; Vakili, M.; Sánchez-Iglesias, A.; Littl, L.; Gao, Y.; Gwozdź, P. V.; Sharpnack, L.; Blick, R. H.; Liz-Marzán, L. M.; Grzelczak, M.; Trebbin, M. Time-Resolved Analysis of the Structural Dynamics of Assembling Gold Nanoparticles. *ACS Nano* **2019**, *13*, 6596–6604.

(309) Podsiadlo, P.; Michel, M.; Critchley, K.; Srivastava, S.; Qin, M.; Lee, J. W.; Verploegen, E.; Hart, A. J.; Qi, Y.; Kotov, N. A.

Diffusional Self-Organization in Exponential Layer-by-Layer Films with Micro- and Nanoscale Periodicity. *Angew. Chem., Int. Ed.* **2009**, *48*, 7073–7077.

(310) Tang, Z.; Kotov, N. A.; Magonov, S.; Ozturk, B. Nanostructured Artificial Nacre. *Nat. Mater.* **2003**, *2*, 413–418.

(311) Zhang, J.; Feng, W.; Zhang, H.; Wang, Z.; Calcaterra, H. A.; Yeom, B.; Hu, P. A.; Kotov, N. A. Multiscale Deformations Lead to High Toughness and Circularly Polarized Emission in Helical Nacre-Like Fibres. *Nat. Commun.* **2016**, *7*, 10701.

(312) Slocik, J. M.; Govorov, A. O.; Naik, R. R. Plasmonic Circular Dichroism of Peptide-Functionalized Gold Nanoparticles. *Nano Lett.* **2011**, *11*, 701–705.

(313) Karst, J.; Cho, N. H.; Kim, H.; Lee, H.-E.; Nam, K. T.; Giessen, H.; Hentschel, M. Chiral Scatterometry on Chemically Synthesized Single Plasmonic Nanoparticles. *ACS Nano* **2019**, *13*, 8659–8668.

(314) Huang, Y.; Fu, Y.; Li, M.; Jiang, D.; Kuttyreff, C. J.; Engle, J. W.; Lan, X.; Cai, W.; Chen, T. Chirality-Driven Transportation and Oxidation Prevention by Chiral Selenium Nanoparticles. *Angew. Chem., Int. Ed.* **2020**, *59*, 4406–4414.

(315) Li, S.; Liu, J.; Ramesar, N. S.; Heinz, H.; Xu, L.; Xu, C.; Kotov, N. A. Single- and Multi-Component Chiral Supraparticles as Modular Enantioselective Catalysts. *Nat. Commun.* **2019**, *10*, 4826.

(316) Feng, W.; Kim, J.-Y.; Wang, X.; Calcaterra, H. A.; Qu, Z.; Meshi, L.; Kotov, N. A. Assembly of Mesoscale Helices with Near-Unity Enantiomeric Excess and Light-Matter Interactions for Chiral Semiconductors. *Sci. Adv.* **2017**, *3*, No. e1601159.

(317) Sun, M.; Xu, L.; Bahng, J. H.; Kuang, H.; Alben, S.; Kotov, N. A.; Xu, C. Intracellular Localization of Nanoparticle Dimers by Chirality Reversal. *Nat. Commun.* **2017**, *8*, 1847.

(318) Li, S.; Xu, L.; Ma, W.; Wu, X.; Sun, M.; Kuang, H.; Wang, L.; Kotov, N. A.; Xu, C. Dual-Mode Ultrasensitive Quantification of MicroRNA in Living Cells by Chiroplasmonic Nanopyramids Self-Assembled from Gold and Upconversion Nanoparticles. *J. Am. Chem. Soc.* **2016**, *138*, 306–312.

(319) Sun, M.; Hao, T.; Li, X.; Qu, A.; Xu, L.; Hao, C.; Xu, C.; Kuang, H. Direct Observation of Selective Autophagy Induction in Cells and Tissues by Self-Assembled Chiral Nanodevice. *Nat. Commun.* **2018**, *9*, 4494.

(320) Tang, Y.; Cohen, A. E. Optical Chirality and Its Interaction with Matter. *Phys. Rev. Lett.* **2010**, *104*, 163901.

(321) Solomon, M. L.; Saleh, A. A. E.; Poulikakos, L. V.; Abendroth, J. M.; Tadesse, L. F.; Dionne, J. A. Nanophotonic Platforms for Chiral Sensing and Separation. *Acc. Chem. Res.* **2020**, *53*, 588–598.

(322) Li, Y.; Zhou, Y.; Wang, H. Y.; Perrett, S.; Zhao, Y.; Tang, Z.; Nie, G. Chirality of Glutathione Surface Coating Affects the Cytotoxicity of Quantum Dots. *Angew. Chem., Int. Ed.* **2011**, *50*, 5860–5864.

(323) González-Rubio, G.; Mosquera, J.; Kumar, V.; Pedrazo-Tardajos, A.; Llombart, P.; Solís, D. M.; Lobato, I.; Noya, E. G.; Guerrero-Martínez, A.; Taboada, J. M.; Obelleiro, F.; MacDowell, L. G.; Bals, S.; Liz-Marzán, L. M. Micelle-Directed Chiral Seeded Growth on Anisotropic Gold Nanocrystals. *Science* **2020**, *368*, 1472–1477.

(324) Yan, W.; Xu, L.; Xu, C.; Ma, W.; Kuang, H.; Wang, L.; Kotov, N. A. Self-Assembly of Chiral Nanoparticle Pyramids with Strong R/S Optical Activity. *J. Am. Chem. Soc.* **2012**, *134*, 15114–15121.

(325) Jana, S.; de Frutos, M.; Davidson, P.; Abécassis, B. Ligand-Induced Twisting of Nanoplatelets and Their Self-Assembly into Chiral Ribbons. *Sci. Adv.* **2017**, *3*, No. e1701483.

(326) Jiang, W.; Qu, Z.-b.; Kumar, P.; Vecchio, D.; Wang, Y.; Ma, Y.; Bahng, J. H.; Bernardino, K.; Gomes, W. R.; Colombari, F. M.; Lozada-Blanco, A.; Veksler, M.; Marino, E.; Simon, A.; Murray, C.; Muniz, S. R.; de Moura, A. F.; Kotov, N. A. Emergence of Complexity in Hierarchically Organized Chiral Particles. *Science* **2020**, *368*, 642–648.

- (327) Ahn, J.; Ma, S.; Kim, J.-Y.; Kyhm, J.; Yang, W.; Lim, J. A.; Kotov, N. A.; Moon, J. Chiral 2D Organic Inorganic Hybrid Perovskite with Circular Dichroism Tunable over Wide Wavelength Range. *J. Am. Chem. Soc.* **2020**, *142*, 4206–4212.
- (328) Schroer, C. G.; Falkenberg, G. Hard X-Ray Nanofocusing at Low-Emittance Synchrotron Radiation Sources. *J. Synchrotron Radiat.* **2014**, *21*, 996–1005.
- (329) Weckert, E. The Potential of Future Light Sources to Explore the Structure and Function of Matter. *IUCrJ* **2015**, *2*, 230–245.
- (330) Schroer, C. G.; Agapov, I.; Brefeld, W.; Brinkmann, R.; Chae, Y.-C.; Chao, H.-C.; Eriksson, M.; Keil, J.; Nuel Gavaldà, X.; Rohlsberger, R.; Seeck, O. H.; Sprung, M.; Tischer, M.; Wanzenberg, R.; Weckert, E. PETRA IV: The Ultralow-Emittance Source Project at DESY. *J. Synchrotron Radiat.* **2018**, *25*, 1277–1290.
- (331) Di Mitri, S. One Way Only to Synchrotron Light Sources Upgrade? *J. Synchrotron Radiat.* **2018**, *25*, 1323–1334.
- (332) Hettel, R. DLSR Design and Plans: An International Overview. *J. Synchrotron Radiat.* **2014**, *21*, 843–855.
- (333) Eriksson, M.; van der Veen, J. F.; Quitmann, C. Diffraction-Limited Storage Rings - A Window to the Science of Tomorrow. *J. Synchrotron Radiat.* **2014**, *21*, 837–842.
- (334) Boldon, L.; Laliberte, F.; Liu, L. Review of the Fundamental Theories Behind Small Angle X-Ray Scattering, Molecular Dynamics Simulations, and Relevant Integrated Application. *Nano Rev.* **2015**, *6*, 25661.
- (335) Fratzl, P.; Jakob, H. F.; Rinnerthaler, S.; Roschger, P.; Klaushofer, K. Position-Resolved Small-Angle X-Ray Scattering of Complex Biological Materials. *J. Appl. Crystallogr.* **1997**, *30*, 765–769.
- (336) He, W. X.; Rajasekharan, A. K.; Tehrani-Bagha, A. R.; Andersson, M. Mesoscopically Ordered Bone-Mimetic Nanocomposites. *Adv. Mater.* **2015**, *27*, 2260–2264.
- (337) Nicolas, J. D.; Bernhardt, M.; Markus, A.; Alves, F.; Burghammer, M.; Salditt, T. Scanning X-Ray Diffraction on Cardiac Tissue: Automated Data Analysis and Processing. *J. Synchrotron Radiat.* **2017**, *24*, 1163–1172.
- (338) Jensen, T. H.; Bech, M.; Bunk, O.; Thomsen, M.; Menzel, A.; Bouchet, A.; Le Duc, G.; Feidenhans'l, R.; Pfeiffer, F. Brain Tumor Imaging Using Small-Angle X-Ray Scattering Tomography. *Phys. Med. Biol.* **2011**, *56*, 1717–1726.
- (339) Schaff, F.; Bech, M.; Zaslansky, P.; Jud, C.; Liebi, M.; Guizar-Sicairos, M.; Pfeiffer, F. Six-Dimensional Real and Reciprocal Space Small-Angle X-Ray Scattering Tomography. *Nature* **2015**, *527*, 353–356.
- (340) Liebi, M.; Georgiadis, M.; Menzel, A.; Schneider, P.; Kohlbrecher, J.; Bunk, O.; Guizar-Sicairos, M. Nanostructure Surveys of Macroscopic Specimens by Small-Angle Scattering Tensor Tomography. *Nature* **2015**, *527*, 349–352.
- (341) Liebi, M.; Georgiadis, M.; Kohlbrecher, J.; Holler, M.; Raabe, J.; Usov, I.; Menzel, A.; Schneider, P.; Bunk, O.; Guizar-Sicairos, M. Small-Angle X-Ray Scattering Tensor Tomography: Model of the Three-Dimensional Reciprocal-Space Map, Reconstruction Algorithm and Angular Sampling Requirements. *Acta Crystallogr., Sect. A: Found. Adv.* **2018**, *74*, 12–24.
- (342) Conceição, A. L. C.; Perlich, J.; Haas, S.; Funari, S. S. SAXS-CT: A Nanostructure Resolving Microscopy for Macroscopic Biologic Specimens. *Biomed. Phys. Eng. Express* **2020**, *6*, 035012.
- (343) Allec, N.; Choi, M.; Yesupriya, N.; Szychowski, B.; White, M. R.; Kann, M. G.; Garcin, E. D.; Daniel, M. C.; Badano, A. Small-Angle X-Ray Scattering Method to Characterize Molecular Interactions: Proof of Concept. *Sci. Rep.* **2015**, *5*, 12085.
- (344) Hartl, C.; Frank, K.; Amenitsch, H.; Fischer, S.; Liedl, T.; Nickel, B. Position Accuracy of Gold Nanoparticles on DNA Origami Structures Studied with Small-Angle X-Ray Scattering. *Nano Lett.* **2018**, *18*, 2609–2615.
- (345) Oberdisse, J. Aggregation of Colloidal Nanoparticles in Polymer Matrices. *Soft Matter* **2006**, *2*, 29–36.
- (346) Kiesel, I.; Paulus, M.; Nase, J.; Tiemeyer, S.; Sternemann, C.; Rüster, K.; Wirkert, F. J.; Mende, K.; Büning, T.; Tolan, M. Temperature-Driven Adsorption and Desorption of Proteins at Solid–Liquid Interfaces. *Langmuir* **2014**, *30*, 2077–2083.
- (347) Evers, F.; Jeworrek, C.; Tiemeyer, S.; Weise, K.; Sellin, D.; Paulus, M.; Struth, B.; Tolan, M.; Winter, R. Elucidating the Mechanism of Lipid Membrane-Induced IAPP Fibrillogenesis and Its Inhibition by the Red Wine Compound Resveratrol: A Synchrotron X-Ray Reflectivity Study. *J. Am. Chem. Soc.* **2009**, *131*, 9516–9521.
- (348) Giri, R. P.; Mukhopadhyay, M. K.; Basak, U. K.; Chakrabarti, A.; Sanyal, M. K.; Runge, B.; Murphy, B. M. Continuous Uptake or Saturation—Investigation of Concentration and Surface-Packing-Specific Hemin Interaction with Lipid Membranes. *J. Phys. Chem. B* **2018**, *122*, 7547–7554.
- (349) Giri, R. P.; Mukhopadhyay, M. K.; Mitra, M.; Chakrabarti, A.; Sanyal, M. K.; Ghosh, S. K.; Bera, S.; Lurio, L. B.; Ma, Y.; Sinha, S. K. Differential Adsorption of a Membrane Skeletal Protein, Spectrin, in Phospholipid Membranes. *EPL* **2017**, *118*, 58002.
- (350) Basu, J. K.; Sanyal, M. K. Ordering and Growth of Langmuir–Blodgett films: X-Ray Scattering Studies. *Phys. Rep.* **2002**, *363*, 1–84.
- (351) Bhattacharyya, A.; Sanyal, M. K.; Mogera, U.; George, S. J.; Dhiman, S.; Kulkarni, G. U.; Fontaine, P. Formation of Two-Dimensional Network of Organic Charge-Transfer Complexes at the Air–Water Interface. *Langmuir* **2019**, *35*, 12630–12635.
- (352) Ke, P. C.; Lin, S.; Parak, W. J.; Davis, T. P.; Caruso, F. A Decade of the Protein Corona. *ACS Nano* **2017**, *11*, 11773–11776.
- (353) Wang, Y.; Cai, R.; Chen, C. The Nano–Bio Interactions of Nanomedicines: Understanding the Biochemical Driving Forces and Redox Reactions. *Acc. Chem. Res.* **2019**, *52*, 1507–1518.
- (354) Nel, A. E.; Madler, L.; Velegol, D.; Xia, T.; Hoek, E. M. V.; Somasundaran, P.; Klaessig, F.; Castranova, V.; Thompson, M. Understanding Biophysicochemical Interactions at the Nano-Bio Interface. *Nat. Mater.* **2009**, *8*, 543–557.
- (355) Fang, Y.; Wang, H.; Yu, H.; Liu, X.; Wang, W.; Chen, H. Y.; Tao, N. J. Plasmonic Imaging of Electrochemical Reactions of Single Nanoparticles. *Acc. Chem. Res.* **2016**, *49*, 2614–2624.
- (356) Fang, Y.; Li, Z.; Jiang, Y.; Wang, X.; Chen, H. Y.; Tao, N.; Wang, W. Intermittent Photocatalytic Activity of Single CdS Nanoparticles. *Proc. Natl. Acad. Sci. U. S. A.* **2017**, *114*, 10566–10571.
- (357) Fang, Y.; Wang, W.; Wo, X.; Luo, Y.; Yin, S.; Wang, Y.; Shan, X.; Tao, N. Plasmonic Imaging of Electrochemical Oxidation of Single Nanoparticles. *J. Am. Chem. Soc.* **2014**, *136*, 12584–12587.
- (358) Chen, Z.; Li, J.; Chen, X.; Cao, J.; Zhang, J.; Min, Q.; Zhu, J. J. Single Gold@Silver Nanoprobes for Real-Time Tracing the Entire Autophagy Process at Single-Cell Level. *J. Am. Chem. Soc.* **2015**, *137*, 1903–1908.
- (359) Xia, Y.; Xia, X.; Peng, H. C. Shape-Controlled Synthesis of Colloidal Metal Nanocrystals: Thermodynamic versus Kinetic Products. *J. Am. Chem. Soc.* **2015**, *137*, 7947–7966.
- (360) Peckys, D. B.; de Jonge, N. Visualizing Gold Nanoparticle Uptake in Live Cells with Liquid Scanning Transmission Electron Microscopy. *Nano Lett.* **2011**, *11*, 1733–1738.
- (361) Liz-Marzan, L. M.; Grzelczak, M. Growing Anisotropic Crystals at the Nanoscale. *Science* **2017**, *356*, 1120–1121.
- (362) Hirai, K.; Yeom, B.; Chang, S.-H.; Chi, H.; Mansfield, J. F.; Lee, B.; Lee, S.; Uher, C.; Kotov, N. A. Coordination Assembly of Discoid Nanoparticles. *Angew. Chem., Int. Ed.* **2015**, *54*, 8966–8970.
- (363) Choi, S.-J.; Choy, J.-H. Effect of Physico-Chemical Parameters on the Toxicity of Inorganic Nanoparticles. *J. Mater. Chem.* **2011**, *21*, 5547–5554.
- (364) Limbach, L. K.; Wick, P.; Manser, P.; Grass, R. N.; Bruinink, A.; Stark, W. J. Exposure of Engineered Nanoparticles to Human Lung Epithelial Cells: Influence of Chemical Composition and Catalytic Activity on Oxidative Stress. *Environ. Sci. Technol.* **2007**, *41*, 4158–4163.

- (365) Schön, F.; Biebl, F.; Greb, L.; Leingang, S.; Grimm-Lebsanft, B.; Teubner, M.; Buchenau, S.; Kaifer, E.; Rübhausen, M. A.; Himmel, H.-J. On the Metal Cooperativity in a Dinuclear Copper–Guanidine Complex for Aliphatic C–H Bond Cleavage by Dioxigen. *Chem. - Eur. J.* **2019**, *25*, 11257–11268.
- (366) Naumova, M.; Khakulin, D.; Rebarz, M.; Rohrmüller, M.; Dicke, B.; Biednov, M.; Britz, A.; Espinoza, S.; Grimm-Lebsanft, B.; Kloz, M.; Kretzschmar, N.; Neuba, A.; Ortmeyer, J.; Schoch, R.; Andreasson, J.; Bauer, M.; Bressler, C.; Gero Schmidt, W.; Henkel, G.; Rübhausen, M. Structural Dynamics upon Photoexcitation-Induced Charge Transfer in a Dicopper(I)–Disulfide Complex. *Phys. Chem. Chem. Phys.* **2018**, *20*, 6274–6286.
- (367) Jiang, X.; Foldbjerg, R.; Miclaus, T.; Wang, L.; Singh, R.; Hayashi, Y.; Sutherland, D.; Chen, C.; Autrup, H.; Beer, C. Multi-Platform Genotoxicity Analysis of Silver Nanoparticles in the Model Cell Line CHO-K1. *Toxicol. Lett.* **2013**, *222*, 55–63.
- (368) Xia, T.; Kovichich, M.; Liang, M.; Madler, L.; Gilbert, B.; Shi, H.; Yeh, J. I.; Zink, J. I.; Nel, A. E. Comparison of the Mechanism of Toxicity of Zinc Oxide and Cerium Oxide Nanoparticles Based on Dissolution and Oxidative Stress Properties. *ACS Nano* **2008**, *2*, 2121–2134.
- (369) Mirshafiee, V.; Sun, B.; Chang, C. H.; Liao, Y. P.; Jiang, W.; Jiang, J.; Liu, X.; Wang, X.; Xia, T.; Nel, A. E. Toxicological Profiling of Metal Oxide Nanoparticles in Liver Context Reveals Pyroptosis in Kupffer Cells and Macrophages versus Apoptosis in Hepatocytes. *ACS Nano* **2018**, *12*, 3836–3852.
- (370) Naatz, H.; Lin, S.; Li, R.; Jiang, W.; Ji, Z.; Chang, C. H.; Koser, J.; Thoming, J.; Xia, T.; Nel, A. E.; Madler, L.; Pokhrel, S. Safe-by-Design CuO Nanoparticles via Fe-Doping, Cu–O Bond Length Variation, and Biological Assessment in Cells and Zebrafish Embryos. *ACS Nano* **2017**, *11*, 501–515.
- (371) Liu, J.; Wang, P.; Zhang, X.; Wang, L.; Wang, D.; Gu, Z.; Tang, J.; Guo, M.; Cao, M.; Zhou, H.; Liu, Y.; Chen, C. Rapid Degradation and High Renal Clearance of Cu<sub>3</sub>BiS<sub>3</sub> Nanodots for Efficient Cancer Diagnosis and Photothermal Therapy *in Vivo*. *ACS Nano* **2016**, *10*, 4587–4598.
- (372) Wang, L.; Yan, L.; Liu, J.; Chen, C.; Zhao, Y. Quantification of Nanomaterial/Nanomedicine Trafficking *in Vivo*. *Anal. Chem.* **2018**, *90*, 589–614.
- (373) Gong, N.; Ma, X.; Ye, X.; Zhou, Q.; Chen, X.; Tan, X.; Yao, S.; Huo, S.; Zhang, T.; Chen, S.; Teng, X.; Hu, X.; Yu, J.; Gan, Y.; Jiang, H.; Li, J.; Liang, X.-J. Carbon-Dot-Supported Atomically Dispersed Gold as a Mitochondrial Oxidative Stress Amplifier for Cancer Treatment. *Nat. Nanotechnol.* **2019**, *14*, 379–387.
- (374) Bauer, M. HERFD-XAS and Valence-to-Core-XES: New Tools to Push the Limits in Research with Hard X-Rays? *Phys. Chem. Chem. Phys.* **2014**, *16*, 13827–13837.
- (375) Gallo, E.; Glatzel, P. Valence to Core X-Ray Emission Spectroscopy. *Adv. Mater.* **2014**, *26*, 7730–7746.
- (376) Szlachetko, J.; Nachtegaal, M.; de Boni, E.; Willmann, M.; Safonova, O.; Sa, J.; Smolentsev, G.; Szlachetko, M.; van Bokhoven, J. A.; Dousse, J. C.; Hoszowska, J.; Kayser, Y.; Jagodzinski, P.; Bergamaschi, A.; Schmitt, B.; David, C.; Lücke, A. A von Hamos X-Ray Spectrometer Based on a Segmented-Type Diffraction Crystal for Single-Shot X-Ray Emission Spectroscopy and Time-Resolved Resonant Inelastic X-Ray Scattering Studies. *Rev. Sci. Instrum.* **2012**, *83*, 103105.
- (377) Hirsch, O.; Kvashnina, K. O.; Luo, L.; Süess, M. J.; Glatzel, P.; Koziej, D. High-Energy Resolution X-Ray Absorption and Emission Spectroscopy Reveals Insight into Unique Selectivity of La-Based Nanoparticles for CO<sub>2</sub>. *Proc. Natl. Acad. Sci. U. S. A.* **2015**, *112*, 15803.
- (378) Lancaster, K. M.; Roemelt, M.; Ettenhuber, P.; Hu, Y.; Ribbe, M. W.; Neese, F.; Bergmann, U.; DeBeer, S. X-Ray Emission Spectroscopy Evidences a Central Carbon in the Nitrogenase Iron-Molybdenum Cofactor. *Science* **2011**, *334*, 974–977.
- (379) Bressler, C.; Milne, C.; Pham, V. T.; ElNahhas, A.; van der Veen, R. M.; Gawelda, W.; Johnson, S.; Beaud, P.; Grolimund, D.; Kaiser, M.; Borca, C. N.; Ingold, G.; Abela, R.; Chergui, M. Femtosecond XANES Study of the Light-Induced Spin Crossover Dynamics in an Iron(II) Complex. *Science* **2009**, *323*, 489–492.
- (380) Sikora, M.; Juhin, A.; Weng, T.-C.; Saintavit, P.; Detlefs, C.; de Groot, F.; Glatzel, P. Strong K-Edge Magnetic Circular Dichroism Observed in Photon-In–Photon-Out Spectroscopy. *Phys. Rev. Lett.* **2010**, *105*, 037202.
- (381) Daffé, N.; Sikora, M.; Bouldi, N.; Gavrilov, V.; Neveu, S.; Choueikani, F.; Ohresser, P.; Dupuis, V.; Taverna, D.; Gloter, A.; Arrio, M.-A.; Saintavit, P.; Juhin, A. Nanoscale Distribution of Magnetic Anisotropies in Bimagnetic Soft Core–Hard Shell MnFe<sub>2</sub>O<sub>4</sub>@CoFe<sub>2</sub>O<sub>4</sub> Nanoparticles. *Adv. Mater. Interfaces* **2017**, *4*, 1700599.
- (382) Kuciakowski, J.; Kmita, A.; Lachowicz, D.; Wyrwal-Sarna, M.; Pitala, K.; Lafuerza, S.; Koziej, D.; Juhin, A.; Sikora, M. Selective Magnetometry of Superparamagnetic Iron Oxide Nanoparticles in Liquids. *Nanoscale* **2020**, *12*, 16420–16426.
- (383) Liu, B.; van Schooneveld, M. M.; Cui, Y.-T.; Miyawaki, J.; Harada, Y.; Eschemann, T. O.; de Jong, K. P.; Delgado-Jaime, M. U.; de Groot, F. M. F. *In-Situ* 2p3d Resonant Inelastic X-Ray Scattering Tracking Cobalt Nanoparticle Reduction. *J. Phys. Chem. C* **2017**, *121*, 17450–17456.
- (384) Penfold, T. J.; Szlachetko, J.; Santomauro, F. G.; Britz, A.; Gawelda, W.; Doumy, G.; March, A. M.; Southworth, S. H.; Rittmann, J.; Abela, R.; Chergui, M.; Milne, C. J. Revealing Hole Trapping in Zinc Oxide Nanoparticles by Time-Resolved X-Ray Spectroscopy. *Nat. Commun.* **2018**, *9*, 478.
- (385) Szlachetko, J.; Kubas, A.; Cieślak, A. M.; Sokołowski, K.; Mąkowski, Ł.; Czapla-Masztafiak, J.; Sá, J.; Lewiński, J. Hidden Gapless States during Thermal Transformations of Preorganized Zinc Alkoxides to Zinc Oxide Nanocrystals. *Mater. Horiz.* **2018**, *5*, 905–911.
- (386) Kayser, Y.; Milne, C.; Juranić, P.; Sala, L.; Czapla-Masztafiak, J.; Follath, R.; Kavčič, M.; Knopp, G.; Rehanek, J.; Blachucki, W.; Delcey, M. G.; Lundberg, M.; Tyrälä, K.; Zhu, D.; Alonso-Mori, R.; Abela, R.; Sá, J.; Szlachetko, J. Core-Level Nonlinear Spectroscopy Triggered by Stochastic X-Ray Pulses. *Nat. Commun.* **2019**, *10*, 4761.
- (387) Krause, M. O. Atomic Radiative and Radiationless Yields for K and L Shells. *J. Phys. Chem. Ref. Data* **1979**, *8*, 307–327.
- (388) Veith, L.; Böttner, J.; Vennemann, A.; Breitenstein, D.; Engelhard, C.; Meijer, J.; Estrela-Lopis, I.; Wiemann, M.; Hagenhoff, B. Detection of ZrO<sub>2</sub> Nanoparticles in Lung Tissue Sections by Time-of-Flight Secondary Ion Mass Spectrometry and Ion Beam Microscopy. *Nanomaterials* **2018**, *8*, 44.
- (389) Turco, A.; Moglianetti, M.; Corvaglia, S.; Rella, S.; Catelani, T.; Marotta, R.; Malitesta, C.; Pompa, P. P. Sputtering-Enabled Intracellular X-Ray Photoelectron Spectroscopy: A Versatile Method to Analyze the Biological Fate of Metal Nanoparticles. *ACS Nano* **2018**, *12*, 7731–7740.
- (390) Sutton, M.; Mochrie, S. G. J.; Greytak, T.; Nagler, S. E.; Berman, L. E.; Held, G. A.; Stephenson, G. B. Observation of Speckle by Diffraction with Coherent X-Rays. *Nature* **1991**, *352*, 608–610.
- (391) Westermeier, F.; Autenrieth, T.; Gutt, C.; Leupold, O.; Duri, A.; Menzel, A.; Johnson, I.; Broennimann, C.; Grubel, G. Fast Two-Dimensional Detection for X-Ray Photon Correlation Spectroscopy Using the PILATUS Detector. *J. Synchrotron Radiat.* **2009**, *16*, 687–689.
- (392) Fluerasu, A.; Moussaid, A.; Falus, P.; Gleyzolle, H.; Madsen, A. X-Ray Photon Correlation Spectroscopy under Flow. *J. Synchrotron Radiat.* **2008**, *15*, 378–384.
- (393) Busch, S.; Jensen, T. H.; Chushkin, Y.; Fluerasu, A. Dynamics in Shear Flow Studied by X-Ray Photon Correlation Spectroscopy. *Eur. Phys. J. E: Soft Matter Biol. Phys.* **2008**, *26*, 55–62.
- (394) Hruszkewycz, S. O.; Sutton, M.; Fuoss, P. H.; Adams, B.; Rosenkranz, S.; Ludwig, K. F., Jr.; Roseker, W.; Fritz, D.; Cammarata, M.; Zhu, D.; Lee, S.; Lemke, H.; Gutt, C.; Robert, A.; Grubel, G.; Stephenson, G. B. High Contrast X-Ray Speckle

from Atomic-Scale Order in Liquids and Glasses. *Phys. Rev. Lett.* **2012**, *109*, 185502.

(395) Verwohlt, J.; Reiser, M.; Randolph, L.; Matic, A.; Medina, L. A.; Madsen, A.; Sprung, M.; Zozulya, A.; Gutt, C. Low Dose X-Ray Speckle Visibility Spectroscopy Reveals Nanoscale Dynamics in Radiation Sensitive Ionic Liquids. *Phys. Rev. Lett.* **2018**, *120*, 168001.

(396) Shpyrko, O. G. X-Ray Photon Correlation Spectroscopy. *J. Synchrotron Radiat.* **2014**, *21*, 1057–1064.

(397) Bandyopadhyay, R.; Liang, D.; Harden, J. L.; Leheny, R. L. Slow Dynamics, Aging, and Glassy Rheology in Soft and Living Matter. *Solid State Commun.* **2006**, *139*, 589–598.

(398) Jain, A.; Schulz, F.; Lokteva, I.; Frenzel, L.; Grübel, G.; Lehmkuhler, F. Anisotropic and Heterogeneous Dynamics in an Aging Colloidal Gel. *Soft Matter* **2020**, *16*, 2864–2872.

(399) Möller, J.; Sprung, M.; Madsen, A.; Gutt, C. X-Ray Photon Correlation Spectroscopy of Protein Dynamics at Nearly Diffraction-Limited Storage Rings. *IUCrJ* **2019**, *6*, 794–803.

(400) Lehmkuhler, F.; Valerio, J.; Sheyfer, D.; Roseker, W.; Schroer, M. A.; Fischer, B.; Tono, K.; Yabashi, M.; Ishikawa, T.; Grübel, G. Dynamics of Soft Nanoparticle Suspensions at Hard X-Ray FEL Sources below the Radiation-Damage Threshold. *IUCrJ* **2018**, *5*, 801–807.

(401) Kang, T.; Tran, T. T.-T.; Park, C.; Lee, B.-J. Biomimetic Shear Stress and Nanoparticulate Drug Delivery. *J. Pharm. Invest.* **2017**, *47*, 133–139.

(402) Holme, M. N.; Fedotenko, I. A.; Abegg, D.; Althaus, J.; Babel, L.; Favarger, F.; Reiter, R.; Tanasescu, R.; Zaffalon, P.-L.; Ziegler, A.; Müller, B.; Saxer, T.; Zumbuehl, A. Shear-Stress Sensitive Lenticular Vesicles for Targeted Drug Delivery. *Nat. Nanotechnol.* **2012**, *7*, 536–543.

(403) Saxer, T.; Zumbuehl, A.; Müller, B. The Use of Shear Stress for Targeted Drug Delivery. *Cardiovasc. Res.* **2013**, *99*, 328–333.

(404) Epshtein, M.; Korin, N. Shear Targeted Drug Delivery to Stenotic Blood Vessels. *J. Biomech.* **2017**, *50*, 217–221.

(405) Korin, N.; Kanapathipillai, M.; Matthews, B. D.; Crescente, M.; Brill, A.; Mammoto, T.; Ghosh, K.; Jurek, S.; Bencherif, S. A.; Bhatta, D.; Coskun, A. U.; Feldman, C. L.; Wagner, D. D.; Ingber, D. E. Shear-Activated Nanotherapeutics for Drug Targeting to Obstructed Blood Vessels. *Science* **2012**, *337*, 738–742.

(406) Nazareus, M.; Zhang, Q.; Soliman, M. G.; del Pino, P.; Pelaz, B.; Carregal-Romero, S.; Rejman, J.; Rothen-Ruthishauser, B.; Clift, M. J. D.; Zellner, R.; Nienhaus, G. U.; Delehanty, J. B.; Medintz, I. L.; Parak, W. J. *In Vitro* Interaction of Colloidal Nanoparticles with Mammalian Cells: What Have We Learned Thus Far? *Beilstein J. Nanotechnol.* **2014**, *5*, 1477–1490.

(407) Bera, P. K.; Kandari, A. K.; Krishnaswamy, R.; Fontaine, P.; Impéror-Clerc, M.; Pansu, B.; Constantin, D.; Maiti, S.; Sanyal, M. K.; Sood, A. K. Grazing Incidence X-Ray Diffraction Studies of Lipid–Peptide Mixed Monolayers during Shear Flow. *ACS Omega* **2020**, *5*, 14555–14563.

(408) Segura-Ruiz, J.; Martínez-Criado, G.; Chu, M. H.; Geburt, S.; Ronning, C. Nano-X-Ray Absorption Spectroscopy of Single Co-Implanted ZnO Nanowires. *Nano Lett.* **2011**, *11*, 5322–5326.

(409) Segura-Ruiz, J.; Martínez-Criado, G.; Chu, M. H.; Denker, C.; Malindretos, J.; Rizzi, A. Synchrotron Nanoimaging of Single In-Rich InGa<sub>N</sub> nanowires. *J. Appl. Phys.* **2013**, *113*, 136511.

(410) Kuzmin, A.; Chaboy, J. EXAFS and XANES Analysis of Oxides at the Nanoscale. *IUCrJ* **2014**, *1*, 571–589.

(411) Martínez-Criado, G.; Homs, A.; Alén, B.; Sans, J. A.; Segura-Ruiz, J.; Molina-Sánchez, A.; Susini, J.; Yoo, J.; Yi, G.-C. Probing Quantum Confinement within Single Core–Multishell Nanowires. *Nano Lett.* **2012**, *12*, 5829–5834.

(412) Segura-Ruiz, J.; Martínez-Criado, G.; Denker, C.; Malindretos, J.; Rizzi, A. Phase Separation in Single In<sub>x</sub>Ga<sub>1-x</sub>N Nanowires Revealed through a Hard X-Ray Synchrotron Nanoprobe. *Nano Lett.* **2014**, *14*, 1300–1305.

(413) James, S. A.; Feltis, B. N.; de Jonge, M. D.; Sridhar, M.; Kimpton, J. A.; Altissimo, M.; Mayo, S.; Zheng, C.; Hastings, A.; Howard, D. L.; Paterson, D. J.; Wright, P. F. A.; Moorhead, G. F.;

Turney, T. W.; Fu, J. Quantification of ZnO Nanoparticle Uptake, Distribution, and Dissolution within Individual Human Macrophages. *ACS Nano* **2013**, *7*, 10621–10635.

(414) Boesenberg, U.; Ryan, C. G.; Kirkham, R.; Siddons, D. P.; Alfeld, M.; Garrevoet, J.; Nunez, T.; Claussen, T.; Kracht, T.; Falkenberg, G. Fast X-Ray Microfluorescence Imaging with Submicrometer-Resolution Integrating a Maia Detector at Beamline P06 at PETRA III. *J. Synchrotron Radiat.* **2016**, *23*, 1550–1560.

(415) Etschmann, B. E.; Ryan, C. G.; Brugger, J.; Kirkham, R.; Hough, R. M.; Moorhead, G.; Siddons, D. P.; De Geronimo, G.; Kuczewski, A.; Dunn, P.; Paterson, D.; de Jonge, M. D.; Howard, D. L.; Davey, P.; Jensen, M. Reduced As Components in Highly Oxidized Environments: Evidence from Full Spectral XANES Imaging Using the Maia Massively Parallel Detector. *Am. Mineral.* **2010**, *95*, 884–887.

(416) Ryan, C. G.; Siddons, D. P.; Kirkham, R.; Dunn, P. A.; Kuczewski, A.; Moorhead, G.; De Geronimo, G.; Paterson, D. J.; de Jonge, M. D.; Hough, R. M.; Lintern, M. J.; Howard, D. L.; Kappen, P.; Cleverley, J.; et al. The New Maia Detector System: Methods for High Definition Trace Element Imaging of Natural Material. *AIP Conf. Proc.* **2009**, *1221*, 9–17.

(417) De Samber, B.; Scharf, O.; Buzanich, G.; Garrevoet, J.; Tack, P.; Radtke, M.; Riesemeier, H.; Reinholz, U.; Evens, R.; De Schampelaere, K.; Falkenberg, G.; Janssen, C.; Vincze, L. Three-Dimensional X-Ray Fluorescence Imaging Modes for Biological Specimens Using a Full-Field Energy Dispersive CCD Camera. *J. Anal. At. Spectrom.* **2019**, *34*, 2083–2093.

(418) Chen, W.; DeGeronimo, G.; Elliott, D.; Giacomini, G.; Kuczewski, A. J.; Mead, J.; Pinelli, D.; Rumaiz, A. K.; Siddons, D. P.; Smith, G.; Vernon, E. O. A New Prototype X-Ray Fluorescence Detector System with Silicon Drift Detector Array. Proceedings from the 2016 IEEE Nuclear Science Symposium, Medical Imaging Conference and Room-Temperature Semiconductor Detector Workshop (NSS/MIC/RTSD), October 29–November 6, 2016, Strasbourg, France; IEEE: New York, 2016; pp 1–3.

(419) IARC Classifies Radiofrequency Electromagnetic Fields as Possibly Carcinogenic to Humans. *Press Release No. 208*; International Agency for Research on Cancer: Lyon, France, 2011. [https://www.iarc.fr/wp-content/uploads/2018/07/pr208\\_E.pdf](https://www.iarc.fr/wp-content/uploads/2018/07/pr208_E.pdf) (accessed 2020-06-16).

(420) Cuttler, J. M. Evidence of a Dose Threshold for Radiation-Induced Leukemia. *Dose-Response* **2018**, *16*, 1559325818811537.

(421) Little, M. P.; Wakeford, R.; Borrego, D.; French, B.; Zablotska, L. B.; Adams, M. J.; Allodji, R.; de Vathaire, F.; Lee, C.; Brenner, A. V.; Miller, J. S.; Campbell, D.; Pearce, M. S.; Doody, M. M.; Holmberg, E.; Lundell, M.; Sadetzki, S.; Linet, M. S.; Berrington de González, A. Leukaemia and Myeloid Malignancy among People Exposed to Low Doses (<100 mSv) of Ionising Radiation during Childhood: A Pooled Analysis of Nine Historical Cohort Studies. *Lancet Haematol.* **2018**, *5*, e346–e358.

(422) Brooks, A. L.; Hoel, D. G.; Preston, R. J. The Role of Dose Rate in Radiation Cancer Risk: Evaluating the Effect of Dose Rate at the Molecular, Cellular and Tissue Levels Using Key Events in Critical Pathways Following Exposure to Low LET Radiation. *Int. J. Radiat. Biol.* **2016**, *92*, 405–426.

(423) de González, A. B.; Darby, S. Risk of Cancer from Diagnostic X-Rays: Estimates for the UK and 14 Other Countries. *Lancet* **2004**, *363*, 345–351.

(424) Pearce, M. S.; Salotti, J. A.; Little, M. P.; McHugh, K.; Lee, C.; Kim, K. P.; Howe, N. L.; Ronckers, C. M.; Rajaraman, P.; Craft, A. W.; Parker, L.; Berrington de González, A. Radiation Exposure from CT Scans in Childhood and Subsequent Risk of Leukaemia and Brain Tumours: A Retrospective Cohort Study. *Lancet* **2012**, *380*, 499–505.

(425) Boffetta, P.; Mannetje, A. t.; Zaridze, D.; Szeszenia-Dabrowska, N.; Rudnai, P.; Lissowska, J.; Fabianová, E.; Mates, D.; Bencko, V.; Navratilova, M.; Janout, V.; Cardis, E.; Fevotte, J.; Fletcher, T.; Brennan, P. Occupational X-Ray Examinations and Lung Cancer Risk. *Int. J. Cancer* **2005**, *115*, 263–267.

- (426) McBride, W. H.; Schae, D. Radiation-Induced Tissue Damage and Response. *J. Pathol.* **2020**, *250*, 647–655.
- (427) Geleijns, J.; Wondergem, J. X-Ray Imaging and the Skin: Radiation Biology, Patient Dosimetry and Observed Effects. *Radiat. Prot. Dosim.* **2005**, *114*, 121–125.
- (428) Koike, M.; Sugasawa, J.; Koike, A.; Kohno, Y. p53 Phosphorylation in Mouse Skin and *in Vitro* Human Skin Model by High-Dose-Radiation Exposure. *J. Radiat. Res.* **2005**, *46*, 461–468.
- (429) Kumar, S.; Kolozsvary, A.; Kohl, R.; Lu, M.; Brown, S.; Kim, J. H. Radiation-Induced Skin Injury in the Animal Model of Scleroderma: Implications for Post-Radiotherapy Fibrosis. *Radiat. Oncol.* **2008**, *3*, 40.
- (430) Zhai, J.; He, F.; Wang, J.; Chen, J.; Tong, L.; Zhu, G. Influence of Radiation Exposure Pattern on the Bone Injury and Osteoclastogenesis in a Rat Model. *Int. J. Mol. Med.* **2019**, *44*, 2265–2275.
- (431) Zhang, J.; Jiang, J.; Huang, R.; Wang, Y.; Nie, X.; Gui, R. Circular RNA Expression Profiles Are Significantly Altered in Mice Bone Marrow Stromal Cells After Total Body Irradiation. *Leuk. Res.* **2018**, *70*, 67–73.
- (432) Künzle, M.; Eckert, T.; Beck, T. Binary Protein Crystals for the Assembly of Inorganic Nanoparticle Superlattices. *J. Am. Chem. Soc.* **2016**, *138*, 12731–12734.
- (433) Garman, E. F.; Weik, M. X-Ray Radiation Damage to Biological Samples: Recent Progress. *J. Synchrotron Radiat.* **2019**, *26*, 907–911.
- (434) Garman, E. Radiation Damage in Macromolecular Crystallography: What Is It and Why Should We Care? *Acta Crystallogr., Sect. D: Biol. Crystallogr.* **2010**, *66*, 339–351.
- (435) Holton, J. A Beginner's Guide to Radiation Damage. *J. Synchrotron Radiat.* **2009**, *16*, 133–142.
- (436) Owen, R. L.; Rudiño-Piñera, E.; Garman, E. F. Experimental Determination of the Radiation Dose Limit for Cryocooled Protein Crystals. *Proc. Natl. Acad. Sci. U. S. A.* **2006**, *103*, 4912–4917.
- (437) Axnanda, S.; Crumlin, E. J.; Mao, B.; Rani, S.; Chang, R.; Karlsson, P. G.; Edwards, M. O. M.; Lundqvist, M.; Moberg, R.; Ross, P.; Hussain, Z.; Liu, Z. Using “Tender” X-Ray Ambient Pressure X-Ray Photoelectron Spectroscopy as a Direct Probe of Solid-Liquid Interface. *Sci. Rep.* **2015**, *5*, 9788.
- (438) Ebrahim, A.; Moreno-Chicano, T.; Appleby, M. V.; Chaplin, A. K.; Beale, J. H.; Sherrell, D. A.; Duyvesteyn, H. M. E.; Owada, S.; Tono, K.; Sugimoto, H.; Strange, R. W.; Worrall, J. A. R.; Axford, D.; Owen, R. L.; Hough, M. A. Dose-Resolved Serial Synchrotron and XFEL Structures of Radiation-Sensitive Metalloproteins. *IUCr* **2019**, *6*, 543–551.
- (439) Kirz, J.; Jacobsen, C.; Howells, M. Soft X-Ray Microscopes and Their Biological Applications. *Q. Rev. Biophys.* **1995**, *28*, 33–130.
- (440) Cazaux, J. A Physical Approach to the Radiation Damage Mechanisms Induced by X-Rays in X-Ray Microscopy and Related Techniques. *J. Microsc.* **1997**, *188*, 106–124.
- (441) Teng, T.-Y.; Moffat, K. Radiation Damage of Protein Crystals at Cryogenic Temperatures between 40 and 150 K. *J. Synchrotron Radiat.* **2002**, *9*, 198–201.
- (442) Rose, A. A Unified Approach to the Performance of Photographic Film, Television Pickup Tubes, and the Human Eye. *J. Soc. Motion Pict. Eng.* **1946**, *47*, 273–294.
- (443) Howells, M. R.; Beetz, T.; Chapman, H. N.; Cui, C.; Holton, J. M.; Jacobsen, C. J.; Kirz, J.; Lima, E.; Marchesini, S.; Miao, H.; Sayre, D.; Shapiro, D. A.; Spence, J. C. H.; Starodub, D. M. An Assessment of the Resolution Limitation Due to Radiation-Damage in X-Ray Diffraction Microscopy. *J. Electron Spectrosc. Relat. Phenom.* **2009**, *170*, 4–12.
- (444) Henderson, R. The Potential and Limitations of Neutrons, Electrons and X-Rays for Atomic Resolution Microscopy of Unstained Biological Molecules. *Q. Rev. Biophys.* **1995**, *28*, 171–193.
- (445) Skarsgard, L. D.; Harrison, I.; Durand, R. E. The Radiation Response of Asynchronous Cells at Low Dose: Evidence of Substructure. *Radiat. Res.* **1991**, *127*, 248–56.
- (446) Fayard, B.; Salomé, M.; Takemoto, K.; Kihara, H.; Susini, J. Some Practical Considerations About the Effects of Radiation Damage on Hydrated Cells Imaged by X-Ray Fluorescence Microscopy. *J. Electron Spectrosc. Relat. Phenom.* **2009**, *170*, 19–24.
- (447) Williams, S.; Zhang, X.; Jacobsen, C.; Kirz, J.; Lindaas, S.; Van'T Hof, J.; Lamm, S. S. Measurements of Wet Metaphase Chromosomes in the Scanning Transmission X-Ray Microscope. *J. Microsc.* **1993**, *170*, 155–165.
- (448) Kempner, E. S.; Wood, R.; Salovey, R. The Temperature Dependence of Radiation Sensitivity of Large Molecules. *J. Polym. Sci., Part B: Polym. Phys.* **1986**, *24*, 2337–2343.
- (449) Hope, H. Crystallography of Biological Macromolecules at Ultra-Low Temperature. *Annu. Rev. Biophys. Biophys. Chem.* **1990**, *19*, 107–126.
- (450) Teng, T.-y.; Moffat, K. Primary Radiation Damage of Protein Crystals by an Intense Synchrotron X-Ray Beam. *J. Synchrotron Radiat.* **2000**, *7*, 313–317.
- (451) Schneider, G. Cryo X-Ray Microscopy with High Spatial Resolution in Amplitude and Phase Contrast. *Ultramicroscopy* **1998**, *75*, 85–104.
- (452) Kanngießler, B.; Malzer, W.; Pagels, M.; Lühl, L.; Weseloh, G. Three-Dimensional Micro-XRF under Cryogenic Conditions: A Pilot Experiment for Spatially Resolved Trace Analysis in Biological Specimens. *Anal. Bioanal. Chem.* **2007**, *389*, 1171–1176.
- (453) Chen, S.; Deng, J.; Yuan, Y.; Flachenecker, C.; Mak, R.; Hornberger, B.; Jin, Q.; Shu, D.; Lai, B.; Maser, J.; Roehrig, C.; Paunesku, T.; Gleber, S. C.; Vine, D. J.; Finney, L.; VonOsinski, J.; Bolbat, M.; Spink, I.; Chen, Z.; Steele, J.; et al. The Bionanoprobe: Hard X-Ray Fluorescence Nanoprobe with Cryogenic Capabilities. *J. Synchrotron Radiat.* **2014**, *21*, 66–75.
- (454) De Samber, B.; Meul, E.; Laforce, B.; De Paepe, B.; Smet, J.; De Bruyne, M.; De Rycke, R.; Bohic, S.; Cloetens, P.; Van Coster, R.; Vandenabeele, P.; Vanden Bergh, T. Nanoscopic X-Ray Fluorescence Imaging and Quantification of Intracellular Key-Elements in Cryofrozen Friedreich's Ataxia Fibroblasts. *PLoS One* **2018**, *13*, e0190495.
- (455) Rothkamm, K.; Löbrich, M. Evidence for a Lack of DNA Double-Strand Break Repair in Human Cells Exposed to Very Low X-Ray Doses. *Proc. Natl. Acad. Sci. U. S. A.* **2003**, *100*, 5057–5062.
- (456) Zhao, Y.; Zhong, R.; Sun, L.; Jia, J.; Ma, S.; Liu, X. Ionizing Radiation-Induced Adaptive Response in Fibroblasts under Both Monolayer and 3-Dimensional Conditions. *PLoS One* **2015**, *10*, e0121289.
- (457) Murray, D.; Mirzayans, R.; McBride, W. H. Defenses Against Pro-Oxidant Forces - Maintenance of Cellular and Genomic Integrity and Longevity. *Radiat. Res.* **2018**, *190*, 331–349.
- (458) Schae, D.; Micewicz, E. D.; Ratikan, J. A.; Xie, M. W.; Cheng, G.; McBride, W. H. Radiation and Inflammation. *Semin. Radiat. Oncol.* **2015**, *25*, 4–10.
- (459) Rodriguez-Ruiz, M. E.; Vitale, I.; Harrington, K. J.; Melero, I.; Galluzzi, L. Immunological Impact of Cell Death Signaling Driven by Radiation on the Tumor Microenvironment. *Nat. Immunol.* **2020**, *21*, 120–134.
- (460) McKelvey, K. J.; Hudson, A. L.; Back, M.; Eade, T.; Diakos, C. I. Radiation, Inflammation and the Immune Response in Cancer. *Mamm. Genome* **2018**, *29*, 843–865.
- (461) Azzam, E. I.; Jay-Gerin, J.-P.; Pain, D. Ionizing Radiation-Induced Metabolic Oxidative Stress and Prolonged Cell Injury. *Cancer Lett.* **2012**, *327*, 48–60.
- (462) Venkatesulu, B. P.; Mahadevan, L. S.; Aliru, M. L.; Yang, X.; Bodd, M. H.; Singh, P. K.; Yusuf, S. W.; Abe, J.-i.; Krishnan, S. Radiation-Induced Endothelial Vascular Injury: A Review of Possible Mechanisms. *J. Am. Coll. Cardiol. Basic Trans. Science* **2018**, *3*, 563–572.
- (463) Smith, T. A.; Kirkpatrick, D. R.; Smith, S.; Smith, T. K.; Pearson, T.; Kailasam, A.; Herrmann, K. Z.; Schubert, J.; Agrawal,

- D. K. Radioprotective Agents to Prevent Cellular Damage Due to Ionizing Radiation. *J. Transl. Med.* **2017**, *15*, 232.
- (464) Liu, Y.; Zhang, P.; Li, F.; Jin, X.; Li, J.; Chen, W.; Li, Q. Metal-Based NanoEnhancers for Future Radiotherapy: Radiosensitizing and Synergistic Effects on Tumor Cells. *Theranostics* **2018**, *8*, 1824–1849.
- (465) Bonvalot, S.; Rutkowski, P. L.; Thariat, J.; Carrère, S.; Ducassou, A.; Sunyach, M.-P.; Agoston, P.; Hong, A.; Mervoyer, A.; Rastrelli, M.; Moreno, V.; Li, R. K.; Tiangco, B.; Herraes, A. C.; Gronchi, A.; Mangel, L.; Sy-Ortin, T.; Hohenberger, P.; de Baère, T.; Le Cesne, A.; et al. NBTXR3, a First-in-Class Radioenhancer Hafnium Oxide Nanoparticle, Plus Radiotherapy versus Radiotherapy Alone in Patients with Locally Advanced Soft-Tissue Sarcoma (Act. In. Sarc): A Multicentre, Phase 2–3, Randomised, Controlled Trial. *Lancet Oncol.* **2019**, *20*, 1148–1159.
- (466) Manohar, N.; Reynoso, F. J.; Diagaradjane, P.; Krishnan, S.; Cho, S. H. Quantitative Imaging of Gold Nanoparticle Distribution in a Tumor-Bearing Mouse Using Benchtop X-Ray Fluorescence Computed Tomography. *Sci. Rep.* **2016**, *6*, 22079.
- (467) Gilbert, B.; Fakra, S. C.; Xia, T.; Pokhrel, S.; Madler, L.; Nel, A. E. The Fate of ZnO Nanoparticles Administered to Human Bronchial Epithelial Cells. *ACS Nano* **2012**, *6*, 4921–4930.
- (468) Unrine, J. M.; Tsyusko, O. V.; Hunyadi, S. E.; Judy, J. D.; Bertsch, P. M. Effects of Particle Size on Chemical Speciation and Bioavailability of Copper to Earthworms (*Eisenia fetida*) Exposed to Copper Nanoparticles. *J. Environ. Qual.* **2010**, *39*, 1942–1953.
- (469) Richardson, J. J.; Liang, K. Nano-Biohybrids: *In Vivo* Synthesis of Metal–Organic Frameworks inside Living Plants. *Small* **2018**, *14*, 1702958.
- (470) Wang, S.; Lv, J.; Ma, J.; Zhang, S. Cellular Internalization and Intracellular Biotransformation of Silver Nanoparticles in *Chlamydomonas reinhardtii*. *Nanotoxicology* **2016**, *10*, 1129–1135.
- (471) Sabo-Attwood, T.; Unrine, J. M.; Stone, J. W.; Murphy, C. J.; Ghoshroy, S.; Blom, D.; Bertsch, P. M.; Newman, L. A. Uptake, Distribution and Toxicity of Gold Nanoparticles in Tobacco (*Nicotiana xanthi*) Seedlings. *Nanotoxicology* **2012**, *6*, 353–360.
- (472) Eggl, E.; Dierolf, M.; Achterhold, K.; Jud, C.; Gunther, B.; Braig, E.; Gleich, B.; Pfeiffer, F. The Munich Compact Light Source: Initial Performance Measures. *J. Synchrotron Radiat.* **2016**, *23*, 1137–1142.
- (473) Hornberger, B.; Kasahara, J.; Gifford, M.; Ruth, R.; Loewen, R. A Compact Light Source Providing High-Flux, Quasi-Monochromatic, Tunable X-Rays in the Laboratory. *Proc. SPIE* **2019**, *11110*, 1111003.
- (474) Eggl, E.; Schleede, S.; Bech, M.; Achterhold, K.; Loewen, R.; Ruth, R. D.; Pfeiffer, F. X-Ray Phase-Contrast Tomography with a Compact Laser-Driven Synchrotron Source. *Proc. Natl. Acad. Sci. U. S. A.* **2015**, *112*, 5567–5572.
- (475) Huang, J.; Günther, B.; Achterhold, K.; Cui, Y.-t.; Gleich, B.; Dierolf, M.; Pfeiffer, F. Energy-Dispersive X-Ray Absorption Spectroscopy with an Inverse Compton Source. *Sci. Rep.* **2020**, *10*, 8772.
- (476) Yaroshenko, A.; Pritzke, T.; Koschlig, M.; Kamgari, N.; Willer, K.; Gromann, L.; Auweter, S.; Hellbach, K.; Reiser, M.; Eickelberg, O.; Pfeiffer, F.; Hilgendorff, A. Visualization of Neonatal Lung Injury Associated with Mechanical Ventilation Using X-Ray Dark-Field Radiography. *Sci. Rep.* **2016**, *6*, 24269.
- (477) Yaroshenko, A.; Hellbach, K.; Yildirim, A. Ö.; Conlon, T. M.; Fernandez, I. E.; Bech, M.; Velroyen, A.; Meinel, F. G.; Auweter, S.; Reiser, M.; Eickelberg, O.; Pfeiffer, F. Improved *In Vivo* Assessment of Pulmonary Fibrosis in Mice Using X-Ray Dark-Field Radiography. *Sci. Rep.* **2015**, *5*, 17492.
- (478) Bech, M.; Tapfer, A.; Velroyen, A.; Yaroshenko, A.; Pauwels, B.; Hostens, J.; Bruyndonckx, P.; Sasov, A.; Pfeiffer, F. *In-Vivo* Dark-Field and Phase-Contrast X-Ray Imaging. *Sci. Rep.* **2013**, *3*, 3209.
- (479) Gromann, L. B.; De Marco, F.; Willer, K.; Noël, P. B.; Scherer, K.; Renger, B.; Gleich, B.; Achterhold, K.; Fingerle, A. A.; Muenzel, D.; Auweter, S.; Hellbach, K.; Reiser, M.; Baehr, A.; Dmochewitz, M.; Schroeter, T. J.; Koch, F. J.; Meyer, P.; Kunka, D.; Mohr, J.; et al. *In Vivo* X-Ray Dark-Field Chest Radiography of a Pig. *Sci. Rep.* **2017**, *7*, 4807.
- (480) David, C.; Nöhhammer, B.; Solak, H. H.; Ziegler, E. Differential X-Ray Phase Contrast Imaging Using a Shearing Interferometer. *Appl. Phys. Lett.* **2002**, *81*, 3287–3289.
- (481) Momose, A.; Kawamoto, S.; Koyama, I.; Hamaishi, Y.; Takai, K.; Suzuki, Y. Demonstration of X-Ray Talbot Interferometry. *Jpn. J. Appl. Phys.* **2003**, *42*, L866–L868.
- (482) Pfeiffer, F.; Weitkamp, T.; Bunk, O.; David, C. Phase Retrieval and Differential Phase-Contrast Imaging with Low-Brilliance X-Ray Sources. *Nat. Phys.* **2006**, *2*, 258–261.
- (483) Pfeiffer, F.; Bech, M.; Bunk, O.; Kraft, P.; Eikenberry, E. F.; Brönnimann, C.; Grünzweig, C.; David, C. Hard-X-Ray Dark-Field Imaging Using a Grating Interferometer. *Nat. Mater.* **2008**, *7*, 134–137.
- (484) Willer, K.; Fingerle, A. A.; Gromann, L. B.; De Marco, F.; Herzen, J.; Achterhold, K.; Gleich, B.; Muenzel, D.; Scherer, K.; Renz, M.; Renger, B.; Kopp, F.; Kriner, F.; Fischer, F.; Braun, C.; Auweter, S.; Hellbach, K.; Reiser, M. F.; Schroeter, T.; Mohr, J. X-Ray Dark-Field Imaging of the Human Lung—A Feasibility Study on a Deceased Body. *PLoS One* **2018**, *13*, e0204565.
- (485) Sauter, A. P.; Andrejewski, J.; De Marco, F.; Willer, K.; Gromann, L. B.; Noichl, W.; Kriner, F.; Fischer, F.; Braun, C.; Koehler, T.; Meurer, F.; Fingerle, A. A.; Pfeiffer, D.; Rummeny, E.; Herzen, J.; Pfeiffer, F. Optimization of Tube Voltage in X-Ray Dark-Field Radiography. *Sci. Rep.* **2019**, *9*, 8699.
- (486) Köcher, S.; Beyer, B.; Lange, T.; Nordquist, L.; Volquardsen, J.; Burdak-Rothkamm, S.; Schlomm, T.; Petersen, C.; Rothkamm, K.; Mansour, W. Y. A Functional *ex Vivo* Assay to Detect PARP1-EJ Repair and Radiosensitization by PARP-Inhibitor in Prostate Cancer. *Int. J. Cancer* **2019**, *144*, 1685–1696.
- (487) Xu, X.; Farach-Carson, M. C.; Jia, X. Three-Dimensional *In Vitro* Tumor Models for Cancer Research and Drug Evaluation. *Biotechnol. Adv.* **2014**, *32*, 1256–1268.
- (488) Peroglio, M.; Gaspar, D.; Zeugolis, D. I.; Alini, M. Relevance of Bioreactors and Whole Tissue Cultures for the Translation of New Therapies to Humans. *J. Orthop. Res.* **2018**, *36*, 10–21.
- (489) Stewart, B.; Wild, C. *World Cancer Report 2014*; International Agency for Research on Cancer: Lyon, France, 2014.
- (490) El-Gabalawy, H.; Guenther, L. C.; Bernstein, C. N. Epidemiology of Immune-Mediated Inflammatory Diseases: Incidence, Prevalence, Natural History, and Comorbidities. *J. Rheumatol., Suppl.* **2010**, *85*, 2–10.
- (491) Molodecky, N. A.; Soon, I. S.; Rabi, D. M.; Ghali, W. A.; Ferris, M.; Chernoff, G.; Benchimol, E. I.; Panaccione, R.; Ghosh, S.; Barkema, H. W.; Kaplan, G. G. Increasing Incidence and Prevalence of the Inflammatory Bowel Diseases with Time, Based on Systematic Review. *Gastroenterology* **2012**, *142*, 46–54.
- (492) Teng, M. W. L.; Bowman, E. P.; McElwee, J. J.; Smyth, M. J.; Casanova, J.-L.; Cooper, A. M.; Cua, D. J. IL-12 and IL-23 Cytokines: From Discovery to Targeted Therapies for Immune-Mediated Inflammatory Diseases. *Nat. Med.* **2015**, *21*, 719–729.
- (493) Farh, K. K.-H.; Marson, A.; Zhu, J.; Kleinewietfeld, M.; Housley, W. J.; Beik, S.; Shores, N.; Whitton, H.; Ryan, R. J. H.; Shishkin, A. A.; Hatan, M.; Carrasco-Alfonso, M. J.; Mayer, D.; Luckey, C. J.; Patsopoulos, N. A.; De Jager, P. L.; Kuchroo, V. K.; Epstein, C. B.; Daly, M. J.; Hafler, D. A.; Bernstein, B. E. Genetic and Epigenetic Fine Mapping of Causal Autoimmune Disease Variants. *Nature* **2015**, *518*, 337–343.
- (494) Huber, S.; Gagliani, N.; Esplugues, E.; O'Connor, W., Jr.; Huber, F. J.; Chaudhry, A.; Kamanaka, M.; Kobayashi, Y.; Booth, C. J.; Rudenski, A. Y.; Roncarolo, M. G.; Battaglia, M.; Flavell, R. A. Th17 Cells Express Interleukin-10 Receptor and Are Controlled by Foxp3(–) and Foxp3+ Regulatory CD4+ T Cells in an Interleukin-10-Dependent Manner. *Immunity* **2011**, *34*, 554–65.
- (495) Chaudhry, A.; Samstein, R. M.; Treuting, P.; Liang, Y.; Pils, M. C.; Heinrich, J. M.; Jack, R. S.; Wunderlich, F. T.; Bruning, J. C.; Muller, W.; Rudenski, A. Y. Interleukin-10 Signaling in Regulatory

T C Is Required for Suppression of Th17 Cell-Mediated Inflammation. *Immunity* **2011**, *34*, 566–578.

(496) Glocker, E. O.; Kotlarz, D.; Boztug, K.; Gertz, E. M.; Schaffer, A. A.; Noyan, F.; Perro, M.; Diestelhorst, J.; Allroth, A.; Murugan, D.; Hatscher, N.; Pfeifer, D.; Sykora, K. W.; Sauer, M.; Kreipe, H.; Lacher, M.; Nustede, R.; Woellner, C.; Baumann, U.; Salzer, U.; et al. Inflammatory Bowel Disease and Mutations Affecting the Interleukin-10 Receptor. *N. Engl. J. Med.* **2009**, *361*, 2033–2045.

(497) Engelhardt, K. R.; Grimbacher, B. IL-10 in Humans: Lessons from the Gut, IL-10/IL-10 Receptor Deficiencies, and IL-10 Polymorphisms. *Curr. Top. Microbiol. Immunol.* **2014**, *380*, 1–18.

(498) Bennett, C. L.; Christie, J.; Ramsdell, F.; Brunkow, M. E.; Ferguson, P. J.; Whitesell, L.; Kelly, T. E.; Saulsbury, F. T.; Chance, P. F.; Ochs, H. D. The Immune Dysregulation, Polyendocrinopathy, Enteropathy, X-Linked Syndrome (IPEX) Is Caused by Mutations of FOXP3. *Nat. Genet.* **2001**, *27*, 20–21.

(499) Wildin, R. S.; Ramsdell, F.; Peake, J.; Faravelli, F.; Casanova, J.-L.; Buist, N.; Levy-Lahad, E.; Mazzella, M.; Goulet, O.; Perroni, L.; Dagna Bricarelli, F.; Byrne, G.; McEuen, M.; Proll, S.; Appleby, M.; Brunkow, M. E. X-Linked Neonatal Diabetes Mellitus, Enteropathy and Endocrinopathy Syndrome Is the Human Equivalent of Mouse Scurfy. *Nat. Genet.* **2001**, *27*, 18–20.

(500) Sun, X.; Gamal, M.; Nold, P.; Said, A.; Chakraborty, I.; Pelaz, B.; Schmied, F.; Pückler, K. v.; Figiel, J.; Zhao, Y.; Brendel, C.; Hassan, M.; Parak, W. J.; Feliu, N. Tracking Stem Cells and Macrophages with Gold and Iron Oxide Nanoparticles – The Choice of the Best Suited Particles. *Appl. Mater. Today* **2019**, *15*, 267–279.

(501) Chen, H.; Wang, G. D.; Chuang, Y.-J.; Zhen, Z.; Chen, X.; Biddinger, P.; Hao, Z.; Liu, F.; Shen, B.; Pan, Z.; Xie, J. Nanoscintillator-Mediated X-Ray Inducible Photodynamic Therapy for *in Vivo* Cancer Treatment. *Nano Lett.* **2015**, *15*, 2249–2256.

(502) Sun, W.; Shi, T.; Luo, L.; Chen, X.; Lv, P.; Lv, Y.; Zhuang, Y.; Zhu, J.; Liu, G.; Chen, X.; Chen, H. Monodisperse and Uniform Mesoporous Silicate Nanosensitizers Achieve Low-Dose X-Ray-Induced Deep-Penetrating Photodynamic Therapy. *Adv. Mater.* **2019**, *31*, 1808024.

(503) Kamkaew, A.; Chen, F.; Zhan, Y.; Majewski, R. L.; Cai, W. Scintillating Nanoparticles as Energy Mediators for Enhanced Photodynamic Therapy. *ACS Nano* **2016**, *10*, 3918–3935.

(504) Kuncic, Z.; Lacombe, S. Nanoparticle Radio-Enhancement: Principles, Progress and Application to Cancer Treatment. *Phys. Med. Biol.* **2018**, *63*, 02TR01.

(505) Liu, Y.; Zhang, P.; Li, F.; Jin, X.; Li, J.; Chen, W.; Li, Q. Metal-Based NanoEnhancers for Future Radiotherapy: Radiosensitizing and Synergistic Effects on Tumor Cells. *Theranostics* **2018**, *8*, 1824–1849.

(506) Rabus, H.; Gargioni, E.; Li, W. B.; Nettelbeck, H.; Villagrasa, C. Determining Dose Enhancement Factors of High-Z Nanoparticles from Simulations where Lateral Secondary Particle Disequilibrium Exists. *Phys. Med. Biol.* **2019**, *64*, 155016.

(507) Rudek, B.; McNamara, A.; Ramos-Mendez, J.; Byrne, H.; Kuncic, Z.; Schuemann, J. Radio-Enhancement by Gold Nanoparticles and Their Impact on Water Radiolysis for X-Ray, Proton and Carbon-Ion Beams. *Phys. Med. Biol.* **2019**, *64*, 175005.

(508) Misawa, M.; Takahashi, J. Generation of Reactive Oxygen Species Induced by Gold Nanoparticles Under X-Ray and UV Irradiations. *Nanomedicine* **2011**, *7*, 604–614.

(509) Sicard-Roselli, C.; Brun, E.; Gilles, M.; Baldacchino, G.; Kelsey, C.; McQuaid, H.; Polin, C.; Wardlow, N.; Currell, F. A New Mechanism for Hydroxyl Radical Production in Irradiated Nanoparticle Solutions. *Small* **2014**, *10*, 3338–3346.

(510) Seo, S. J.; Jeon, J. K.; Han, S. M.; Kim, J. K. Reactive Oxygen Species-Based Measurement of the Dependence of the Coulomb Nanoradiator Effect on Proton Energy and Atomic Z Value. *Int. J. Radiat. Biol.* **2017**, *93*, 1239–1247.

(511) Clark, J. N.; Beitra, L.; Xiong, G.; Fritz, D. M.; Lemke, H. T.; Zhu, D.; Chollet, M.; Williams, G. J.; Messerschmidt, M. M.;

Abbey, B.; Harder, R. J.; Korsunsky, A. M.; Wark, J. S.; Reis, D. A.; Robinson, I. K. Imaging Transient Melting of a Nanocrystal Using an X-Ray Laser. *Proc. Natl. Acad. Sci. U. S. A.* **2015**, *112*, 7444–7448.

(512) Neutze, R.; Wouts, R.; Van der Spoel, D.; Weckert, E.; Hajdu, J. Potential for Biomolecular Imaging with Femtosecond X-Ray Pulses. *Nature* **2000**, *406*, 752–757.

(513) Wernet, P.; Kunnus, K.; Josefsson, I.; Rajkovic, I.; Quevedo, W.; Beye, M.; Schreck, S.; Grübel, S.; Scholz, M.; Nordlund, D.; Zhang, W.; Hartsock, R. W.; Schlotter, W. F.; Turner, J. J.; Kennedy, B.; Hennies, F.; de Groot, F. M. F.; Gaffney, K. J.; Techert, S.; Odelius, M.; Föhlisch, A. Orbital-Specific Mapping of the Ligand Exchange Dynamics of Fe(CO)<sub>5</sub> in Solution. *Nature* **2015**, *520*, 78–81.

(514) Spence, J. XFELs for Structure and Dynamics in Biology. *IUCrJ* **2017**, *4*, 322–339.

(515) Mancuso, A. P.; Yefanov, O. M.; Vartanyants, I. A. Coherent Diffractive Imaging of Biological Samples at Synchrotron and Free Electron Laser Facilities. *J. Biotechnol.* **2010**, *149*, 229–237.

(516) van der Schot, G.; Svenda, M.; Maia, F. R. N. C.; Hantke, M.; DePonte, D. P.; Seibert, M. M.; Aquila, A.; Schulz, J.; Kirian, R.; Liang, M.; Stellato, F.; Iwan, B.; Andreasson, J.; Timneanu, N.; Westphal, D.; Almeida, F. N.; Odić, D.; Hasse, D.; Carlsson, G. H.; Larsson, D. S. D.; et al. Imaging Single Cells in a Beam of Live Cyanobacteria with an X-Ray Laser. *Nat. Commun.* **2015**, *6*, 5704.

(517) Hantke, M. F.; Hasse, D.; Maia, F. R. N. C.; Ekeberg, T.; John, K.; Svenda, M.; Loh, N. D.; Martin, A. V.; Timneanu, N.; Larsson, D. S. D.; van der Schot, G.; Carlsson, G. H.; Ingelman, M.; Andreasson, J.; Westphal, D.; Liang, M.; Stellato, F.; DePonte, D. P.; Hartmann, R.; Kimmel, N.; et al. High-Throughput Imaging of Heterogeneous Cell Organelles with an X-Ray Laser. *Nat. Photonics* **2014**, *8*, 943–949.

(518) Seibert, M. M.; Ekeberg, T.; Maia, F. R. N. C.; Svenda, M.; Andreasson, J.; Jönsson, O.; Odić, D.; Iwan, B.; Rocker, A.; Westphal, D.; Hantke, M.; DePonte, D. P.; Barty, A.; Schulz, J.; Gumprecht, L.; Coppola, N.; Aquila, A.; Liang, M.; White, T. A.; Martin, A.; et al. Single Mimivirus Particles Intercepted and Imaged with an X-Ray Laser. *Nature* **2011**, *470*, 78–81.

(519) Hosseinizadeh, A.; Mashayekhi, G.; Copperman, J.; Schwander, P.; Dashti, A.; Sepehr, R.; Fung, R.; Schmidt, M.; Yoon, C. H.; Hogue, B. G.; Williams, G. J.; Aquila, A.; Ourmazd, A. Conformational Landscape of a Virus by Single-Particle X-Ray Scattering. *Nat. Methods* **2017**, *14*, 877–881.

(520) Poudyal, I.; Schmidt, M.; Schwander, P. Single-Particle Imaging by X-Ray Free-Electron Lasers—How Many Snapshots Are Needed? *Struct. Dyn.* **2020**, *7*, 024102.

(521) Sobolev, E.; Zolotarev, S.; Giewekemeyer, K.; Bielecki, J.; Okamoto, K.; Reddy, H. K. N.; Andreasson, J.; Ayyer, K.; Barak, I.; Bari, S.; Barty, A.; Bean, R.; Bobkov, S.; Chapman, H. N.; Chojnowski, G.; Daurer, B. J.; Dörner, K.; Ekeberg, T.; Flückiger, L.; Galzitskaya, O.; et al. Megahertz Single-Particle Imaging at the European XFEL. *Commun. Phys.* **2020**, *3*, 97.

(522) Malik, V.; Petukhov, A. V.; He, L.; Yin, Y.; Schmidt, M. Colloidal Crystallization and Structural Changes in Suspensions of Silica/Magnetite Core–Shell Nanoparticles. *Langmuir* **2012**, *28*, 14777–14783.

(523) Martin, A. V.; Loh, N. D.; Hampton, C. Y.; Sierra, R. G.; Wang, F.; Aquila, A.; Bajt, S.; Barthelmeß, M.; Bostedt, C.; Bozek, J. D.; Coppola, N.; Epp, S. W.; Erk, B.; Fleckenstein, H.; Foucar, L.; Frank, M.; Graafsma, H.; Gumprecht, L.; Hartmann, A.; Hartmann, R.; et al. Femtosecond Dark-Field Imaging with an X-Ray Free Electron Laser. *Opt. Express* **2012**, *20*, 13501–13512.

(524) Li, X.; Chiu, C.-Y.; Wang, H.-J.; Kassemeyer, S.; Botha, S.; Shoeman, R. L.; Lawrence, R. M.; Kupitz, C.; Kirian, R.; James, D.; Wang, D.; Nelson, G.; Messerschmidt, M.; Boutet, S.; Williams, G. J.; Hartmann, E.; Jafarpour, A.; Foucar, L. M.; Barty, A.; Chapman, H.; et al. Diffraction Data of Core-Shell Nanoparticles from an X-Ray Free Electron Laser. *Sci. Data* **2017**, *4*, 170048.

(525) Jadzinsky, P. D.; Calero, G.; Ackerson, C. J.; Bushnell, D. A.; Kornberg, R. D. Structure of a Thiol Monolayer-Protected Gold Nanoparticle at 1.1 Å Resolution. *Science* **2007**, *318*, 430–433.

(526) Ayer, K.; Xavier, P. L.; Bielecki, J.; Shen, Z.; Daurer, B. J.; Samanta, A. K.; Awel, S.; Bean, R.; Barty, A.; Bergemann, M.; Ekeberg, T.; Estillore, A. D.; Fangohr, H.; Giewekemeyer, K.; Hunter, M. S.; Kirian, R.; Karnevskiy, M.; Kirian, R. A.; Kirkwood, H.; Kim, Y.; et al. 3D Diffractive Imaging of Nanoparticle Ensembles Using an X-Ray Laser. *Optica* **2021**, *8*, 15–23.

(527) Auldridge, M. E.; Forest, K. T. Bacterial Phytochromes: More than Meets the Light. *Crit. Rev. Biochem. Mol. Biol.* **2011**, *46*, 67–88.

(528) Burgie, E. S.; Zhang, J.; Vierstra, R. D. Crystal Structure of Deinococcus Phytochrome in the Photoactivated State Reveals a Cascade of Structural Rearrangements during Photoconversion. *Structure* **2016**, *24*, 448–457.

(529) Sanchez, J. C.; Carrillo, M.; Pandey, S.; Noda, M.; Aldama, L.; Feliz, D.; Claesson, E.; Wahlgren, W. Y.; Tracy, G.; Duong, P.; Nugent, A. C.; Field, A.; Srajer, V.; Kupitz, C.; Iwata, S.; Nango, E.; Tanaka, R.; Tanaka, T.; Fangjia, L.; Tono, K.; et al. High-Resolution Crystal Structures of a Myxobacterial Phytochrome at Cryo and Room Temperatures. *Struct. Dyn.* **2019**, *6*, 054701.

(530) Takala, H.; Björling, A.; Berntsson, O.; Lehtivuori, H.; Niebling, S.; Hoernke, M.; Kosheleva, I.; Henning, R.; Menzel, A.; Ihalainen, J. A.; Westenhoff, S. Signal Amplification and Transduction in Phytochrome Photosensors. *Nature* **2014**, *509*, 245–248.

(531) Giewekemeyer, K.; Aquila, A.; Loh, N.-T. D.; Chushkin, Y.; Shanks, K. S.; Weiss, J. T.; Tate, M. W.; Philipp, H. T.; Stern, S.; Vagovic, P.; Mehrjoo, M.; Teo, C.; Barthelmess, M.; Zontone, F.; Chang, C.; Tiberio, R. C.; Sakdinawat, A.; Williams, G. J.; Gruner, S. M.; Mancuso, A. P. Experimental 3D Coherent Diffractive Imaging from Photon-Sparse Random Projections. *IUCr* **2019**, *6*, 357–365.

(532) Bielecki, J.; Maia, F. R. N. C.; Mancuso, A. P. Perspectives on Single Particle Imaging with X-Rays at the Advent of High Repetition Rate X-Ray Free Electron Laser Sources. *Struct. Dyn.* **2020**, *7*, 040901.